Second harmonic generation in germanotellurite glass ceramics doped with silver oxide

Nhat Truong Lo

THÈSE EN COTUTELLE PRÉSENTÉE

POUR OBTENIR LE GRADE DE

DOCTEUR DE L'UNIVERSITÉ DE BORDEAUX ET DE L'INSTITUTO SUPERIOR TÉNICO

ÉCOLE DOCTORALE SCIENCES CHIMIQUES

SPÉCIALITÉ : PHYSICO-CHIMIE DE LA MATIÈRE CONDENSÉE

Par **Nhat-Truong LO**

TITRE

Second Harmonic Generation in Germanotellurite glass ceramics doped with silver oxide

Sous la direction de Mme Evelyne FARGIN
Et M. Luis Filipe da Silva dos Santos
Et M. Marc DUSSAUZE

Soutenue le 28/10/2015

Membres du jury:

M. SMEKTALA Frédéric – Professeur, Université de Bourgogne	Président/Rapporteur
Mme. DUTREILH-COLAS Maggy – Chargée de recherche, CNRS	Rapporteur
Mme. FARGIN Evelyne – Professeur, Université de Bordeaux	Examinateur
M. Luís Filipe da Silva dos Santos – Professeur, Instituto Superior Técnico	Examinateur
M. Rui Manuel Amaral de Almeida – Professeur, Instituto Superior Técnico	Invité
M. Marc DUSSAUZE – Chargée de recherche, CNRS	Invité

SECOND HARMONIC GENERATION IN GERMANOTELLURITE GLASS CERAMICS DOPED WITH SILVER OXIDE

Contents

GENERAL INTRODUCTION

In the age of photonics, mankind has witnessed a rapid spread of broadband network which changed the methods of communication. One of the most important factors that contribute to this bloom is the transmission capacity. Nowadays, a single bit rate of 10GB/s is deployed, allowing, for instance, fast internet response. However, this wide flourish of applications induces a serious problem of large power consumption. The need for ultrafast systems arises and the idea to use all-optical signal processing devices, which reduces to a minimum the conversions of optical to electric signals, becomes interesting.

The importance of signal processing and transmission promotes new applications for nonlinear optical materials, such as frequency converters with generation of new optical frequencies by nonlinear processes, enabling devices used in electro-photonic systems. Single crystals are well known materials for these applications because of their strong optical nonlinear properties. However, they are costly to manufacture and are strongly dependant on crystal orientation. One way to circumvent this problem is to replace the single crystals with new materials. Inorganic materials like glass are possible candidates because they have many advantages, especially due to their optical properties and ease of fabrication. However, second-order nonlinearity does not exist in glass due to their centrosymmetric structure. Therefore, a composite of two components can present a favourable combination of ferroelectric crystals and glass matrix, combining the nonlinear properties of crystals and the ease of fabrication of glasses. In fact, several glass ceramic materials presenting second harmonic generation arising from $LaBGeO_5$, $LiNbO_3$ and $KNbO_3$ crystals have been reported but their low transparency still limits commercial applications.

One of our laboratories, Institut de Chimie de la Matiere Condensee de Bordeaux, has studied glass ceramics and their optical nonlinear effects for long time. On the other hand, another laboratory in Lisbon, Instituto Superior Tecnico, has solid experiences about tellurite-based glasses which are in focus nowadays due to their specific characteristics. The cooperation between the two laboratories with the financial aid from

International Doctoral School in Functional Materials (IDS FunMat – One of the Erasmus Mundus programs) has provided an opportunity to look for new materials for future electro-photonic devices based on the tellurite-based glass ceramics.

Optical glass ceramics require high transparency and high second-order nonlinearity. To ensure the quality of the transmission in glass ceramics, two common solutions are envisaged: size restriction of ferroelectric crystals and/or reduction of the refractive index difference between the glass and the crystallized parts. The latter requirement can be fulfilled by a careful selection of glass matrix and crystal phase. Although several host-glass compositions have been characterized and tested, tellurite remains one of the most promising glass formers, because of its low melting temperature and the fact that the refractive indices of those glasses and many ferroelectric crystals are quite similar. This means that low scattering losses at the interface between glass and crystals can be obtained and therefore high transparency might be achieved. Another possibility is to control the time and temperature of annealing to obtain small crystals of sub-micron size and thus reduce the scattering of light. However, in order to control the crystal growth in the bulk, it is necessary to avoid dominant surface crystallization and promote bulk crystallization. Only a few reported works show elaboration and optical properties characterizations of transparent tellurite glass–ceramics containing a high crystalline volume fraction. This lack can be attributed to the difficulty of promoting controlled crystallization in TeO_2 -based glasses because of preferential surface crystallization.

Our research concentrates on elaboration and characterization of new glass ceramics, to fulfil the requirements of nonlinear optical materials with high transparency and strong nonlinear activity. Furthermore, a study on the correlation of the ceramics and optical nonlinearity will also be in the scope of this thesis.

Based on the results we have obtained from this study, the manuscript is divided into four distinct parts corresponding to four chapters:

The first chapter of this thesis introduces the literature review about different aspects related to the study. It consists of a brief review of glass and glass ceramics

from elaboration to characterization as well as a theoretical section of nonlinear optics and its role in the studied materials. The end part of this chapter focuses on the progress of tellurite-based glass and glass ceramics, regarding optical nonlinear properties. The up-to-date studies on the properties of germanotellurite glass ($70TeO_2$ – $10GeO_2$ – $10Nb_2O_5$ – $10K_2O$) will also be addressed in this chapter.

In the first part of chapter 2, the characterization techniques and their experimental conditions to analyse the thermal, structural and optical properties of materials will be presented. Details of optical nonlinear measurements to detect the second harmonic signal generated from the materials, in macroscopic and microscopic scales will be also provided. In the second part of the chapter, we will introduce the development of a new methodology based on a mathematical model to correlate multi-scale characterizations. The model will be tested with two glass ceramic systems developed by my colleague Helene Vigouroux. Those are the $LiNbO_3/SiO_2$ and $LaBGeO_5$ systems. The model will take into account the nonlinear properties of the corresponding crystal phases with some appropriate modifications to describe the complex sub-structure of separated spherulites.

The third chapter will focus on the germanotellurite glass system with addition of silver oxide. It will start with the preparation and characterization of new glass and glass ceramic compositions. Tellurite-based glasses usually present surface crystallization; therefore, silver oxide was introduced as nucleating agent is order to promote bulk crystallization. The effect of silver ions on the thermal, optical and structural properties of the glass will be studied by using differential scanning calorimetry, X-ray diffraction, electron microscopy, UV-Visible and Raman spectroscopies. Finally, the results of glass ceramics relating to the optical linear and nonlinear properties will be presented. The evolution of the nonlinear intensity as a function of separated domains' size will be discussed.

The fourth chapter focusses on the origin of the observed optical nonlinearity, i.e. second harmonic generation activity, with respect to the organization of crystallites within the separated domains. The study is based on a unique correlative Raman/Second Harmonic Generation technique which is helpful to give an insight on

the structural changes and correlative optical nonlinear function of a sub-microscopic area. This chapter also reports the presence of a crystalline of sub-structure in the separated domains and the application of the mathematical model presented in chapter 3, to correlate it to the global second harmonic generation responses.

Based on this work, I presented an oral presentation in an international conference and did/will publish three articles.

1. *Volume precipitation in germanotellurite glass ceramics and its second harmonic generation properties*, ESG2014: 12th European Society of Glass Conference held in Parma, Sep 21-24, (2014).

2. *Isotropic octupolar SHG response in La_2O_3 - B_2O_3 - GeO_2 glass-ceramic with spherulitic precipitation of $LaBGeO_5$, Applied Physics Letters*, 106, 161901 (2015)

3. *Second Harmonic Generation in transparent Germanotellurite bulk glass ceramics* (to be submitted)

4. *Correlation between structural modification and Second Harmonic Generation in bulk precipitated Germanotellurite glass ceramics* (to be submitted)

CHAPTER 1 – LITERATURE REVIEW

Contents

CHAPTER 1 – BIBLIOGRAPHY

1.1 Introduction

Glasses are amorphous materials that exhibit a glass transition which is a reversible transition from a hard and relatively brittle state into a molten or rubber-like state [1, 2]. Mankind has found the way to make glasses for a long time, and till now, it is still a useful material for human life. Nevertheless, since last century, it is a choice for many advanced applications in vision devices and telecommunication.

Scientists have firstly used the phrase “Glass ceramics” since 1960s to describe a new material [3]. Glass ceramics materials (sometimes known as vitro-cerams, pyrocerams, vitroceramics, vitroceramiques and sittals) [4] are polycrystalline solids embedded in a residual glass matrix. They are normally produced by devitrification of glasses. The first step of elaboration involves conventional techniques for glass production, followed by controlled crystallization; this process leads to separation of crystalline phase from the glassy parent phase in the form of tiny crystals, where the number of crystals, their growth rate and their final size are controlled by suitable heat treatment [5-8].

The fact that glass ceramics can combine the properties of both two components of glasses and ceramics leads to the boom of researches and applications.

Glasses are well known because of low cost and ease of production. Besides, they are homogeneous and transparent materials with no porosity. Crystals, on the other hand, contain many interesting properties in the field of optics, mechanics and electronics [4, 8, 9]. When combining both of them, a trade-off could be paid forming new materials with associated properties of interest for engineers and researchers. Many interesting papers and patents related to glass ceramics have been published and granted from research institutes, universities and companies [4, 10].

Nowadays, glass ceramics becomes a promising candidate for many applications in many different fields from technics to consumer [4, 11-13]. Trace back to the middle of 20^{th} century, the first commercially viable glass ceramics was applied in aerospace industry to fabricate radomes which protect radar equipment in the noses of aircraft and rockets. Glass ceramics was used because it showed many advantages such as low dielectric constant, low coefficient of thermal expansion, low dielectric loss, high strength, and high abrasion resistance [4, 8, 14].

Another application which can be listed here is the Magnetic Memory Disk Substrates [15, 16]. Four types of glass ceramics often used for these substrates to improve the mechanical property are spinel-enstatite, spinel, lithium disilicate and canasite. Enstatite, for instance, is an important accessory phase to increase the fracture toughness above $1MPa.m^{0.5}$. They prove a favourable high Young's modulus of 100-165 GPa to prevent the flutter of the magnetic disk at high rotational speeds up to 10000 rpm [8].

For the last three decades, we have observed a continuous and significant development of computer industry. Each new computer launched was soon replaced by a faster and more powerful one in just few months. Human demands require un-exhaustedly a new system in which all limits of usage could be challenged. The efforts to fabricate faster systems led to the photonic age which adapts the demands of manufacturers to replace electronic components by all optical-processing devices such as optical switching, amplification, sensors, transducers, actuators, etc [17]. Second order optical responses such as Second

Harmonic Generation (SHG), first observed in 1961 by Franken et al., is a key property for these applications [18].

Single crystals with SHG properties are commonly used but their cost and difficulties in fabrication limited their commercial applications. In 1991, Komatsu et al. applied for the first time glass ceramics in which crystals were grown inside a host glass for nonlinear optics [19]. Furthermore, development of micro photonic devices nowadays also requires responses of nonlinear optical signals at the micro-scale. Hence, interest in materials with SHG properties again raised and further applications have been considered. [20]

1.1.1 Fundamentals of inorganic glasses

All kinds of glasses, including metallic glasses and organic glasses, have two common characteristics. The first one is the absence long-range structural order. This means that glasses are amorphous solid with short-range order, but no regularity in the arrangement of its molecular constituents. Secondly, glasses exhibit time-dependent glass transformation behaviour [1, 2]. The traditional method to produce non-crystalline materials is the melt-quenching process. This method is based on the fact that a slow cooling allows enough time for a viscous liquid to alter its local atomic arrangement to attain the minimum free energy at the corresponding temperature, whereas a rapid cooling causes an increase of viscosity that is too quick for the local atomic arrangement to follow [21]. The structure of a rapidly cooled glass is more open than that of a slowly cooled one because the freezing of the atomic arrangement occurs at a higher temperature. Nowadays there are other methods to produce glass such as sol-gel process and chemical vapour deposition [1], however, those processes are out of the scope of this thesis.

Thermodynamic aspect of glass formation

Based on the enthalpy-temperature diagram, presented in **Figure 1.1**, we can see the path going from melting liquid to glass. In literature, a volume-temperature diagram is sometimes used but because volume and enthalpy behave in a similar

way, we can completely use same explanation to study the mechanisms when cooling the melt depending on the time [1]. Above the melting point and if the temperature of the melt is decreased slowly, the atomic structure of the melt will be characteristic of the exact temperature at which the melt is held. Below the melting temperature, the conversion of the material to the crystalline state with long range, periodic atomic arrangement would happen if it is slow enough to reach the thermodynamic stable state which is crystal. We should notice that crystallization occurs if there are enough numbers of nuclei and sufficiently large crystal growth rate. In this case, the enthalpy will decrease abruptly at T_m (as shown on the diagram). After fully converting to crystal, continuous cooling will result in a further decrease in enthalpy due to the heat capacity of the crystal.

If the temperature of the liquid is quickly decreased below the melting point, we can obtain a super-cooled state without any crystallization. The structure of the liquid continues to rearrange. This rearrangement is partially due to the decrease in the amplitude of atomic vibrations and partially the change in structure of the melting liquid which becomes more compact as the temperature falls. However, there is no abrupt decrease in enthalpy due to discontinuous structural rearrangement. As the liquid is cooled further, the viscosity increases due to the lower and lower mobility of molecules. This increase in viscosity becomes so great that the atoms can no longer completely rearrange to the equilibrium liquid structure. The straight line starts to change and follow a curve of gradually decreasing slope, until it eventually becomes determined by the heat capacity of the frozen liquid, i.e., the viscosity is so high that the structure of the liquid becomes fixed and is no longer temperature-dependent. The region between the limits where the enthalpy corresponds to the equilibrium liquid and to that of the frozen solid, is designated the glass transformation region. The liquid now becomes a glass.

For a supercooled liquid, depending on the cooling rate, the relation between enthalpy and temperature can be modified correspondingly. Because the viscosity is controlled by the temperature of the liquid, a slower cooling rate will allow the

enthalpy to follow the supercooled curve to a lower temperature. The glass transformation temperature (T_g) is defined as the intersection of the extrapolated glass line and the super-cooled liquid line. The glass transformation temperature will, as a sequence, shift to lower temperature (lower curve in diagram) for slow cooled glasses. The glass obtained will have a lower enthalpy than the one obtained with a faster cooling rate (see Figure 1.1). The atomic arrangement will also retain the characteristics of a supercooled liquid just before the glass transformation temperature.

However, it is useful to adopt the onset of the glass transformation region during reverse heating of a glass. As the glass transition temperature (T_g) for which the solid begins to behave as a viscoelastic solid on heating, this temperature depends on the thermal history of the glass elaboration [1, 21].

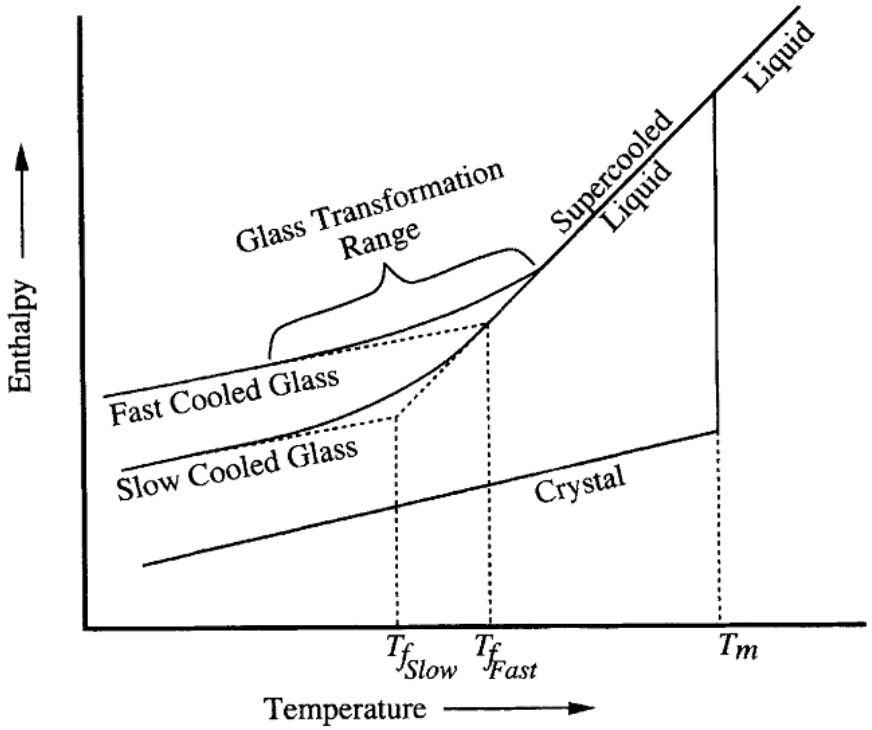

Figure 1.1: Enthalpy-temperature diagram for a glass-forming melt [1]

Local structure in glasses [1]

Unlike the crystalline materials with long range, periodic structure, glasses, or amorphous unstable materials, have different structure description. The most

popular model for glass structure description is based on the idea of Zachariasen and called random network theory [1]. Zachariasen's rules for glass formation in oxides, which are summarized below, state the conditions for the formation of continuous 3-dimensional amorphous network.

Zachariasen's rules for glass formation in simple oxides

a. Each oxygen atom is linked to no more than two cations
b. The oxygen coordination number of the network cation is small
c. Oxygen polyhedra share only corners and not the edges or faces
d. At least 3 corners of each oxygen polyhedron must be shared in order to form a 3-dimensional network.

Modified rules for complex glasses

e. The sample must contain a high percentage of network cations which are surrounded by oxygen tetrahedral or triangles
f. The tetrahedra or triangles share only corners with each other.
g. Some oxygens are linked only to two network cations and do not form further bonds with any other cations.

From the above list of rules, the first basic element for the network formation is the coordination of the cations as the building blocks which constitute the network. The building blocks exhibit order at the level of several associated atoms or ions. Because of this small range order, it is sometimes called short range order. Silicate glasses, for instance, usually contain tetrahedral coordination of Si whereas boron can potentially exist in either 3- or 4-fold coordination in borate glasses.

Secondly, the understanding of glass structure often includes the number and arrangement of bridging and non-bridging bonds (NBO) consuming the network conectivity. These bonds connect each of the building block to their neighbours by sharing oxygen corner to form the network. NBO density appears as an indication

of the network breakages and should be taken into account to evaluate the connectivity degree in the glass network.

1.1.2 Phase separation in glasses

There are two types of phase separation: stable and metastable immiscibility. The distinction between them is based on temperature. If the phase separation occurs at temperatures higher than the liquidus one, it is stable immiscibility phase separation. Metastable immiscibility occurs at lower temperatures than the liquidus one [7]. In this study, we concentrate on the metastable immiscibility.

Figure 1.2 illustrates the existence of phase separation within a binary system (C)X – (1-C)Y.

- If $C < C_1$ or $C > C_4$, phase separation is impossible to occur because the melt is stable. This region is called miscibility and the boundary separated with the inside regions is nominated immiscibility boundary.
- $C_1 < C < C_2$ and $C_3 < C < C_4$: the formation of second phase occurs due to the change in energy. In this region, a droplet-type microstructure dispersed throughout the matrix can be found.
- $C_2 < C < C_3$: the formation of inhomogeneity occurs and the microstructure tends to be continuously interconnected. The boundary as indicated on Figure 1.2 is nominated spinodal boundry.

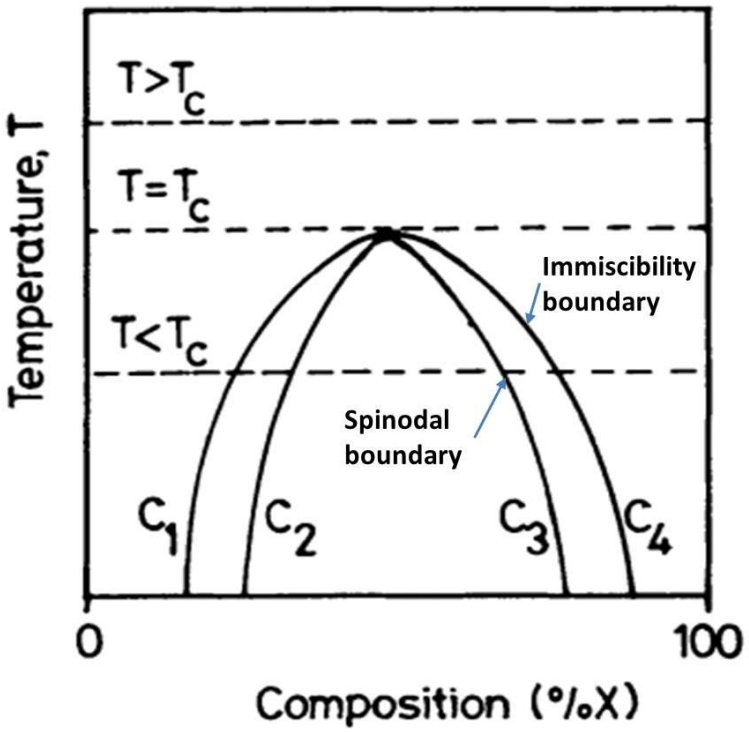

Figure 1.2: Phase separation regions in a binary (C)X – (1-C)Y glass system [7]. T_c is critical temperature for phase separation.

The two types of phase separation (droplets in matrix morphology and interconnected morphology) can be illustrated in **Figure 1.3** for sodium silicate system [22].

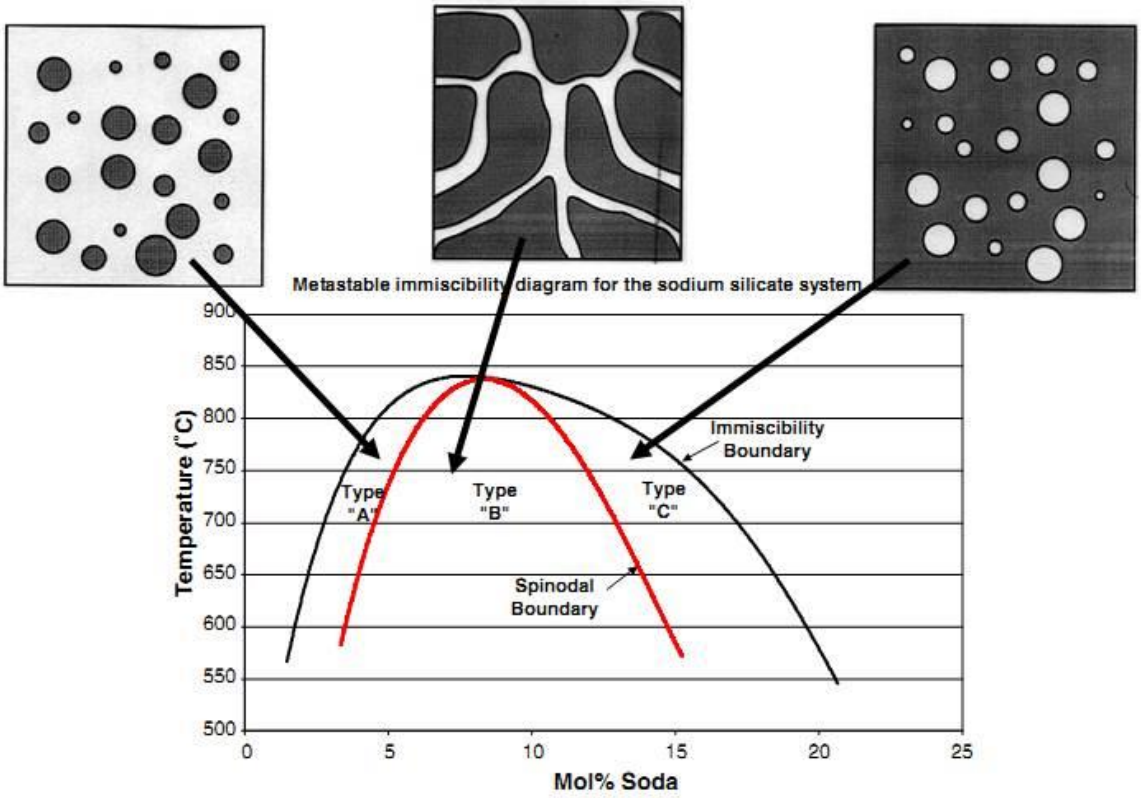

Figure 1.3: An example of two main shapes of phase separation in sodium silicate system [22].

1.1.3 Glass ceramics

Glass ceramics can be formed through heat treatment and proper control of the crystallization process. The development of crystals in a mother glass generally occurs in two stages, formation of nuclei (nucleation) and crystal growth. These two stages require a two-step heat treatment [9, 23, 24]. Marotta et al. developed a technique based on DSC method to define the temperature at which the maximum nucleation rate takes place [25, 26]. Then, Ray et al. showed that the DSC method can be applied to determine the temperature of maximum crystal growth as well [27]. In this section, we show the background of nucleation and crystal growth, including the effect of adding nucleating agents.

Nucleation

Theoretically, there is a model for nucleation process based on the thermodynamic (W^*) and kinetics (ΔG_D) free energy barriers to nucleation [2, 7]. The nucleation rate (I) is described by the following expression:

$$I = Aexp[-(W^* + \Delta G_D)/kT] \quad (1.1)$$

where k is Boltzmann constant and A is the exponential factor, which can be expressed as

$$A = 2n_V V^{\frac{1}{3}}(\frac{kT}{h})(\frac{\sigma}{kT})^{1/2} \quad (1.2)$$

Where n_V is the number of atoms of the crystallizing component phase per unit volume of the liquid V, σ is the crystal-liquid interfacial free energy per unit area and h is Planck's constant.

However, practically, the process of nucleation is assumed to be influenced by two factors [8]:

- Chemical composition of the base glass, with the possible addition of a nucleating agent.
- Controlled heat treatment of the base glass as a function of time and temperature.

Volmer (1939) defined nucleus as an entity that belongs to a new phase but its formation is unstable in the supersaturated mother phase. Further description for its formation is based on thermodynamics and kinetics. The thermodynamic driving force of the transition between glass and crystal is the variation of Gibbs free energy between the melt and the crystal. The reaction rate of nucleation must be inspected in regarding to the kinetics of nucleation [8, 29].

Nucleation can be separated into homogeneous and heterogeneous nucleation [8, 28]. In case of homogeneous nucleation which occurs randomly throughout the system, a new phase develops without any foreign boundaries [2]. In heterogeneous nucleation, foreign boundaries such as substrates and grain boundaries are involved. This type of nucleation is the typical mechanism in the

development of glass - ceramics, as boundaries cannot be excluded. Surface crystallization is one of its consequences.

For all types of glass ceramics, the nucleation process occurs much easier on the surface leading to heterogeneous nucleation in the early stage of heat treatment [30]. As a result, heterogeneous crystallization from the surface is preferable than homogeneously from interior volume. There are two major factors that may favour surface crystallization [30].

(i) The crystal phase has higher density than the mother glass. Furthermore, the viscosity of the glass is too high to relax the stresses. Therefore, devitrification is influenced by tensile stresses in the crystallites and compressive stresses in the surrounding matrix. At the surface, those stresses will be partly reduced, so it is more favourable for surface crystallization to occur.

(ii) In some cases, the difference in interfacial energies may favour surface crystallization because the crystals forming at the surface will have the crystal ambient interface instead of glass-ambient interface in comparing to the formation of new glass-crystal interface in the interior.

Influences of nucleating agents

Surface nucleation, however, is not interesting in many cases, especially due to the difficulty for shaping. Then there are two available options to exploit heterogeneous nucleation for making homogeneous bulk precipitated glass ceramics [30].

(a) Selection of the glass composition can promote the nanoscale phase separation before the crystallization process begins. This separation would usually occur uniformly throughout the volume. When the phase separated structure provides sites for easier nucleation, the sample crystallizes homogenously.

(b) Another possibility is addition of a nucleating agent which is soluble in the melt of starting composition but create defects out during nucleation heat treatment.

To illustrate the second possibility, the heterogeneous nucleation of the oxide phase has been induced by adding metallic nucleants such as Au, Ag, Cu, Pt and Pd or adding some oxide nucleating agents such as TiO_2, ZrO_2, P_2O_5, or Cr_2O_3 [31]. During the devitrification, the metallic nucleating agents are precipitated at relatively low temperature as a result of a strong decrease in solubility and simultaneous reduction to the metallic form [31]. In case of oxide nucleating agents, the metastable separation will occur homogeneously inside the volume which leads to bulk crystallization. Therefore, the role of nucleating agents in initiating glass crystallization from randomly distributed centres was the major factor allowing the introduction of glass ceramics into industrial applications [32].

Crystal growth

When the nucleus approaches the critical size, the crystal growth will begin. Actually, as shown on **Figure 1.4**, both processes overlap together from glass transition temperature T_g. At higher temperature, especially in the Ostwald-Miers range, crystals will increase in size without creating more nucleuses.

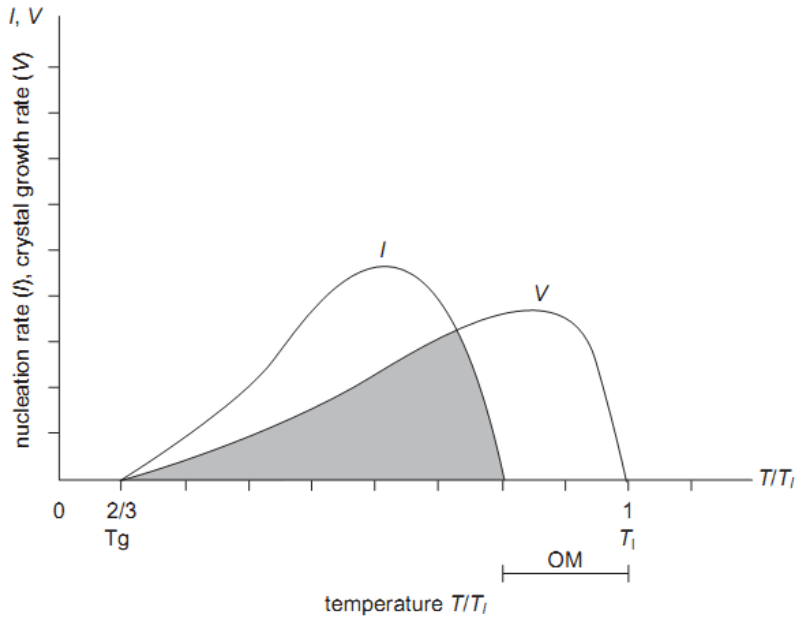

Figure 1.4: Nucleation rate (I) and crystal growth rate (V) in respect to ratio of temperature T/T_l, where Tl is the liquid temperature. OM represents Ostwald-Miers range of metastable supercooling where only crystal growth process occurs [8]

I and V are respectively the nucleation rate and crystal growth rate. The diagram illustrates both of the parameters as a function of reduced temperature (T/T_l) in which T_l represents liquidus temperature. The grey region is the overlap temperature range in which both of the nucleation and crystal growth take place. OM represents for Ostward-Miers range of metastable supercooling. In this range, only crystal growth process occurs.

1.2 Nonlinear optics in brief

1.2.1 Interaction of light with dielectrics and nonlinear optical phenomenon

The propagation of light in space or matter can be described by a time and space varying electric and magnetic fields. All materials interact with the electric field of the light through a collection of electric dipoles constituting the material. The positive poles will tend to move in the direction of the electric field (E) as negative poles constituted by electrons will tend to move on the opposite one. We should notice that the electrons with much lighter mass move more significantly ($m_{electron} \approx \frac{1}{1000} m_{proton}$), along the electric field. In dielectric media, this oscillation

of the dipolar separation leads to oscillating dipole moments with the same frequency as the applied optical field. In general, the bulk optical oscillating response called induced polarization P results from summation of responses from all individual dipole moments [33].

It is well-known that the electromagnetic radiation is described by Maxwell's equations [34]:

$$\nabla.\vec{D} = \rho \tag{1.3}$$

$$\nabla \times \vec{H} = \frac{\partial \vec{D}}{\partial t} + \vec{J} \tag{1.4}$$

$$\nabla \times \vec{E} = -\frac{\partial \vec{B}}{\partial t} \tag{1.5}$$

$$\nabla.\vec{B} = 0 \tag{1.6}$$

Where $\vec{D}$ Electric displacement (C/m^2)

$\vec{E}$ Electric field (V/m)

$\vec{B}$ Magnetic field (T or V.s/m^2)

$\vec{H}$ Magnetic field intensity (A/m)

ρ Volume charge intensity (C/m^3)

$\vec{J}$ Current density (A/m^2)

In non-magnetic material, $\vec{B} = \mu_o \vec{H}$ and if $\rho = 0, j = 0$

$$\Delta\vec{E} = -\frac{1}{c^2}\frac{\partial^2 \vec{E}}{dt^2} - \mu_o \frac{\partial^2 \vec{\rho}}{dt^2} \tag{1.7}$$

The electric displacement field $\vec{D}$ is given by

$$\vec{D} = \varepsilon_o \vec{E} + \vec{P} \tag{1.8}$$

Where $\vec{E}$ is the electric field and $\vec{P}$ is the polarization field generated from electric field and dipoles interactions within the medium, ε_o is free space permittivity. In general, the polarization is expanded in a Taylor series and the function of the electric field E(ω) is given by

$$\vec{P} = \vec{P}^{(1)} + \vec{P}^{(2)} + \vec{P}^{(3)} + \cdots = \varepsilon_o(\chi^{(1)}\vec{E} + \chi^{(2)}\vec{E}\vec{E} + \chi^{(3)}\vec{E}\vec{E}\vec{E} + \cdots) \quad (1.9)$$

Where $P^{(1)}$ is linear, $P^{(2)}$ is quadratic, and $P^{(3)}$ is cubic as a function of the electric field, and so on.

Normally, intensity of light is sufficiently low and this relation is limited to the first order rank, or linearity. The induced polarization of the whole medium is given by the following linear expression

$$\vec{P}(\omega) = \vec{P}^{(1)} = \varepsilon_o\chi^{(1)}(\omega)\vec{E}(\omega) \quad (1.10)$$

Where $\chi^{(1)}(\omega)$ is the first-order susceptibility (or linear susceptibility). The equation (1.10) can be expressed as tensors of rank 2 with nine components $\chi_{ij}^{(1)}$, so the polarization becomes:

$$P_x(\omega) = \varepsilon_o[\chi_{xx}^{(1)}(\omega)E_x(\omega) + \chi_{xy}^{(1)}(\omega)E_y(\omega) + \chi_{xz}^{(1)}(\omega)E_z(\omega)$$

$$P_y(\omega) = \varepsilon_o[\chi_{yx}^{(1)}(\omega)E_x(\omega) + \chi_{yy}^{(1)}(\omega)E_y(\omega) + \chi_{yz}^{(1)}(\omega)E_z(\omega) \quad (1.11)$$

$$P_z(\omega) = \varepsilon_o[\chi_{zx}^{(1)}(\omega)E_x(\omega) + \chi_{zy}^{(1)}(\omega)E_y(\omega) + \chi_{zz}^{(1)}(\omega)E_z(\omega)$$

Or

$$\begin{pmatrix} P_x \\ P_y \\ P_z \end{pmatrix} = \varepsilon_o \begin{pmatrix} \chi_{xx}^{(1)} & \chi_{xy}^{(1)} & \chi_{xz}^{(1)} \\ \chi_{yx}^{(1)} & \chi_{yy}^{(1)} & \chi_{yz}^{(1)} \\ \chi_{zx}^{(1)} & \chi_{zy}^{(1)} & \chi_{zz}^{(1)} \end{pmatrix} \begin{pmatrix} E_x \\ E_y \\ E_z \end{pmatrix} \quad (1.12)$$

In short, the linear polarization can be described as follow:

$$P_i = \varepsilon_o \sum_j \chi_{ij}^{(1)} E_j \ ; j = x, y, z \quad (1.13)$$

However, since the laser was invented and its applications become popular, the interaction of materials with highly intense illumination has established an issue for engineering the nonlinear optical effects. The second and third-order ranks in Equation (1.9) have dramatically arisen. $\chi^{(2)}$ and $\chi^{(3)}$ are the second and third-order susceptibilities which characterize the nonlinear optical response of the medium [34-36].

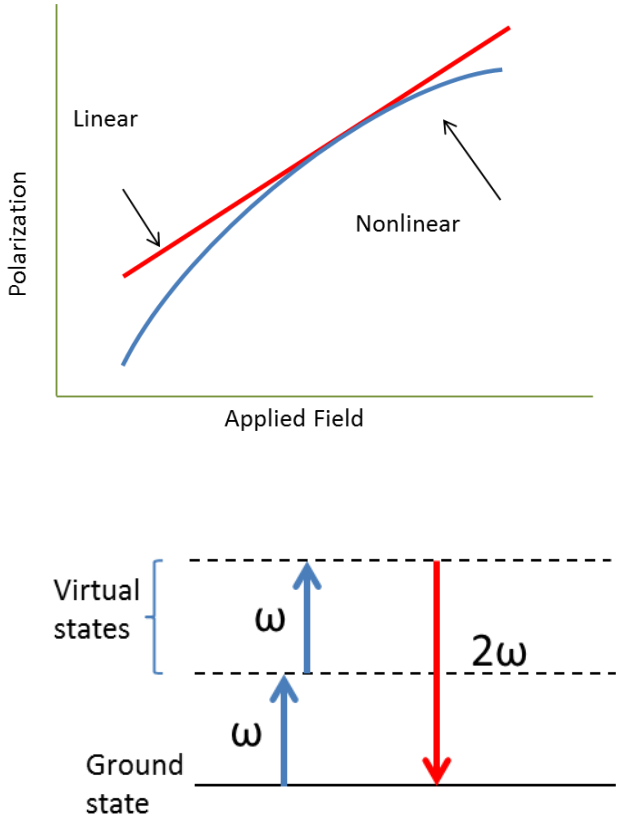

Figure 1.5: Linear and nonlinear responses of P against E (above) and mechanism of SHG (below)

Considering the general case in n^{th} order, nonlinear polarization can be generated at new frequencies

$$\vec{P}^{(n)}(-\omega_\sigma;\omega_1,\omega_2,\dots,\omega_n) = \varepsilon_o\chi^{(n)}\vec{E}(\omega_1)\vec{E}(\omega_2)\vec{E}(\omega_3)\dots\vec{E}(\omega_n) \qquad (1.14)$$

Where $\chi^{(n)}$ is a susceptibility tensor of order n+1 and $\omega_\sigma = \pm\omega_1 \pm \omega_2 \pm \omega_3 \pm \cdots \pm \omega_n$ is the resulting of frequency from nonlinear response of the material. Therefore, the second and third-order susceptibility can be formed like

$$\vec{P}^{(2)}(-\omega_\sigma; \omega_1, \omega_2) = \varepsilon_o \chi^{(2)} \vec{E}(\omega_1)\vec{E}(\omega_2) \tag{1.15}$$

$$\omega_\sigma = \pm\omega_1 \pm \omega_2$$

$$\vec{P}^{(3)}(-\omega_\sigma; \omega_1, \omega_2, \omega_3) = \varepsilon_o \chi^{(3)} \vec{E}(\omega_1)\vec{E}(\omega_2)\vec{E}(\omega_3) \tag{1.16}$$

$$\omega_\sigma = \pm\omega_1 \pm \omega_2 \pm \omega_3$$

$\chi^{(2)}$ and $\chi^{(3)}$ nonlinear optical susceptibilities are tensors of the third and the fourth rank containing 27 and 81 components, respectively. Both of them are responsible for many optical phenomena as mentioned in Table 1.1

In the scope of this thesis, we will focus on the second-order polarization. If $\omega_1 = \omega_2 = \omega$, $P^{(2)}$ results from the combination of two photons with same frequency to make a new one with double energy and half of wavelength (Figure 1.5). This nonlinear process is called Second Harmonic Generation. Regarding to the Cartesian coordinates, the Equation (1.15) becomes

$$P_i^{(2)}(2\omega) = \varepsilon_o \sum_{j,k} \chi_{ijk}^{(2)} E_j(\omega) E_k(\omega) \tag{1.17}$$

Where i, j, and k can be related to the axis orientation x, y, z.

Due to space orientation considerations, $\chi^{(2)}$ coefficients do not change through space referential permutatons, then

$$\chi_{ijk}^{(2)} = \chi_{kij}^{(2)} = \chi_{jki}^{(2)}, \forall i, j, k \tag{1.18}$$

The more general symmetry requirement that is currently used in Equation 1.18, called the overall permutation symmetry, is an approximation which applies when all the optical fields involved in the susceptibility formulae (excitations and response) have frequencies far from resonant frequencies. It has been first formulated by Kleinman [37].

In SHG, the tensor d_{il} is used instead of $\chi^{(2)}_{ijk}$ ($d_{il} = \frac{1}{2}\chi^{(2)}_{ijk}$), if Kleinman symmetry holds, i.e. all the field frequencies are in the transparent spectral region, fa from resonances of the nonlinear medium), in which i=1, 2, 3 correspond to x,y,z axis and l is as below:

jk	xx	Yy	zz	yz=zy	xz=zx	xy=yx
l	1	2	3	4	5	6

$$\begin{bmatrix} P_x^{(2)}(2\omega) \\ P_y^{(2)}(2\omega) \\ P_z^{(2)}(2\omega) \end{bmatrix} = \varepsilon_o \begin{bmatrix} d_{11} & d_{12} & d_{13} & d_{14} & d_{15} & d_{16} \\ d_{21} & d_{22} & d_{23} & d_{24} & d_{25} & d_{26} \\ d_{31} & d_{32} & d_{33} & d_{34} & d_{35} & d_{36} \end{bmatrix} \begin{bmatrix} E_x^2(\omega) \\ E_y^2(\omega) \\ E_z^2(\omega) \\ 2E_y(\omega)E_z(\omega) \\ 2E_x(\omega)E_z(\omega) \\ 2E_x(\omega)E_y(\omega) \end{bmatrix} \quad (1.19)$$

Table 1.1: Basic electro-optical and nonlinear-optical effects observed in dielectrics [33, 36]

Order	Tensor	Effect	Description of the effect
2	$\chi^{(2)}(-\omega, \omega, 0)$	Linear electro optical effect (Pokel's effect)	Under the action of an electric field, there is a change of refractive index of the NLO medium. It is observed only in non-centrosymmetrical crystals
2	$\chi^{(2)}(0, \omega, -\omega)$	Optical detecting	The electric field appears in the NLO medium at illumination
2	$\chi^{(2)}(-2\omega, \omega, \omega)$	Generation of the second Harmonic of laser emission	The emission of light with a double frequency happens at illumination of the NLO medium

2	$\chi^{(2)}(-\omega_3, \pm\omega_2, \omega_1)$	Generation of light with total frequency equal to the sum or the difference of frequencies of incident emissions	It is observed at illumination of the NLO medium by two light sources with different frequency (wave length). The emission with the frequency equal to a sum or difference of frequencies of submitting emissions is observed
3	$\chi^{(3)}(-\omega, \omega, 0,0)$	Quadratic electro optical effect (Kerr's effect)	Because of the action of an electric field there is a change of the medium's refractive index.
3	$\chi^{(3)}(-\omega_2, \omega_1, -\omega_1, \omega_2)$	Nonlinear refractive index	The medium's refractive index changes in dependence on emission's intensity according to the formula: $n=n_o+n_2I$, where $n_2=6\chi^{(3)}/4\varepsilon_o n_o^2 c$. The self-focusing and self-defocusing of the laser beam are the special cases.
3	$\chi^{(3)}(-3\omega, \omega, \omega, \omega)$	Generation of the third harmonic	There is an emission of light with the threefold frequency at illumination of the medium

3	$\chi^{(3)}(-\omega_4, \omega_1, \omega_2, \omega_3)$	Multiwave mixing	At illumination of the medium by three light sources with different frequencies there is a generation of light with the frequency equal to the sum of the frequencies of incident emissions

Symmetry plays an important role to define the optical behaviour of material and, therefore, its susceptibilities. It includes permutation symmetry, time-reversal symmetry and symmetry in space which are of fundamental importance in nonlinear optics. While the first two symmetries themselves are fundamental properties of the susceptibilities and have been taken into account before leading to independent coefficients, space symmetry, on the other hand, reflects the structural properties of the nonlinear medium [34]. A full list of Point Group symmetries and their un-vanishing tensors can be found in [34].

All tensors components $\chi^{(2)}_{ijk}$ of centrosymmetric materials are zero [33-36]. As a result, second-order nonlinear optics effects ($\chi^{(2)}(-2\omega;\omega,\omega)$) as well as first-order electro-optical effects ($\chi^{(2)}(-\omega;\omega,0)$) are not observed either in centrosymmetric crystals or in glasses.

1.2.2 Transmitted SHG responses in nonlinear active material

The intensity of the emitted SHG signal $I_{2\omega}$ in transmission mode depends on several factors related to the intrinsic properties of the experimental sample and the path length through the sample. The intensity $I_{2\omega}$ can be estimated as following [34, 38]

$$I_{2\omega}(L) = \frac{(2\omega)^2}{8\varepsilon_o c^3} \frac{\left|\chi^{(2)}\right|^2}{n_\omega^2 . n_{2\omega}} I_\omega^2 . L^2 . sinc^2\left(\frac{\Delta k . L}{2}\right) \quad (1.20)$$

Where L is the SHG active distance in the measured sample; n_ω and $n_{2\omega}$ are refractive index of the material at frequency ω and 2ω, respectively; $\chi^{(2)}$ is second-order efficient susceptibility taking into account the polarizations of the incident and SHG transmitted beams; symmetry of the studied sample and then relative orientations between polarizations and symmetry axis of the studied material; sinc is the mathematical function f(x)=sinx/x; c is the speed of light; and Δk, expressed as $\Delta k = 2k - k_2 = 2\omega(n_{2\omega} - n_\omega)/c$, is called the wave-vector mismatch [34].

The incident laser beam with frequency ω transmitted through the SHG-active material and the generated wave at frequency 2ω interfere as they propagate together in the medium. The intensity of the SHG then depends on the refractive indices n_ω and $n_{2\omega}$. It is maximum for phase matching condition. In practice, the phase matching occurs only in the case of suitably oriented crystals leading to $n_\omega = n_{2\omega}$. In the case of oxide glasses and transmission in the UV-Vis-NIR window, in general: $n_\omega < n_{2\omega}$. Therefore, a glass containing crystals randomly oriented will always be a system with no possibility of phase matching. Then, in these materials, the waves do not propagate at the same speed ($n_\omega \neq n_{2\omega} \rightarrow \Delta k \neq 0$), and interferences induce variation of the SHG amplitude. If we define the coherence length (L_c) as the distance necessary to induce a phase shift π between the two waves: $L_c = \pi/|\Delta k|$, therefore, the intensity follows the sinc function of the ratio L/L_c given on **Figure 1.6** [34, 38].

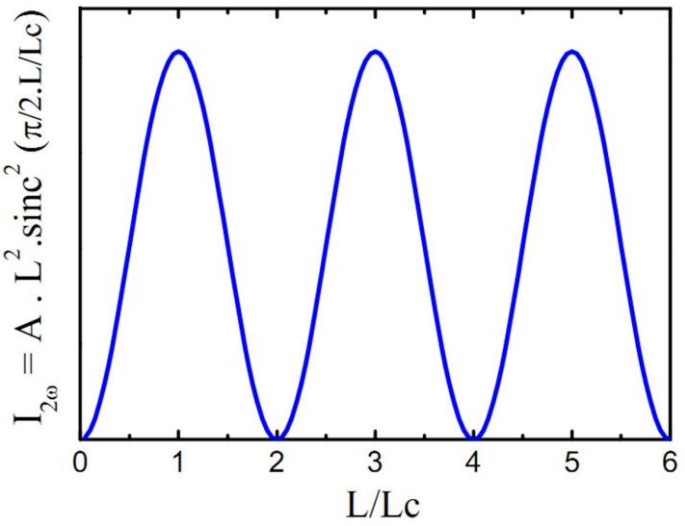

Figure 1.6: Typical curve shape of the f(L/Lc) function

Therefore, the generated intensity ($I_{2\omega}$) has maxima for a length: $L=(2n + 1)L_c$ with an integer n and it becomes zero for $L=2nL_c$.

1.3 Nonlinear optical crystals

1.3.1 Nonlinear optical crystals in glass ceramics

A Dmitriev and co-workers listed 77 popular ferroelectrics materials which are classified into 4 categories consisting of basic, frequently used, other inorganic and organic [39]. Besides that, some other studies reported several phases such as $LiMX_2$ (M = Al, In, Ga, and X = S, Se, Te) as new nonlinear crystals [40].

The list of popular ferroelectric materials consists of alkaline-earth titanate of perovskite family like $BaTiO_3$ [41, 42], an alkali niobate like $LiNbO_3$ or $KNbO_3$, a mixed alkaline-earth niobate of the tungsten bronze family like $Sr_{0.5}Ba_{0.5}Nb_2O_6$ (SBN), an alkali tantalate like $LiTaO_3$, or more complex crystalline phase like $LaBGeO_5$. Table 1.2 gives a non-exhaustive list of successful elaboration of optical glass ceramics with ferroelectric phase. Among the glass ceramic systems listed, the ferroelectric behaviour has not been demonstrated explicitly for some of them but was inferred from indirect observations of structure or optical properties [43, 44].

Table 1.2: Materials systems from which transparent ferroelectric glass ceramics have been obtained [30, 39]

	Glass system	Ferroelectric phase
1	Li_2O-Nb_2O_5-SiO_2 [45]	$LiNbO_3$
	$LiNbO_3$-SiO_2 [46]	$LiNbO_3$
	K_2O-Li_2O-Nb_2O_5-SiO_2 [47]	$LiNbO_3$
	Li_2O-Nb_2O_5-TeO_2 [19]	$LiNbO_3$
	$(xNb_2O_5$-$(0.5-x)P_2O_5$-$0.5Li_2O$ [48]	$LiNbO_3$
	K_2O-Nb_2O_5-SiO_2 [49]	$KNbO_3$
	$Na_2B_4O_7$-Nb_2O_5 [50]	$NaNbO_3$
2	BaO-TiO_2-TeO_2 [41, 42]	$BaTiO_3$
	BaO-TiO_2-Al_2O_3-SiO_2 [51]	$BaTiO_3$
	PbO-TiO_2-Al_2O_3-SiO_2 [52]	$PbTiO_3$
3	SrO-BaO-Nb_2O_5-SiO_2 [44]	$Sr_{0.5}Ba_{0.5}Nb_2O_6$
	SrO-BaO-Nb_2O_5-GeO_2 [53]	$Sr_{0.5}Ba_{0.5}Nb_2O_6$
	SrO-BaO-Nb_2O_5-TeO_2 [54]	$Sr_xBa_{1-x}Nb_2O_6$
4	LiO-Ta_2O_5-Al_2O_3-SiO_2 [55]	$LiTaO_3$
	$KTa_{0.65}Nb_{0.35}O_3$ [56]	$KTa_{0.65}Nb_{0.35}O_3$
5	La_2O_3-B_2O_3-GeO_2 [57, 58]	$LaBGeO_5$

Among those crystal phases, niobate family has remained one of the most popular ferroelectric oxides not only for application using single crystal but also for active components within the glass ceramics which will be discussed in this thesis.

1.3.2 Structure of some Niobate crystalline phases

A list of ferroelectric phases containing niobium with an oxidation number +5 is shown in the Table 1.3. They show second-order nonlinearity. In all cases, niobium

is situated in octahedral NbO_6 sites which are joined by common vertexes, forming three-dimensional structural frames. The role of octahedral asymmetry in creation of nonlinear optical properties has been proved by means of the theoretical calculations [59, 60].

Table 1.3: Formulas and structures of some niobate crystals. [35, 67]

Compound	Space group	Structural type
$LiNbO_3$	R3c	Isotypic to corundum and ilmenite [61]
$KNbO_3$	Cm2m	Perovskite [62]
$NaNbO_3$	$P2_1ma$	Perovskite [63]
$Ba_2NaNb_5O_{15}$	Pba2	Tetragonal tungsten bronzes (TTB) [64, 65]
$Li_4K_5Nb_{10}O_{30}$	P4bm	TTB [35]
$Ba_{0.5}Sr_{0.5}Nb_2O_6$	P4bm	TTB [35, 66]

In comparison to potassium dihydrogen phosphate (KDP) which was the first crystal converted to commercial application, the susceptibility of niobates is much higher. For instance, $KNbO_3$ which is among the most used second-order active crystals show susceptibility up to 20pm/V (d_{31}=-11.9pm/V; d_{32}=-13.7pm/V; d_{33}=-20.6pm/V) [39, 68]. Therefore, studies on glass ceramics containing niobate crystals are of interest.

1.4 TeO_2-based glass system

1.4.1 Tellurite based glass for optical glass ceramics

Among the various oxides available as host matrices, TeO_2 are of technical interest because of their typical properties such as low melting point and absence of hygroscopic properties [69-72]. This glass family also presents high density, low transition temperature, and some advantages in optical nonlinearity like wide infrared transparency and high third-order susceptibility [70, 73]. These points, for example, limit the applications of phosphate and borate glasses [20, 73]. However,

pure TeO_2 glass is difficult to obtain and needs other ions to form bulk glasses [71]. Many studies characterized binary, ternary, and quaternary systems of TeO_2 – based glasses and consider that they are promising materials for optical applications [69]. TeO_2 – based glasses have low phonon maxima and high refractive index [74-76]. The latter is quite important to produce glass ceramics with high SONL and good optical transparency.

TeO_2–based glass formation has been shown with systems of more than 90 mol% TeO_2 and no other glass former presents [77, 78]. TeO_2-based glass systems containing BaO, Na_2O, Li_2O, and B_2O_3 were least durable when exposed to an atmosphere saturated with water vapour at around 50 to 55°C [78]. Those glasses were slightly attacked by citric acid, and sodium carbonate solution. However, heavy attack of the alkali was shown by the binary TeO_2 – PbO glasses, and the ternary lead tellurite glasses containing P_2O_5, ZnF_2, BaO, Li_2O and Na_2O, as well as the TeO_2 – BaO – As_2O_5 glasses. Glasses containing d-block oxides: MoO_3, WO_3 and Nb_2O_5 showed the best overall resistance to acid, alkali and water [78-80].

Unlike silicate glasses, TeO_2 – based glasses are composed of low-symmetry structural units such as TeO_4 trigonal bipyramids and TeO_3 trigonal pyramids [81, 82]. A common representation of the TeO_2 – based glass with structure of tellurium-oxygen sites is illustrated in Figure 1.7. The sites are interconnected by Te-O-Te bridges.

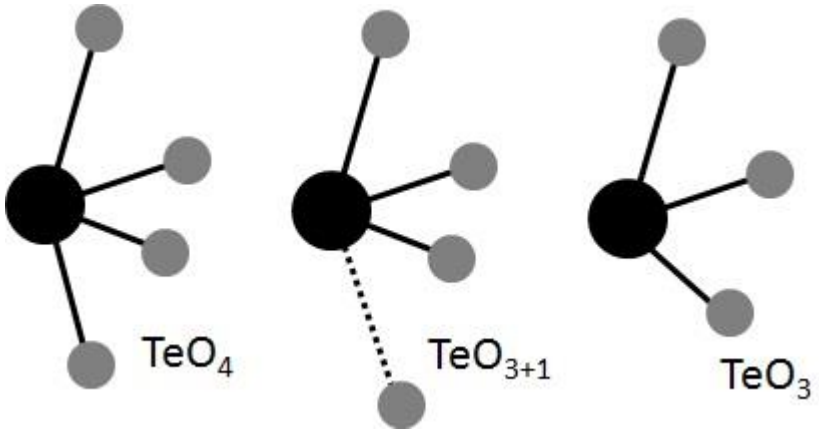

Figure 1.7: Structure of the TeO_4 tbp (a) and the TeO_{3+1}/TeO_3 tp (b) in tellurite based glasses [81, 82]

In the TeO_4 units one equatorial site of the Te sp^3d hybrid orbitals is occupied by a lone pair electron and the two equatorial and axial sites are bonded to oxygen atoms while in the case of TeO_3 units one of the Te sp^3 orbitals is occupied by the lone pair electrons [82, 83]. The nearly pure TeO_2 glass network is mainly constituted of TeO_4 units. The addition of a modifier such as Al_2O_3 or K_2O leads to depolymerization of the glass by conversion of TeO_4 units into TeO_3 units [78, 80, 82].

Recently, interest has focused on laser and nonlinear applications. In 1976, TeO_2 was first recognized as a possible host for lasing ions [84]. Comparing with silicate glasses, tellurite is more favourable due to its spectroscopic factors such as fluorescence life-times. Latter in 1980s, Elzaidia et al. [85] noted the low absorption in the spectral region beyond 2.5μm and suggested the application for low loss mid infrared optical fibers. For the nonlinear applications, TeO_2 – based glasses combined with nano ferroelectric crystals to overcome the difficulty of fabrication of single ferroelectric crystals [86].

However, low glass transition temperature (T_g) and onset of crystallisation temperature (T_x), with values ranging from ~250–350°C and ~300–550°C, respectively, can be a drawback, especially for fiber drawing applications. In fact, to achieve a large range of working temperatures, it is desired that the glass host has $\Delta T = T_x - T_g \geq 100^oC$ to be considered stable against the crystallization during fiber drawing [87].

1.4.2 TeO_2-(GeO_2)-Nb_2O_5-K_2O/Na_2O system

Before the 21st century, along with demands for useful applications in the military, security and construction, scientists concentrated on germanium oxide (GeO_2) in an effort to produce high quality infrared transmission glasses. GeO_2-based glasses are nowadays known as one of the best materials for long – wave infrared applications (LWIR), contain long transmission bandwidth up to 6μm in the infrared region. Tellurite (TeO_2) was used as a modifier to reinforce mechanical ability and prevent chemical attack but still keep similar transmission cut-off [88]. Researchers

studied and characterized TeO_2 – GeO_2 system often with ratio $GeO_2/TeO_2 > 1$ [88, 89].

During the two last decades, photonic age has flourished and led to an urgent requirement for transparent and optically active materials for optical amplification, switching, sensors, transducers, actuators and so on [30]. Scientists have focused on other more promising candidate host glass, TeO_2. As mentioned in previous section, TeO_2 – based glasses show many interesting properties such as ease of fabrication, chemical resistance and high refractive index. Many papers now focus on how to improve TeO_2 based glass by combining with other constituents. Binary and even more complex ternary and quaternary tellurite glasses have been investigated [90, 91].

Many studies on TeO_2 – GeO_2 system demonstrated that the presence of GeO_2 can improve the TeO_2 network. One of main drawback of TeO_2 – based glasses is the low thermal stability because of weaker bonding Te-O due to larger size and heavier mass of tellurite [92]. This advantage is serious for fiber application. Fiber drawing itself needs annealing of a glass preform and the crystallization increases the scattering loss of fiber and decreases the optical properties. GeO_2 has high viscosity which can enlarge the lower one of tellurite based host around the drawing temperature up to a limit to prevent the crystallization [91]. Moreover, it also helps to shift the minimum loss wavelength toward shorter wavelength and decrease fiber loss at 1.5μm [93].

According to a study of the (80-x) TeO_2 – x GeO_2 – 10 Nb_2O_5 – 10 K_2O system, Monteiro et al. has characterized this system and found the improvements in thermal stability from $\Delta T = T_x - T_p = 81^oC$ to 193^oC when adding GeO_2 up to 60% [70]. Furthermore, optical and thermal properties of those glasses were tested and they showed that this system is a potential candidate for photonic applications after fiber processing [76, 94]. The progress mainly comes from the expansion of temperature working range of tellurite glass due to the introduction of GeO_2.

Blue laser for use in colour display, optics, biomedical diagnosis and optical communication is another interesting trend of research [95, 96]. This leads to the

need of up–conversion phenomenon for compact and efficient solid state. This effect is used to describe the absorption of 2 or more photons and then emission of a photon with higher energy. The study of Kishimoto and Hirao proved that although tellurite is a well-known material for rare-earth host but the glass matrix with high phonon energy usually has a low upconversion efficiency [97]. Some studies have confirmed this observation [98, 99]. Role of GeO_2 and Nb_2O_5 in TeO_2-based glasses on up–conversion efficiency was studied and some improvements were found [100, 101].

In terms of nonlinear optical potential, TeO_2 – GeO_2 glass system was made and characterized. Second harmonic generation (SHG) in those glasses was observed by using bicolour optical poling or electrical poling. The optical nonlinear properties of the TeO_2 – GeO_2 system with a third constituent like Bi_2O_3 and PbO (maximally reported value up to 2.25 pm/V) were also discussed elsewhere [102, 103].

1.5 TeO_2 glass ceramics for optics

1.5.1 General goals for optical glass ceramics

So, for photonic applications, a transparent glass ceramic material should have [8, 30, 104]:

(a) High transparency

(b) High optical nonlinearity, especially second harmonic generation, which requires high volume fraction of the non centrosymmetric crystallized phase.

(c) Alignment of active crystallites so that the optical response can be controlled electrically.

(d) Ability of the glass matrix to make films or fibres that can be subsequently transformed into desired glass nanocomposite.

Concerning transparency, several host-glass compositions have been characterized and tested but tellurite is still one of the most interesting glass formers, because of its advantages as mentioned previously. This means that low

scattering losses at the interface between glass and crystals can be obtained and therefore high transparency.

Relationship between the light scattering intensity, refractive indices and spherical shape of dielectric particle can be expressed in the following formula [35]:

$$I(\theta) = I_o \left(\frac{1+cos^2\theta}{r^2}\right) \frac{8\pi^4}{\lambda^4} d^4 \left(\frac{\left(\frac{n_2}{n_1}\right)^2 - 1}{\left(\frac{n_2}{n_1}\right)^2 + 2}\right)^2 \quad (1.18)$$

- θ is the angle formed by the incident and scattered direction.
- I_o and I(θ) are the intensities of incident and scattered emission, correspondingly.
- r represents the distance from a scattering centre and a point of observation
- λ is the wavelength of radiation.
- d is the particle radius
- n_2 and n_1 are refractive index of the particle and the matrix, repectively.

Increasing the size of particles and the refractive index mismatch are expected to increase the scattering losses. It is noted that it is difficult to obtain a perfect match between refractive indices. Therefore, the grain size seems to be the critical factor to control the scattering intensity. Malakho et al. have claimed that in the transparent glass ceramics the size of crystal grains should not exceed 100 nm [30, 35].

Glass ceramics can be obtained through a 2-step method during the first step. Nuclei are generated and the second step allows the controlled crystal growth. The key idea of this method is to obtain the trade-off between transparency and optically nonlinear activity. As we know, larger crystals embedded within the glass are favoured but the transmittance of the glass would decrease as a sequence. The elaboration process will have to take into account the control of volume number. For this purpose, Massera et al. [81] propose the following process of elaboration. A transparent glass is first produced by rapidly quenching. In the next step, the glass is heat treated at the temperature (T_n) at which nucleation rate is

the highest. This step will assure a wide distribution of nucleus. This T_n is often recognized slightly above the glass transition temperature (T_g) and Marotta's method is usually used to define this point [26]. After a sufficiently large number of nuclei have formed, the glass (with nucleus) will be heated to higher temperature to promote the growth of the crystals (see Figure 1.4). The growth temperature and duration of thermal treatment should be chosen so that the crystallites reach a size that is consistent with sample transparency [81].

Tellurite based glass ceramics can limit the scattering by reducing the difference between refractive indices of parent glass and crystal. Effectively, tellurite-based glasses show high refractive index which can be up to 2.2 [69] and it was demonstrated to be close to many kinds of ferroelectric crystal's refractive indices such as $KNbO_3$ (~2.28 at 0.633μm) or $LiNbO_3$ (~2.21 at 0.6μm) [39, 105]. In previous studies, TeO_2-based glasses containing $LiNbO_3$, $BaTiO_3$, and $KNbO_3$ crystals have been characterized and developed [42, 105, 106]. Furthermore, some other properties are appreciated as advantages such as low melting temperature which leads to ease of production, high dielectric constants, wide infrared transmittance and high third-order NLO susceptibilities.

1.5.2 Tellurite glass ceramics for SHG

Tellurite glass ceramics containing 60-90% of TeO_2 possess special combined properties of the two components of glass and crystallites, especially nonlinear optical nature of the embedded ferroelectrics. Interest in glass ceramics for optical applications is connected with their benefits over both glasses and single crystals as new materials for SHG properties again raised [9, 107]. It makes them attractive materials for photonic applications. In 1991, Komatsu et al. applied for the first time glass ceramics based on TeO_2 in which crystals of $LiNbO_3$ were grown inside a host glass for nonlinear optics [19]. For recent years, beside some studies focusing on processing tellurite-based glass ceramics for solid state laser, most efforts have examined composition regions that exhibit low optical scattering loss and high second harmonic nature [43, 108, 109]. Tellurite-based glasses show high refractive index (n = 2.00 – 2.24 dependent on composition) which are

demonstrated to be close to many kinds of ferroelectric crystals such as $LiNbO_3$, $BaTiO_3$, or $KNbO_3$ [30, 105]. Glass compositions such as Li_2O-Nb_2O_5-TeO_2, BaO-TiO_2-TeO_2, or have been reported [41, 42, 90, 105, 110-112].

1.5.3 TeO_2 – Nb_2O_5 – (Na_2O,K_2O) system

In this section, we collect all studies related to the TeO_2 – Nb_2O_5 – (Na_2O,K_2O) glass systems because they are close to the TeO_2 – GeO_2 – Nb_2O_5 – K_2O – Ag_2O composition which will be the core of this thesis.

TeO_2-Nb_2O_5-R_2O compositions (R=Li, Na, K) seem to be the most studied [43, 106, 111-113]. Many research groups have reported studies about their mechanical, thermal and optical properties as well as rare-earth doping with Nd or Er for photo-luminescense applications [114-117]. However, the main drawback of these tellurite based glass ceramic is the preferable surface crystallization which can limit its application [9, 43].

Shioya et al. [112] have obtained a metastable intermediate crystalline phase (phase P) when trying to elaborate glass ceramics based on TeO_2-Nb_2O_5-K_2O composition (which is known as KNbTe glass). They claim a cubic structure for lattice constant a = 0.554nm.

From literature, the cubic structure phases are formed frequently as a first phase of crystallization on various glasses [105, 106, 112]. Some studies reported that the precipitation of cubic pyrochlore-type compounds were found in systems containing Nb_2O_5 such as $K_{1.5}[Ta_{0.65}Nb_{0.35}]_2O_{5.75}$ with a lattice constant a = 1.062nm [112]. Another phase with composition $KNbTeO_6$ was recorded in ternary system K_2O-Nb_2O_5-TeO_2 [112, 114]. Its lattice parameter is a=1.0249nm. Both of them are different from phase P (a=2x0.554=1.108nm). This implies that the cubic phase P is not a pyrochlore type. Other crystals have been reported in literature including cubic face-centered non-stoichiometric tellurates of Y, La and lanthanides. Its lattice constant is around 0.549-0.570nm which is quite close to the crystal phase P. This closeness suggests that the phase P could contain K^+ and Na^+.

The unknown phase P was then determined as $K[Nb_{1/3}Te_{2/3}]_2O_{4.8}$ through energy dispersive X-ray spectroscopy by Komatsu and co-workers [106, 118]. Interestingly, they also recorded small the Second Harmonic Generation signal attributed to the nanocrystallites distributed with random orientation existing in the glass ceramics [106]. In $xK_2O – (14-x)Na_2O – 14Nb_2O_5 – 72TeO_2$, x=0-12% glass ceramics, similar cubic phase P has been characterized from XRD. Crystalline chemical composition have been reported as $(K,Na)[Nb_{1/3}Te_{2/3}]_2O_{4.8}$ the ratio K/Na increasing with x and the glass ceramics show SHG except for x = 0 and precipitation of $Na[Nb_{1/3}Te_{2/3}]_2O_{4.8}$ [111, 119]. The lattice parameter a was also reported to vary from 5.544 Å to 5.566 Å for x varying from 0 to 10, according to the larger ionic radius of K^+ compared to Na^+. However, they could not explain how crystallites showing an inversion symmetry cubic structure in the structure could generate Second Harmonic signal.

A study of Jeong et al. [106, 119, 120] focused on $10K_2O – 4Na_2O – 14Nb_2O_5 – 72TeO_2$ glass ceramics has tempted to explain this contradiction provided some insight on its origin. They assumed a phase centered cubic phase in a fluorite-type structure for the phase P with chemical composition quantified as $K_{7.41}Na_{5.1}Nb_{8.11}Te_{18.79}O_{60.59}$ by using energy dispersive X-ray spectroscopy. They claimed this composition close to $(K_{0.59},Na_{0.41})(Nb_{1/3}Te_{2/3}]_2O_{4.8}$. According to this hypothesis, K+ and Na+ ions occupy the eightfold site in the fluorite structure. The structure was then schematically described as shown in **Figure 1.8**.

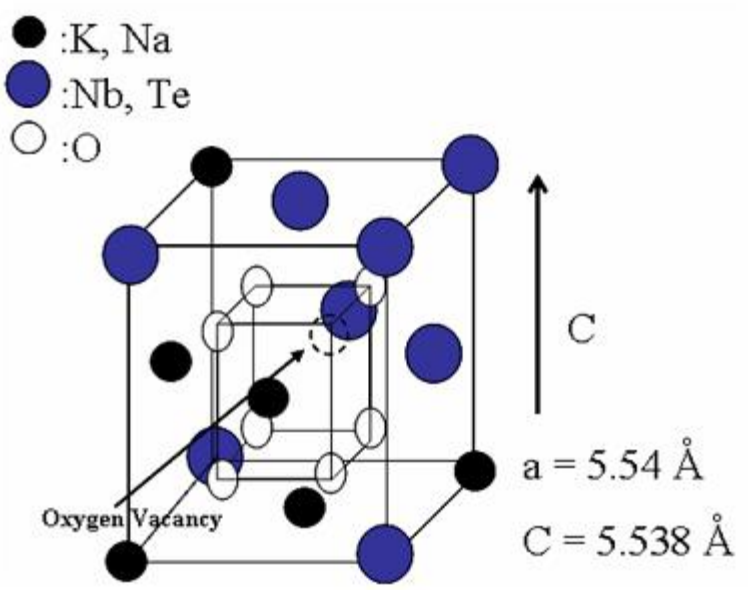

Figure 1.8: Structure of $10K_2O$-$4Na_2O$-$14Nb_2O_5$-$72TeO_2$ glass ceramics [119]

Hart and coworkers have proposed different distortion of the Face Centered Cubic (FCC) revealed by XRD patterns for the phase P which precipitates in the $15K_2O$ – $15Nb_2O_5$ – $70TeO_2$ glass ceramics [121, 122]. The lattice cell parameter a was estimated 5.54 Å. At this point they discussed the inconsistency of the fluorite-type model proposed on Figure 1.8 [121]. In this structure, the mean M-O distance is 2.4 Å, but typical M-O bond lengths in niobate and tellurite crystals are <2.2 Å. Furthermore, in the fluorite cell all the cations are coordinated by eight anions, in contradiction with 6 coordinated Nb^{5+} cation in most of niobate crystals and the 4 or 3 nearest oxygen neighbors observed in tellurite crystals. Finally, they argued the large 1.6 oxygen atoms deficiency per cell to envisage distortions from the cubic cell.

As the scattering cross-sections from oxygen are small relative to that of niobium and tellurium in XRD, they provide neutron diffraction characterizations to complete X-ray analysis. Additional broad Bragg peaks reflections were revealed from neutron diffraction data which do not fit a FCC cell. They concluded these reflection occurred form planes containing predominantly oxygen atoms with randomness in the distribution of positions. Thus this anion disorder model would help to explain the generation of SHG. Hart et al. proposed a first model of the

resulting distortion with an orthorhombic unit cell which could justify SHG [121]. Later, Hart et al. proposed another model for polymorph $K_2Te_4O_9$ in space group $P2_{1/C}$ with a tetragonal lattice [122]. This model has inversion symmetry and cannot explain SHG. Then, Jeong et al. went further with energy-dispersive X-ray spectroscopy characterization of the crystal composition definitively invalidated $K_2Te_4O_9$ proposition as Nb was clearly evidenced to be included in the composition [119]. They suggested a tetragonal distortion c/a = 1.001 from the fluorite-type structure which could explain the origin of SHG [119]. The investigators [111, 120] also assumed that atomic size of K can affect the distortion because no SHG is observed after precipitation of $Na[Nb_{1/3}Te_{2/3}]_2O_{4.8}$.

REFERENCES

1. Shelby, J.E., *Introduction to glass science and technology*. 2005: Royal Society of Chemistry.
2. Zarzicky, J., *Les verres et l'état vitreux.* Paris: Manson, 1982.
3. McMillan, P.W., *Glass-ceramics*. Non-metallic solids,. 1964, London, New York,: Academic Press. viii, 229 p.
4. Zanotto, E.D., B*right future for glass-ceramics.* American Ceramics Society Bulletin, 2010. **89**(8): p. 19-27.
5. McMillan, P.W., *Glass-ceramics*. 2d ed. Non-metallic solids. 1979, London ; New York: Academic Press. viii, 285 p.
6. Parkash, O., D. Kumar, and L. Pandey, *Glass ceramics containing ferroelectric phases.* Bulletin of Materials Science, 1986. **8**(5): p. 557-565.
7. Lewis, M.H., *Glasses and glass-ceramics*. 1989, London ; New York: Chapman and Hall. xii, 378 p.
8. Holand, W. and G.H. Beall, *Glass ceramic technology*. 2012: John Wiley & Sons.
9. Komatsu, T. and T. Honma, *Optical Active Nano-Glass-Ceramics.* International Journal of Applied Glass Science, 2013. **4**(2): p. 125-135.
10. Tao, H., X. Zhao, and Q. Liu, *Optical non-linearity in nano-and micro-crystallized glasses.* Journal of Non-Crystalline Solids, 2013. **377**: p. 146-150.
11. El-Meliegy, E. and R.v. Noort, *Glasses and glass ceramics for medical applications*. 2012, New York: Springer. xxiv, 244 p.
12. Alekseeva, I., O. Dymshits, M. Tsenter, A. Zhilin, V. Golubkov, I. Denisov, N. Skoptsov, A. Malyarevich, and K. Yumashev, *Optical applications of glass-ceramics.* Journal of Non-Crystalline Solids, 2010. **356**(52): p. 3042-3058.
13. Dejneka, M.J., *Transparent oxyfluoride glass ceramics.* Mrs Bulletin, 1998. **23**(11): p. 57-62.
14. Beall, G., *Design and properties of glass-ceramics.* Annual Review of Materials Science, 1992. **22**(1): p. 91-119.
15. Beall, G.H. and L.R. Pinckney, *Nanophase glass-ceramics.* Journal of the American Ceramic Society, 1999. **82**(1): p. 5-16.
16. Sohn, S.-B., S.-Y. Choi, and Y.-K. Lee, *Controlled crystallization and characterization of cordierite glass-ceramics for magnetic memory disk substrate.* Journal of materials science, 2000. **35**(19): p. 4815-4821.
17. Ishikawa, H., *Ultrafast all-optical signal processing devices*. Vol. 258. 2008: Wiley Online Library.
18. Franken, P., A. Hill, C. Peters, and G. Weinreich, *Generation of optical harmonics.* Physical Review Letters, 1961. **7**(4): p. 118-119.
19. Komatsu, T., H. Tawarayama, H. Mohri, and K. Matusita, *Properties and crystallization behaviors of TeO 2・LiNbO 3 glasses.* Journal of non-crystalline solids, 1991. **135**(2): p. 105-113.
20. Bach, H. and N. Neuroth, *The properties of optical glass*. 1998: Springer.
21. Yamane, M. and Y. Asahara, *Glasses for photonics*. 2000: Cambridge University Press Cambridge.
22. Wheaton, B.R. and A.G. Clare, *Evaluation of phase separation in glasses with the use of atomic force microscopy.* Journal of Non-Crystalline Solids, 2007. **353**(52): p. 4767-4778.
23. Santos, R., L.F. Santos, R.M. Almeida, J. Deubener, and L. Wondraczek, *Crystallization of niobium germanosilicate glasses.* Journal of Solid State Chemistry, 2010. **183**(1): p. 128-135.
24. Vigouroux, H., E. Fargin, A. Fargues, B.L. Garrec, M. Dussauze, V. Rodriguez, F. Adamietz, G. Mountrichas, E. Kamitsos, and S. Lotarev, *Crystallization and second harmonic generation of lithium niobium silicate glass ceramics.* Journal of the American Ceramic Society, 2011. **94**(7): p. 2080-2086.

25. Marotta, A., A. Buri, F. Branda, S. Saiello, J. Simmons, D. Uhlmann, and G. Beall, *Nucleation and crystallization in glasses, advances in ceramics.* The American Ceramic Society, 1982.
26. Marotta, A., A. Buri, and F. Branda, *Nucleation in glass and differential thermal analysis.* Journal of materials science, 1981. **16**(2): p. 341-344.
27. Ray, C.S., K.S. Ranasinghe, and D.E. Day, *Determining crystal growth rate-type of curves in glasses by differential thermal analysis.* Solid state sciences, 2001. **3**(6): p. 727-732.
28. Höland, W., V. Rheinberger, and M. Schweiger, *Control of nucleation in glass ceramics.* Philosophical Transactions of the Royal Society of London. Series A: Mathematical, Physical and Engineering Sciences, 2003. **361**(1804): p. 575-589.
29. Volmer, M., *Kinetik der phasenbildung.* 1939.
30. Jain, H., *Transparent ferroelectric glass-ceramics.* Ferroelectrics, 2004. **306**(1): p. 111-127.
31. Oprea, I.-I., *Optical properties of borate glass-ceramics*. 2005, Dissertation zur Erlangung des Grades Doktor der Naturwissenschaften, Osnabruck University, Germany.
32. Abraham, F., *Homogeneous nucleation theory: the pretransition theory of vapor condensation*. Vol. 1. 2012: Elsevier.
33. Butcher, P.N. and D. Cotter, *The elements of nonlinear optics*. Vol. 9. 1991: Cambridge University Press.
34. Verbiest, T., K. Clays, and V. Rodriguez, *Second-order nonlinear optical characterization techniques: an introduction*. 2009: CRC Press.
35. Malakho, A., *Second order optical nonlinearity in the crystals, glasses and glass-ceramic oxides containing vanadium and niobium*. 2006, Bordeaux 1.
36. Fargin, E., T. Cardinal, L. Canioni, B. Bousquet, A. Malakho, V. Rodriguez, M. Couzi, and F. Adamictz, *Second-order nonlinear optical properties in oxide photonic glasses and transparent oxide glass-ceramics by thermai poiing.*
37. Kleinman, D., *Nonlinear dielectric polarization in optical media.* Physical Review, 1962. **126**(6): p. 1977.
38. Crémoux, T., *Physico-chimie aux interfaces de systèmes vitreux à charge d'espace*. 2013, Université Sciences et Technologies-Bordeaux I.
39. Dmitriev, V.G., G.G. Gurzadyan, and D.N. Nikogosyan, *Handbook of nonlinear optical crystals*. Vol. 64. 2013: Springer.
40. Isaenko, L., I. Vasilyeva, A. Merkulov, A. Yelisseyev, and S. Lobanov, *Growth of new nonlinear crystals LiMX 2 (M= Al, In, Ga; X= S, Se, Te) for the mid-IR optics.* Journal of crystal growth, 2005. **275**(1): p. 217-223.
41. Narazaki, A., K. Tanaka, and K. Hirao, *Optical second-order nonlinearity of transparent glass-ceramics containing BaTiO 3 precipitated via surface crystallization.* Journal of materials research, 1999. **14**(09): p. 3640-3646.
42. Narazaki, A. and N. Soga, *Second harmonic generation in BaTiO3 film crystallized on tellurite glass surface.* Journal of materials science letters, 1998. **17**(13): p. 1063-1065.
43. Sakai, R., Y. Benino, and T. Komatsu, *Enhanced second harmonic generation at surface in transparent nanocrystalline TeO2-based glass ceramics.* Applied Physics Letters, 2000. **77**(14): p. 2118-2120.
44. Shyu, J.J. and J.R. Wang, *Crystallization and Dielectric Properties of SrO–BaO–Nb2O5–SiO2 Tungsten-Bronze Glass-Ceramics.* Journal of the American Ceramic Society, 2000. **83**(12): p. 3135-3140.
45. Ding, Y., A. Osaka, Y. Miura, H. Toratani, and Y. Matsuoka, *Second order optical nonlinearity of surface crystallized glass with lithium niobate.* Journal of applied physics, 1995. **77**(5): p. 2208-2210.

46. Bescher, E., Y. Xu, and J. Mackenzie, *New low temperature multiphase ferroelectric films.* Journal of Applied Physics, 2001. **89**(11): p. 6341-6348.
47. Ding, Y., Y. Miura, S. Nakaoka, and T. Nanba, *Oriented surface crystallization of lithium niobate on glass and second harmonic generation.* Journal of non-crystalline solids, 1999. **259**(1): p. 132-138.
48. De Almeida, E., J. De Paiva, and A. Sombra, *Infrared and complex dielectric function studies of LiNbO3 in niobate glass-ceramics.* Journal of materials science, 2000. **35**(6): p. 1555-1559.
49. Pernice, P., A. Aronne, V.N. Sigaev, P.D. Sarkisov, V.I. Molev, and S.Y. Stefanovich, *Crystallization behavior of potassium niobium silicate glasses.* Journal of the American Ceramic Society, 1999. **82**(12): p. 3447-3452.
50. Malakho, A., E. Fargin, M. Lahaye, B. Lazoryak, V. Morozov, G. Van Tendeloo, V. Rodriguez, and F. Adamietz, *Enhancement of second harmonic generation signal in thermally poled glass ceramic with NaNbO 3 nanocrystals.* Journal of applied physics, 2006. **100**(6): p. 063103-063103-5.
51. Yao, K., W. Zhu, L. Zhang, and X. Yao, *Structural and Electrical Characters of Sintered Ba–Ti–Al–Si Ferroelectric Glass-Ceramic Prepared From Sol–Gel Derived Powders.* Japanese journal of applied physics, 1997. **36**(7R): p. 4369.
52. Kokubo, T. and M. Tashiro, *Fabrication of Transparent $PbTiO_3$ Glass-Ceramics.* 1976.
53. Shyu, J.-J. and H.-W. Peng, *Crystallization and dielectric properties of SrO–BaO–Nb 2 O 5–GeO 2 tungsten–bronze glass–ceramics.* Journal of Materials Research, 2001. **16**(07): p. 2057-2063.
54. Kortan, A., N. Kopylov, B. Greene, and A. Glass, *Novel Ferroelectric Ceram-glass of [(SrO)(y)(BaO)(1− y)(Nb 2 O 5)](1− x) Tellurite.* Journal of materials research, 2002. **17**(05): p. 1208-1212.
55. Ito, S., T. Kokubo, and M. Tashiro, *Transparency of LiTaO3-SiO2-Al2O3 glass-ceramics in relation to their microstructure.* Journal of Materials Science, 1978. **13**(5): p. 930-938.
56. Lu, C. and A. Kuang, *Preparation of potassium tantalate niobate through sol–gel processing.* Journal of materials science, 1997. **32**(16): p. 4421-4427.
57. Truong, L.N., M. Dussauze, E. Fargin, L. Santos, H. Vigouroux, A. Fargues, F. Adamietz, and V. Rodriguez, *Isotropic octupolar second harmonic generation response in LaBGeO5 glass-ceramic with spherulitic precipitation.* Applied Physics Letters, 2015. **106**(16): p. 161901.
58. Takahashi, Y., Y. Benino, T. Fujiwara, and T. Komatsu, *Comprehensive study of crystallization and phase formation in (La, Gd) BGeO5 glass.* Journal of the Ceramic Society of Japan, 2008. **116**(1358): p. 1108-1114.
59. Halasyamani, P.S., *Asymmetric cation coordination in oxide materials: influence of lone-pair cations on the intra-octahedral distortion in d0 transition metals.* Chemistry of materials, 2004. **16**(19): p. 3586-3592.
60. Levine, B., *Bond-charge calculation of nonlinear optical susceptibilities for various crystal structures.* Physical Review B, 1973. **7**(6): p. 2600.
61. Boyd, G., R.C. Miller, K. Nassau, W. Bond, and A. Savage, *LiNbO3: an efficient phase matchable nonlinear optical material.* Applied physics letters, 1964. **5**(11): p. 234-236.
62. Nakamoto, Y., K. Ohi, T. Okada, T. Nagai, and T. Yamanaka, *The phase transitions of KNbO3 under high pressure.* Ferroelectrics, 2006. **337**(1): p. 189-195.
63. Reznitchenko, L., A. Turik, E. Kuznetsova, and V. Sakhnenko, *Piezoelectricity in NaNbO3 ceramics.* Journal of Physics: Condensed Matter, 2001. **13**(17): p. 3875.
64. Foulon, G., M. Ferriol, A. Brenier, M. Cohen, and A.G. Boulon. S*elf-frequency doubling potentiality of a new phase of neodymium-doped Ba2NaNb5O15 (BANANA)*. in *Advanced Solid State Lasers*. 1997. Optical Society of America.

65. Kundu, S. and K. Varma, *Evolution of Nanocrystalline Ba2NaNb5O15 in 2BaO–0.5 Na2O–2.5 Nb2O5–4.5 B2O3 Glass System and Its Refractive Index and Band Gap Tunability.* Crystal Growth & Design, 2013. **14**(2): p. 585-592.
66. Титаев, Д., М. Фаддеев, and Е. Чупрунов, *Влияние структурных и симметрийных особенностей кристаллов ниобата стронция–бария с различным соотношением долей sr и ba в структуре на интенсивность возбуждаемой в них второй гармоники.* 2007.
67. Atuchin, V., B. Kidyarov, and N. Pervukhina, *Shortest chemical bond length as a criterion for searching new noncentrosymmetric niobate and tantalate crystals with high optical nonlinearity.* Journal of Crystal Growth, 2005. **275**(1): p. e1941-e1946.
68. Zysset, B., I. Biaggio, and P. Günter, *Refractive indices of orthorhombic KNbO 3. I. Dispersion and temperature dependence.* JOSA B, 1992. **9**(3): p. 380-386.
69. El-Mallawany, R.A., *Tellurite glasses handbook: physical properties and data*. 2011: CRC press.
70. Monteiro, G., L.F. Santos, J. Pereira, and R.M. Almeida, *Optical and spectroscopic properties of germanotellurite glasses.* Journal of Non-Crystalline Solids, 2011. **357**(14): p. 2695-2701.
71. El-Mallawany, R., *Tellurite glasses part 1. elastic properties.* Materials chemistry and physics, 1998. **53**(2): p. 93-120.
72. Rada, S., E. Culea, V. Rus, M. Pica, and M. Culea, *The local structure of gadolinium vanado-tellurite glasses.* Journal of Materials Science, 2008. **43**(10): p. 3713-3716.
73. Dussauze, M., T. Cremoux, F. Adamietz, V. Rodriguez, E. Fargin, G. Yang, and T. Cardinal, *Thermal Poling of Optical Glasses: Mechanisms and Second-Order Optical Properties.* International Journal of Applied Glass Science, 2012. **3**(4): p. 309-320.
74. Idalgo, E., E. Araújo, K. Yukimitu, J. Moraes, V. Reynoso, and C. Carvalho, *Effects of the particle size and nucleation temperature on tellurite 20Li2O–80TeO2 glass crystallization.* Materials Science and Engineering: A, 2006. **434**(1): p. 13-18.
75. Blanchandin, S., P. Thomas, P. Marchet, J.C. Champarnaud-Mesjard, and B. Frit, *Equilibrium and non-equilibrium phase diagram within the TeO 2-rich part of the TeO 2-Nb 2 O 5 system.* Journal of Materials Chemistry, 1999. **9**(8): p. 1785-1788.
76. Monteiro, G., L.F. Santos, R.M. Almeida, and F. D'Acapito, *Local structure around Er 3+ in GeO 2–TeO 2–Nb 2 O 5–K 2 O glasses and glass-ceramics.* Journal of Non-Crystalline Solids, 2013. **377**: p. 129-136.
77. Vogel, W., *Glass chemistry.* 1979.
78. O'Donnell, M.D., *Tellurite and fluorotellurite glasses for active and passive fibreoptic waveguides*. 2004, University of Nottingham.
79. Stanworth, J., *Tellurite glasses.* 1952.
80. Lasbrugnas, C., P. Thomas, O. Masson, J.-C. Champarnaud-Mesjard, E. Fargin, V. Rodriguez, and M. Lahaye, *Second harmonic generation of thermally poled tungsten tellurite glass.* Optical Materials, 2009. **31**(6): p. 775-780.
81. Massera, J., *Nucleation and growth behavior of tellurite-based glasses suitable for mid-infrared applications.* 2009.
82. Tatsumisago, M., S.-K. Lee, T. Minami, and Y. Kowada, *Raman spectra of TeO< sub> 2</sub>-based glasses and glassy liquids: local structure change with temperature in relation to fragility of liquid.* Journal of non-crystalline solids, 1994. **177**: p. 154-163.
83. Fargin, E., A. Berthereau, T. Cardinal, G. Le Flem, L. Ducasse, L. Canioni, P. Segonds, L. Sarger, and A. Ducasse, *Optical non-linearity in oxide glasses.* Journal of non-crystalline solids, 1996. **203**: p. 96-101.
84. Dimitriev, Y., E. Kaschieva, and E. Gurov, *Phase diagram of the TeO 2 · GeO 2 system.* Materials Research Bulletin, 1976. **11**(11): p. 1397-1403.

85. El-Zaidia, M., A. Ammar, and R. El-Mallwany, *Infra-Red Spectra, Electron Spin Resonance Spectra, and Density of (TeO2) 100− x–(WO3) x and (TeO2) 100− x–(ZnCl2) x Glasses.* physica status solidi (a), 1985. **91**(2): p. 637-642.
86. Manning, S., *A study of tellurite glasses for electro-optic optical fibre devices.* 2011.
87. Stepien, R., R. Buczynski, D. Pysz, I. Kujawa, A. Filipkowski, M. Mirkowska, and R. Diduszko, *Development of thermally stable tellurite glasses designed for fabrication of microstructured optical fibers.* Journal of Non-Crystalline Solids, 2011. **357**(3): p. 873-883.
88. Nielsen, S., W. Lawson, and A. Fray, *Some infrared transmitting glasses containing germanium dioxide.* Infrared Physics, 1961. **1**(1): p. 21-26.
89. Ahmed, M., C. Hogarth, and M. Khan, *A study of the electrical and optical properties of the GeO2-TeO2 glass system.* Journal of materials science, 1984. **19**(12): p. 4040-4044.
90. Blanchandin, S., P. Marchet, P. Thomas, J. Champarnaud-Mesjard, B. Frit, and A. Chagraoui, *New investigations within the TeO2-WO3 system: phase equilibrium diagram and glass crystallization.* Journal of materials science, 1999. **34**(17): p. 4285-4292.
91. Jose, R. and Y. Ohishi, *Higher nonlinear indices, Raman gain coefficients, and bandwidths in the TeO 2–ZnO–Nb 2 O 5–MoO 3 quaternary glass system.* Applied physics letters, 2007. **90**(21): p. 211104-211104-3.
92. Yang, Z., S. Xu, J. Yang, L. Hu, and Z. Jiang, *Thermal analysis and optical transition of Yb3+, Er3+ co-doped lead–germanium–tellurite glasses.* Journal of materials research, 2004. **19**(06): p. 1630-1637.
93. Feng, X., S. Tanabe, and T. Hanada, *Spectroscopic Properties and Thermal Stability of Er3+-Doped Germanotellurite Glasses for Broadband Fiber Amplifiers.* Journal of the American Ceramic Society, 2001. **84**(1): p. 165-171.
94. Monteiro, G., Y. Li, L.F. Santos, and R.M. Almeida, *Optical and spectroscopic properties of rare earth-doped (80-x) TeO2-xGeO2-10Nb2O5-10K2O glasses.* Journal of Luminescence, 2013. **134**(Complete): p. 284-296.
95. Scheps, R., *Upconversion laser processes.* Progress in Quantum Electronics, 1996. **20**(4): p. 271-358.
96. Agrawal, G., *Applications of nonlinear fiber optics*. 2001: Academic press.
97. Kishimoto, S. and K. Hirao, *Intense ultraviolet and blue upconversion fluorescence in Tm3+-doped fluoroindate glasses.* Journal of applied physics, 1996. **80**(4): p. 1965-1969.
98. Tsang, W., W. Yu, C. Mak, W. Tsui, K. Wong, and H. Hui, *Evidence of the influence of phonon density on Tm3+ upconversion luminescence in tellurite and germanate glasses.* Journal of applied physics, 2002. **91**(4): p. 1871-1874.
99. Yang, J., L. Zhang, L. Wen, S. Dai, L. Hu, and Z. Jiang, *Optical transitions and upconversion luminescence of Er3+/Yb3+-codoped halide modified tellurite glasses.* Journal of applied physics, 2004. **95**(6): p. 3020-3026.
100. Shen, X., Q. Nie, T. Xu, S. Dai, G. Li, and X. Wang, *Effect of Ce3+ on the spectroscopic properties in Er3+ doped TeO2-GeO2-Nb2O5-Li2O glasses.* Journal of luminescence, 2007. **126**(2): p. 273-277.
101. Zhao, C., G. Yang, Q. Zhang, and Z. Jiang, *Spectroscopic properties of GeO2 and Nb2O5 modified tellurite glasses doped with Er3+.* Journal of Alloys and Compounds, 2008. **461**(1): p. 617-622.
102. Kassab, L., R. de A Pinto, R. Kobayashi, M. Piasecki, P. Bragiel, and I. Kityk, *Photoinduced non-linear optics of Eu2O3 doped TeO2–GeO2–PbO glasses.* Journal of Physics D: Applied Physics, 2007. **40**(6): p. 1642.
103. Shivachev, B.L., T. Petrov, H. Yoneda, R. Titorenkova, and B. Mihailova, *Synthesis and nonlinear optical properties of TeO2–Bi2O3–GeO2 glasses.* Scripta Materialia, 2009. **61**(5): p. 493-496.
104. Beall, G. and D. Duke, *Transparent glass-ceramics.* Journal of Materials Science, 1969. **4**(4): p. 340-352.

105. Kim, H.G., T. Komatsu, R. Sato, and K. Matusita, *Crystallization of LiNbO< sub> 3</sub> in tellurite glasses.* Journal of non-crystalline solids, 1993. **162**(1): p. 201-204.
106. Kim, H.G., T. Komatsu, K. Shioya, K. Matusita, K. Tanaka, and K. Hirao, *Transparent tellurite-based glass-ceramics with second harmonic generation.* Journal of non-crystalline solids, 1996. **208**(3): p. 303-307.
107. Vigouroux, H., E. Fargin, S. Gomez, B. Le Garrec, G. Mountrichas, E. Kamitsos, F. Adamietz, M. Dussauze, and V. Rodriguez, *Synthesis and Multiscale Evaluation of LiNbO3-Containing Silicate Glass-Ceramics with Efficient Isotropic SHG Response.* Advanced Functional Materials, 2012. **22**(19): p. 3985-3993.
108. Hart Jr, R.T., *Structures and optical properties of tellurite glasses and glass ceramics*. 2004.
109. Prasad, N.S., J. Wang, R. Pattnaik, H. Jain, and J. Toulouse, *Preform fabrication and drawing of KNbO3 modified tellurite glass fibers.* Journal of non-crystalline solids, 2006. **352**(6): p. 519-523.
110. Kim, H.G., T. Komatsu, R. Sato, and K. Matusita, *Incorporation of LiNbO3 crystals into tellurite glasses.* Journal of Materials science, 1996. **31**(8): p. 2159-2164.
111. Kim, H. and T. Komatsu, *Fabrication and properties of transparent glass-ceramics in Na2O-Nb2O5-TeO2 system.* Journal of materials science letters, 1998. **17**(13): p. 1149.
112. Shioya, K., T. Komatsu, H.G. Kim, R. Sato, and K. Matusita, *Optical properties of transparent glass-ceramics in K2O・Nb2O5・TeO2 glasses.* Journal of non-crystalline solids, 1995. **189**(1): p. 16-24.
113. Jeong, E., J. Bae, T. Hong, K. Lee, B. Ryu, T. Komatsu, and H. Kim, *Thermal properties and crystallization kinetics of tellurium oxide based glasses.* Journal of Ceramic Processing Research, 2007. **8**(6): p. 417.
114. Komatsu, T. and K. Shioya, *Role of Te valence on phases crystallized in K 2 O–Nb 2 O 5–TeO 2 glasses.* Journal of non-crystalline solids, 1997. **209**(3): p. 305-308.
115. Komatsu, T., K. Shioya, and H. Kim, *Thermal stability and optical properties of K2O-Nb2O5-TeO2 glasses.* Physics and chemistry of glasses, 1997. **38**(4): p. 188-192.
116. Torres, F., Y. Benino, T. Komatsu, and C. Lavelle, *Mechanical and elastic properties of transparent nanocrystalline TeO2-based glass-ceramics.* Journal of materials science, 2001. **36**(20): p. 4961-4967.
117. Gonçalves, M.C., L.F. Santos, and R.M. Almeida, *Rare-earth-doped transparent glass ceramics.* Comptes Rendus Chimie, 2002. **5**(12): p. 845-854.
118. Komatsu, T., *Design and control of crystallization in oxide glasses.* Journal of Non-Crystalline Solids, 2015. **428**: p. 156-175.
119. Jeong, E., J. Bae, M. Ha, H. Kim, H. Pak, B. Ryu, and T. Komatsu, *Structure of a nanocrystalline phase with second harmonic generation.* JOURNAL-KOREAN PHYSICAL SOCIETY, 2007. **51**: p. S32.
120. Jeong, E.D., P.H. Borse, J.S. Lee, M.G. Ha, H.K. Pak, T. Komatsu, and H.G. Kim, *Second harmonic generation and fabrication of transparent K2O-Na2O-Nb2O5-TeO2 glass-ceramics.* Journal of Industrial and Engineering Chemistry, 2006. **12**(5): p. 790-4.
121. Hart, R.T., M.A. Anspach, B.J. Kraft, J.M. Zaleski, J.W. Zwanziger, P.J. DeSanto, B. Stein, J. Jacob, and P. Thiyagarajan, *Optical implications of crystallite symmetry and structure in potassium niobate tellurite glass ceramics.* Chemistry of materials, 2002. **14**(10): p. 4422-4429.
122. Hart, R.T., J.W. Zwanziger, and P.L. Lee, *The crystalline phase of (K 2 O) 15 (Nb 2 O 5) 15 (TeO 2) 70 glass ceramic is a polymorph of K 2 Te 4 O 9.* Journal of non-crystalline solids, 2004. **337**(1): p. 48-53.

CHAPTER 2 – EXPERIMENTAL TECHNIQUES AND MODELING OF SHG PRINCIPLES

Contents

CHAPTER 2 – EXPERIMENTAL TECHNIQUES AND MODELING OF SHG PRINCIPLES

2.1 Introduction

This chapter is divided into 2 separated parts. Besides the first part concerning experimental techniques and conditions which were used to characterize the materials, the second part will develop a methodology to correlate the macroscopic SHG response of a glass ceramics with the micro-SHG signals and crystallite micro-organization. The model is based on the correlation between the nonlinear response and structural properties of two glass ceramic systems which are $LiNbO_3/SiO_2$ (LNS) and $25La_2O – 25B_2O_3 – 50GeO_2$ (LBG). Those two glass ceramics compositions were developed by Vigouroux et al. [1-3].

2.2 Experimental techniques

2.2.1 Density and refractive index

Density of all samples was obtained by using Archimedes method. Their mass was measured by a scale or balance while the volume was measured directly by dipping the sample in to a fluid (hereafter toluene, ρ=0.870 g/cm^3). The quantification was carried out at room temperature (25^{o}C).

A Spectroscopic Phase Modulated Ellipsometer (Horiba Jobin-Yvon, Uvisel) was used to determine the refractive indices of polished glass samples. Their thickness was kept at around 1 mm. The experiment was performed in the 200-1100 nm spectral range at an angle of 70°. The optical constants were defined by the minimization of the mean square deviation between the calculated and the experimental data using the DeltaPsi2 software package provided by Jobin-Yvon.

2.2.2 Thermal analysis (DSC)

Differential Scanning Calorimetry (DSC) scans were performed to determine their thermal characteristics of transition temperature T_g and onset crystallization temperature T_x. All glass samples were crushed into fine powder or small pieces with 1-2 mm size to analyse the behavior of surface and bulk crystallization, which is respectively due to high or low ratio of surface areas. The sample weight ranged from 30-40mg. The heating rate was 20°C/min. The accuracy is $\pm 2K$.

2.2.3 Structural characterizations (Raman, XRD)

Local structure analysis of glasses was carried out by Raman spectroscopy. The Raman system, a LabRAM HR 800 Evolution from Horiba, consists of a diode laser (Ventus) working at 532 nm and a Peltier-cooled Horiba Symphony II CCD detector with 1024 x 256 pixels. The Raman spectra of those glasses with different amount of silver oxide were collected from 300cm^{-1} to 1000cm^{-1}.

Crystalline phase characterization was obtained from X-ray diffraction. X-ray diffraction was performed with a Philips X'PERT APD to analyse the crystalline phases of the heat-treated glass samples in air, at room temperature, using Cu Kα radiation. The step angle was fixed to 0.017°. Time per step is 59s for the case of normal scan and 699s for the one of long acquisition.

2.2.4 Imaging (OM, SEM, TEM)

Optical microscope labelled Leica was used to observe the surface and particles in the volume of samples. The digital image was captured by CCD camera (charge-coupled device). There are two objective lenses with magnification of 10x and 50x.

CAMECA microprobe SX 100 has a 10 ppm detection limit (parts per million), from the sodium. The size of the probe is 1 μm³. The device allows making quantitative composition profiles, X maps or local composition measurements on all inorganic materials. WDS spectrometry has the advantage of a spectral resolution 5-10 times better than that of EDS, usually used in scanning microscopy, which provides reliable results with an accuracy of about 1 to 2% (relative) of the basic chemical composition.

Transmission electron microscopy test was carried out in CEMHTI (Orléans) with the help of Mathieu Allix, researcher in CNRS. The TEM data were collected on a Philips CM20 microscope fitted with an Oxford energy dispersive spectrometry (EDS) analyser. To avoid any evolution of the sample under the electron beam, the experiments were run at 80keV.

2.2.5 Optical characterizations (UV-Vis and macro-SHG)

Optical transmittance spectra (UV-Vis) were recorded on optically polished 1mm-thick samples at room temperature using a double-beam spectrophotometer (CARY) in the wavelength range 200-800nm.

In the thesis' work, the macroscopic SHG measurements were done in the transmission mode. The experiment of Maker Fringes consists of the irradiation of a laser beam (frequency ω) to a sample and the record of the SHG signal ($I_{2\omega}$) generated by the sample as a function of the angle between the propagation vector and x-axis (θ) or the polarization angle of the electric field (Ψ). The principle of this measurement is illustrated in the general following **Figure 2.1**:

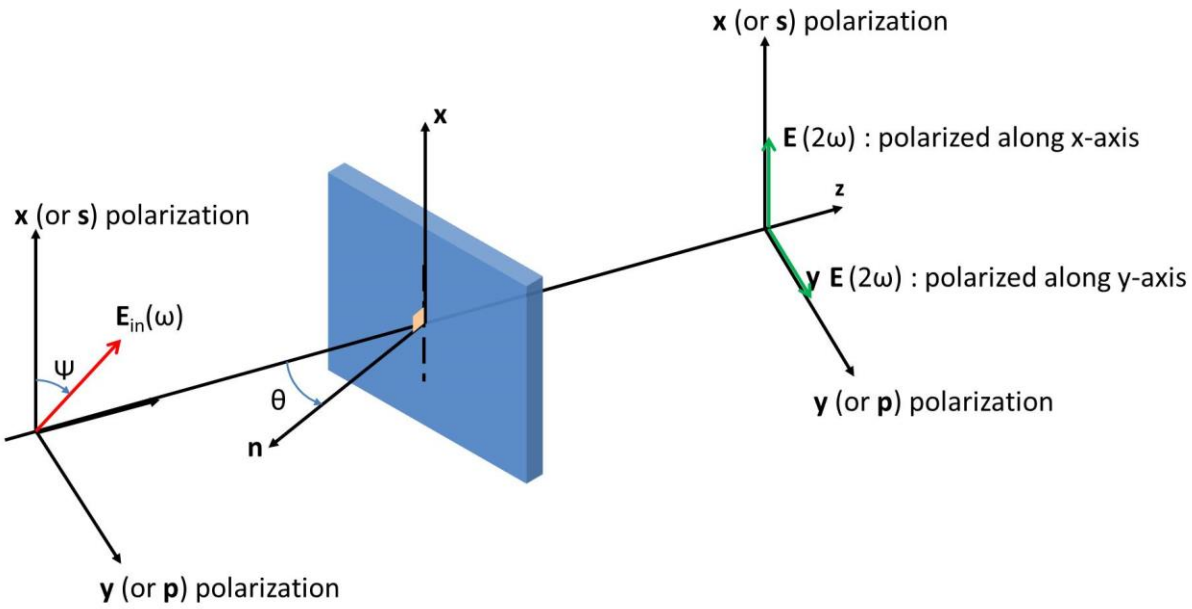

Figure 2.1: Scheme of principle in Maker Fringes experiment. In θ scans, the polarized beam and detector are fixed while the sample will rotate around the x-axis. In Ψ scans, the sample is fixed while the polarization of electric field is rotated around the z-axis. Normally, we use p and s to describe the parallel (with the plane of incidence) and perpendicular (with the plane of incidence) polarization. In Chapter 2, x and y will replace s and p to facilitate the modeling description. n is the normal vector of the sample's surface.

Transmission measurement mode that we call θ scans can be performed for different polarizations of incident and transmitted beams in function of rotating the sample of an angle θ. Usually, we measure θ_{ss}, θ_{sp}, θ_{pp}, and θ_{ps} which can be noted in function of lab referential orientation θ_{xx}, θ_{xy}, θ_{yy}, and θ_{yx}, respectively. In the notations, the first letter represents the polarized incident pump beam and the second letter is for the analysed polarization of the second harmonic beam. The sample would be rotated for θ variation from -80 degree to 80 degree.

The transmission measurements that we call Ψ scans consist in continuous polarization scans of the input beam for a fixed incidence angle θ. For this purpose, the fundamental beam, initially polarized out of the plane of incidence (x direction) goes through a combination of a rotating half wave plate (Ψ/2 angle of continuous rotation) leading to Ψ rotation of the polarization and a fixed quarter wave plate (vertical fast axis inducing π/2 phase shift). All possible polarizations are then continuously addressed, from linear to elliptical and to circular

polarization. The incident beam is focused on the sample with a spot size of 100µm and the transmitted second harmonic light is resolved into components polarized parallel (y or p polarization) and perpendicular (x or s polarization) to the horizontal plane of incidence leading to so-called Ψ_p (or Ψ_y) and Ψ_s (or Ψ_x) patterns. The excitation was performed using a spectra physics Nd:YAG laser 1064nm, 20Hz, 20ns pulses with a typical energy of 250µJ. More details can be found elsewhere [1, 4].

2.2.6 Micro-SHG/micro-Raman

Correlation between local SHG signal and local structural symmetry of the crystalline phases in glass ceramics could be recognized by the combination of micro-Raman and micro-SHG analysis with respect to the positions and orientations of the crystals.

The experiment set up was based on a modified micro-Raman (HR 800, Horiba/Jobin-Yvon) instrument equipped with two laser sources, (i) a picosecond laser at 1064nm for SHG measurement; (ii) a continuous 532 nm source for Raman. Confocal microscopy and motorized stages (X, Y, Z) allow the 3D imaging of both Raman and SHG signals. The micro-Raman spectra were recorded with a typical spectral resolution of 2.5 cm^{-1} in the backscattering geometry at room temperature [5]. The setup scheme is illustrated in **Figure 2.2** below.

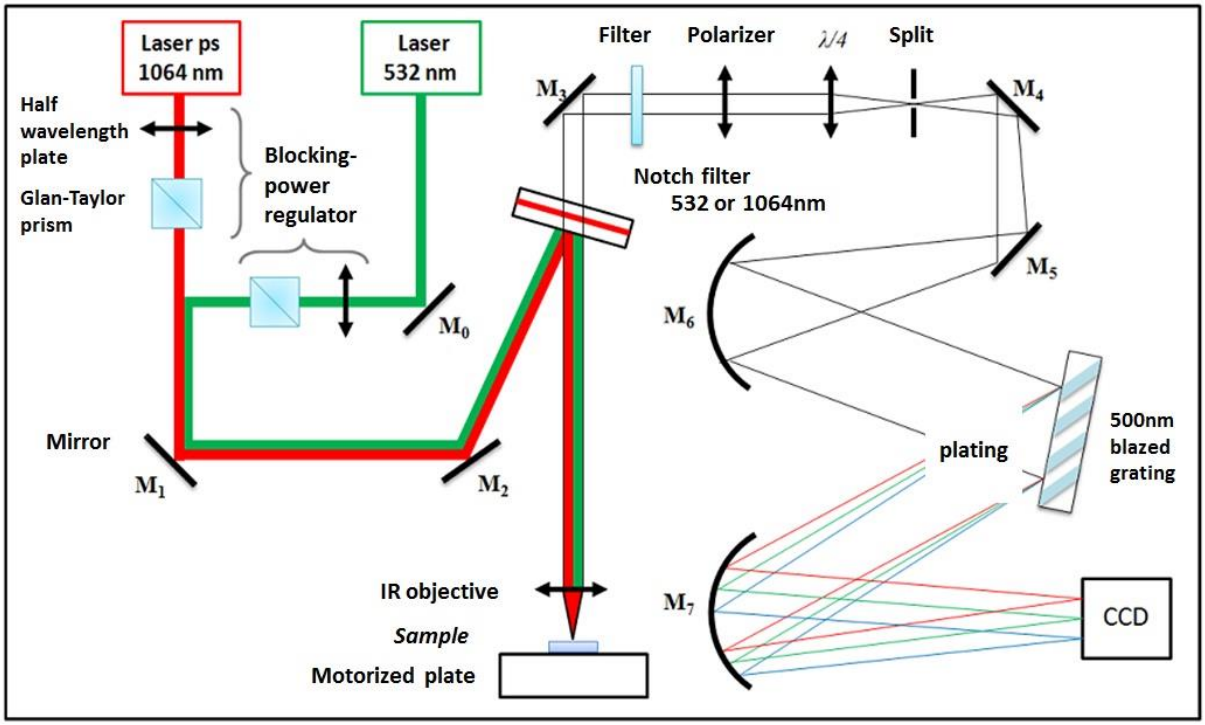

Figure 2.2: Scheme of micro-SHG /micro- Raman setup [6]. The red and green lines represent the laser beam with 1064nm and 532nm wavelength, respectively. The 1064nm laser beam is used for micro-SHG analysis and the 532nm one is used for Raman scattering analysis. The notch filter can be changed to collect the selective signal and eliminate the excitation beam.

The polarized incident beam (direction y) is reflected from a notch filter and is then focussed on the sample surface by using a near infrared objective (50x or 100x). The reflected or scattered light (micro-SHG or micro-Raman, respectively) is collected by the same objective. Then, the micro-SHG or micro-Raman signal is redirected through the selective notch filter to eliminate the reflected excitation light. An analyser selects the polarization of analysis (vertical (y) or horizontal (x)). The polarized reflected analysed beam is directed to a blazed grating before transferring to a CCD camera. The reflection spectrum as a function of wavelength can be viewed from a display device.

Figure 2.3 illustrates the surveyed terms depending on the crystal orientation. In this scheme, the polarization analysis (of the wave at 2ω), is given by the index i. The polarizations of the two incident photons ω are given by the indices j and k.

Depending on the orientation of crystallites, we could obtain the information of $\chi^{(2)}_{yyy}$, $\chi^{(2)}_{xyy}$, $\chi^{(2)}_{xxx}$, and $\chi^{(2)}_{yxx}$.

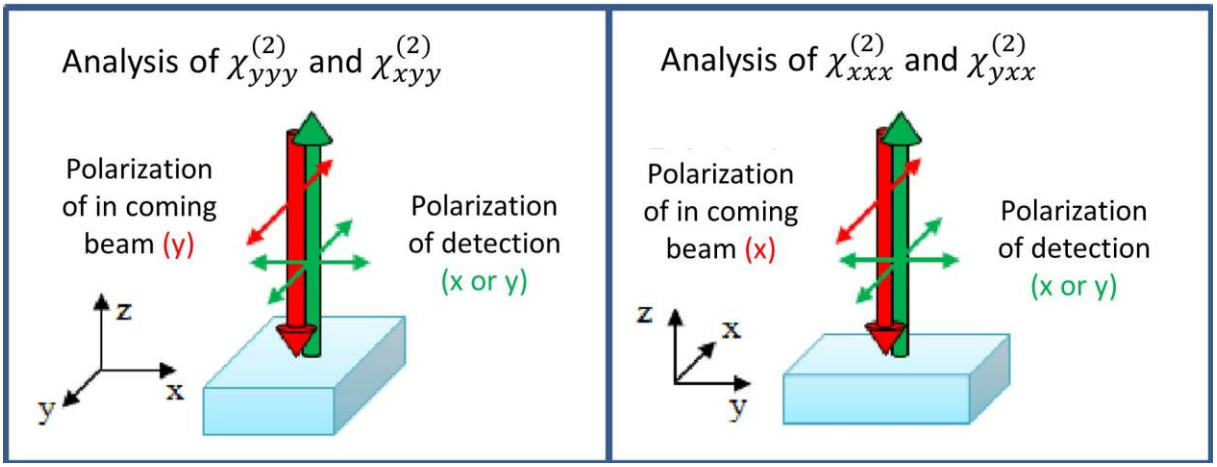

Figure 2.3: Illustration of the analyzed scheme where the detected micro-SHG results are dependent on the orientation of crystallites [6].

2.3 Multiscale-approach to investigate the glass ceramics SHG responses

2.3.1 Introduction

Studies on functional glass ceramics with second order optical properties have been focused on the optimization of second harmonic generation responses and transparency [7, 8]. As an example, research efforts have been done to control precipitation of crystals in the niobate family like $LiNbO_3$, $KNbO_3$ or $NaNbO_3$ in silicate glassy matrix [1, 9, 10]. Although the nonlinear optical properties of such crystalline phases are well known, glass ceramics usually contains poly-crystals randomly oriented which do not allow any optimization of the nonlinear optical properties.

Therefore, the first issue can be to control organization and/or orientation of crystallites within glass ceramics. Laszlo et al. [11-14] have shown that the crystal growth can be induced inside phase separated spherulites. According to a first mechanism, the spherulite is formed via central isotropic multidirectional growth. A second mechanism has been suggested in which the formation of spherulite is due

to folded-chains of single crystal via unidirectional growth and low angle branching. Such approach can promote specific orientation of crystallites within a glass ceramic. Recently, Vigouroux et al. [1-3] have shown that the precipitation of $LiNbO_3$ in silicate glass (LNS) and $LaBGeO_5$ in borogermanate glass (LBG) with the same composition can be growth within phase separated spherulite domains. Correlative micro-Raman/micro-SHG characterizations have been used to determine crystallites organization and allowed to make the correlation with SHG properties. They evidenced the radial distribution of the elementary crystalline particles for both LNS and LBG. The non-linear optical signal was then related to coherent SH effects occurring inside each spherulite and linked to the spherulite size with respect to the wavelength and the coherent length avoiding cancellation effects expected in a spherical system [1]. Interestingly, second order optical properties have been found to be isotropic at the macro scale which is potentially interesting for applications.

Vigouroux et al. [2] developed the crystallization of nonlinear $LaBGeO_5$. In the LBG system, macro SHG induced by $LaBGeO_5$ spherulites showed surprisingly different behavior when compared to LNS system. So it was necessary to develop a methodology allowing a complete correlation of multi-scale experimental characterizations. This would lean on a mathematical model which can simulate the global SHG response of a glass ceramic depending on (i) crystallite organization and (ii) single crystal properties. The next chapter details this approach for the two systems $LiNbO_3/SiO_2$ (LNS) and $LaBGeO_5$ (LBG) glass ceramics previously studied by Vigouroux et al. [1-3].

2.3.2 Mathematical description of macroscopic SHG Ψ-scan measurements

We express the parallel and perpendicular component of the NLO polarization according to the lab frame depicted in Figure 2.1):

$$P_i^{2\omega}(\Psi) = \chi_{i;x,x}^{(2)}(E_x^{\omega})^2 + \chi_{i;y,y}^{(2)}(E_y^{\omega})^2 + 2\chi_{i;x,y}^{(2)}E_x^{\omega}E_y^{\omega} \quad (2.1)$$

with $i = x, y$

The incident electric field components are given by

$$E_{\mathrm{y}}^{\omega} = E_o^{\omega} \sin(\Psi) \cos\left(\omega t + \frac{\pi}{2}\right)$$

$$E_{\mathrm{x}}^{\omega} = E_o^{\omega} \cos(\Psi) \cos(\omega t) \tag{2.2}$$

Where $\Psi/2$ is the angle of the half wave plate and the phase shift $\pi/2$ is induced by the quarter wave plate and E_o is the incident electric field amplitude. After combining Eq. 2.1 and 2.2 and time averaging the calculus, we obtain the final expression:

$$I_{\Psi i}^{2\omega} \propto \left|P_i^{2\omega}(\Psi)\right|^2 = (E_o^{\omega})^4/8 \left| \left(\chi_{i;x,x}^{(2)}\right)^2 cos^4(\Psi) + \left(\chi_{i;y,y}^{(2)}\right)^2 sin^4(\Psi) + 2\left(2\left(\chi_{i;x,y}^{(2)}\right)^2 - \chi_{i;x,x}^{(2)}.\chi_{i;y,y}^{(2)}\right) \sin^2(\Psi)\cos^2(\Psi) \right| \tag{2.3}$$

This calculation is general for all glass ceramic systems to simulate their macroscopic SHG responses. Based on this equation, one could recognize that behavior of the responses belong to the relative ratio of coefficients of the three trigonometric terms, i.e. $\left(\chi_{i;x,x}^{(2)}\right)^2$ (A), $\left(\chi_{i;y,y}^{(2)}\right)^2$ (B) and $2\left(2\left(\chi_{i;x,y}^{(2)}\right)^2 - \chi_{i;x,x}^{(2)}.\chi_{i;y,y}^{(2)}\right)$ (C). There are several possibilities, among them:

- If 2AB > C, the principal terms are in the main direction of incident and analysed polarization. The SHG response is mainly dipolar (**Figure 2.4**, red patterns).
- If 2AB < C, the crossed term (two excitation with two different polarization) starts to be predominant. The SHG response is mainly octupolar (Figure 2.4, green patterns).

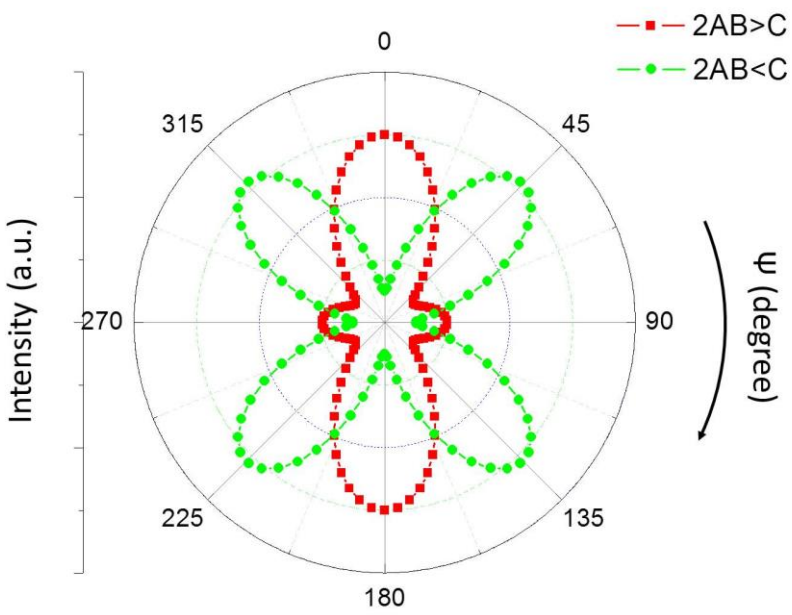

Figure 2.4: SHG responses with dipolar property (2AB>C) and octupolar property (2AB<C)

This calculation can be applied to the following LNS and LBG glass ceramic systems.

2.3.3 $Li_2O – Nb_2O_5 – SiO_2$ (LNS) glass ceramics

The LNS glass ceramic sample was elaborated from 2-step heat treatment. The heat process includes a first nucleation step done at 620°C during 1h and followed by a crystal growth step at 690°C (between T_g and T_x) during 75 min. The obtained LNS glass ceramic contains 25-35µm size spherulites. **Figure 2.5** shows a typical spherulite within the silicate matrix. The transparency of the glass ceramics is very high which is close to the mother as pristine glass. Conditions of glass elaboration and its characteristics can be found elsewhere [1-3].

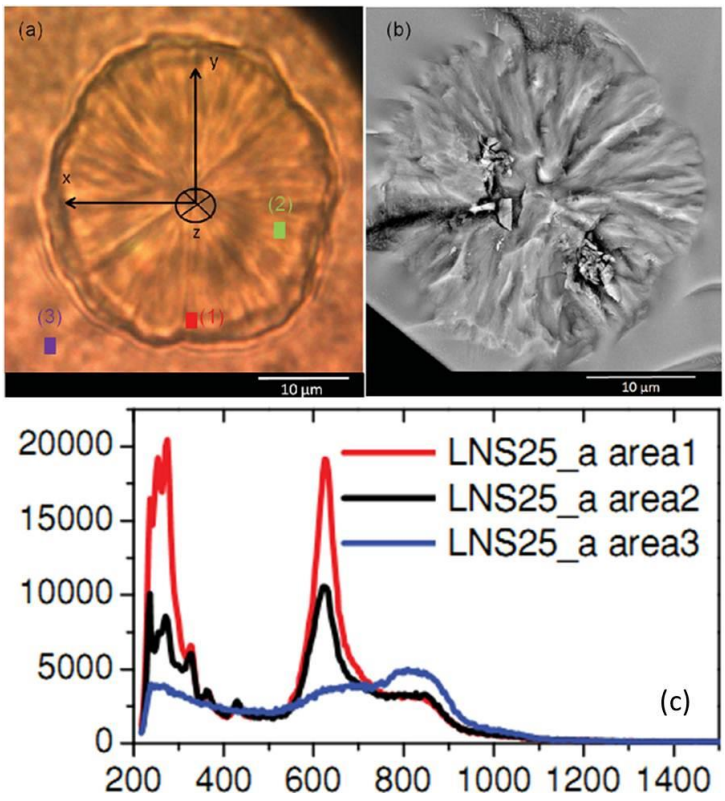

Figure 2.5: Typical spherulite of LNS glass ceramics observed through (a) an optical microscope and (b) an SEM; (c) the polarized Raman spectra at different positions in (a).

The precipitation of the unique crystalline phase $LiNbO_3$ has been investigated with micro-Raman spectroscopy inside and outside the spherulite. Sharp peaks merge in the spectra obtained only inside the spherulite (area 1 and area 2 in the Figure 2.5c), which are attributed to $LiNbO_3$ crystal phase.

The orientation of the crystallites within the spherulite was further quantified by imaging the micro-Raman signal registered in the domain 230-300 cm^{-1} inside the spherulite where the $LiNbO_3$ single crystal response is the most sensible to its orientation. The authors [1] have demonstrated radial c-axis orientation of $LiNbO_3$ crystallites within the spherulite (see Figure 2.5). More detail can be found in [1, 2].

In terms of nonlinear properties, $LiNbO_3$ is an SHG-active crystal with one dominant d_{33} nonlinear coefficient and dipolar behavior. The lithium niobate class symmetry is C_{3v} and the nonlinear coefficients reported are: d_{33} = 34.4 pm/V, d_{31} = 5.95 pm/V, and d_{22} = 2.76 pm/V [2, 15, 16].

$$C_{3v}: \begin{pmatrix} 0 & 0 & 0 & 0 & d_{31} & \overline{d_{22}} \\ \overline{d_{22}} & d_{22} & 0 & d_{31} & 0 & 0 \\ d_{31} & d_{31} & d_{33} & 0 & 0 & 0 \end{pmatrix} \quad (2.4)$$

The micro-SHG mapping has demonstrated the correlation with polarized micro-Raman mapping characterizations where one can observe in both cases the rotation of maximum signal with the rotation of the excitation polarization (**Figure 2.6**). Therefore, correlated micro-SHG and micro-Raman characterizations allow to conclude that d_{33} component of $LiNbO_3$ crystallites within the spherulite domains is effectively predominant (dipolar behavior) to explain the microscopic SHG signal evolution inside the spherulite [1].

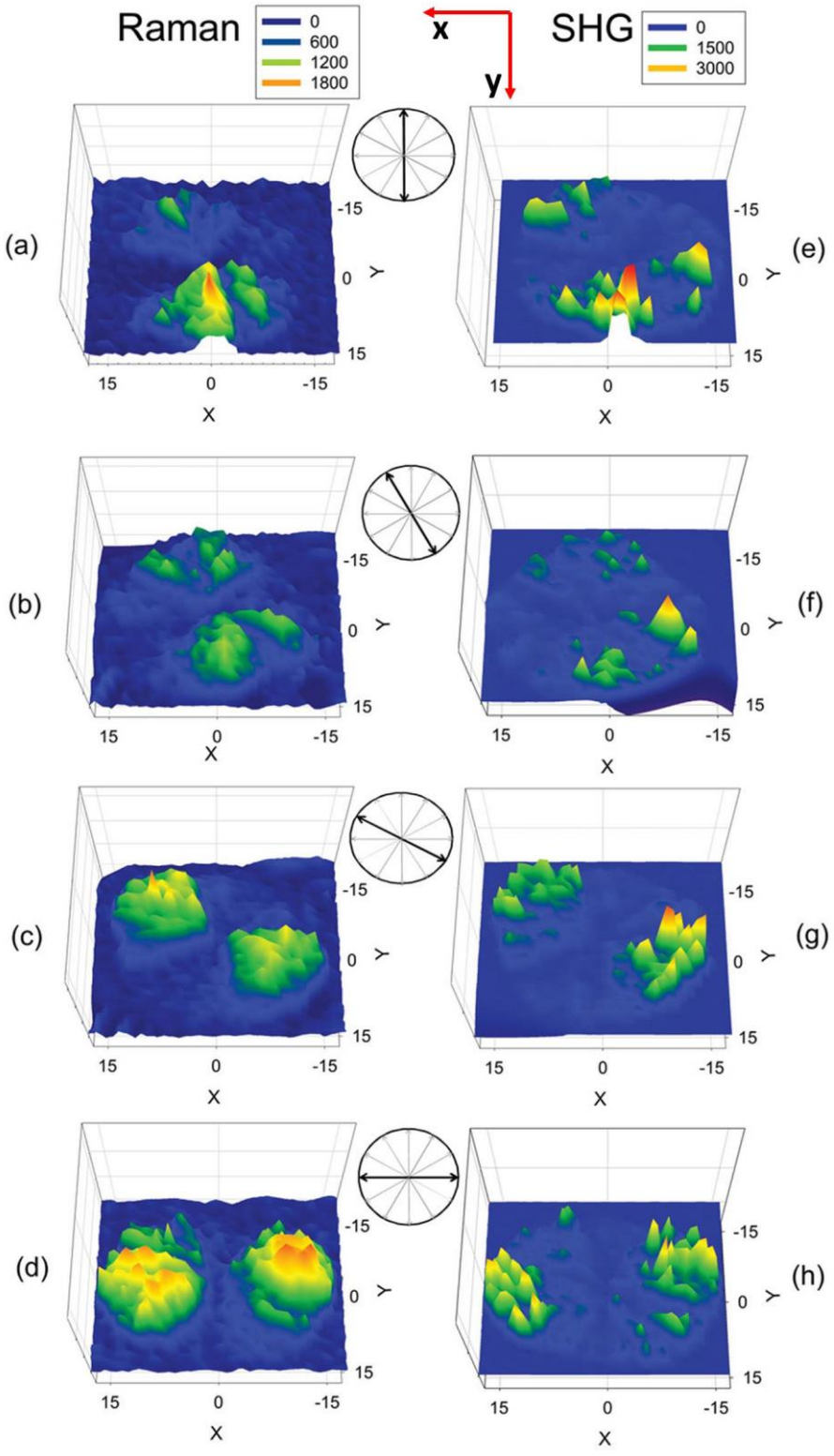

Figure 2.6: Probing the spherulite in Figure 2.5: micro-Raman (obtained at selected 250 cm^{-1} band, detection polarized y;y,y) and micro-SHG mapping for different angles of polarization of excitation and reflected signals [1, 2]

Macroscopic SHG Ψ response (Ψ_s-Exp.) obtained in transmission mode (see section 2.2.5) are depicted in **Figure 2.7**. Considering it is the sum of spherulites' SHG responses in non-active glass, one can use information obtained from macro SHG data and $LiNbO_3$ crystallite properties as inputs to equation (2.3). Experimentally, we observe from θ scans (see section 2.2.5) that $\theta_{pp} = \alpha\theta_{ps}$ → $I_{yy}^{2\omega} = \alpha I_{yx}^{2\omega}$ and $\theta_{ss} = \alpha\theta_{sp}$ → $I_{xx}^{2\omega} = \alpha I_{xy}^{2\omega}$ [1, 3] (2.5).

If we do not take into account the scattering loss, Equation 2.5 implies that $\left|\chi_{y;y,y}^{(2)}\right| = \sqrt{\alpha}\left|\chi_{y;x,x}^{(2)}\right|$ and $\left|\chi_{x;x,x}^{(2)}\right| = \sqrt{\alpha}\left|\chi_{x;y,y}^{(2)}\right|$ with estimation $\alpha \approx 2.35$.

Secondly, we observe from Ψ scans (see Section 2.2.5): $I_{\Psi\parallel}^{2\omega} = I_{\Psi\perp}^{2\omega}$ modulo 90°, which implies by identification $\sqrt{\alpha}\left|\chi_{y;x,x}^{(2)}\right| = \sqrt{\alpha}\left|\chi_{x;y,y}^{(2)}\right| = \left|\chi_{x;x,x}^{(2)}\right| = \left|\chi_{y;y,y}^{(2)}\right|$.

Furthermore, according to the $LiNbO_3$ $\chi^{(2)}$ components, we have $d_{15} = d_{31}$. This implies that $\chi_{y;y,x}^{(2)} = \chi_{x;y,y}^{(2)}$ and $\chi_{x;y,x}^{(2)} = \chi_{y;x,x}^{(2)}$

As a consequence, using equation (2.3), we obtain finally:

$$I_{\Psi y}^{2\omega} \propto \left|P_y^{2\omega}(\Psi)\right|^2 = ((E_o^{\omega})^4/8)\left(\chi_{y;y,y}^{(2)}\right)^2 \left|{}^1\!/_{\alpha}\cos^4(\Psi) + \sin^4(\Psi) + 2\left({}^2\!/_{\alpha} - {}^1\!/_{\sqrt{\alpha}}\right)\sin^2(\Psi)\cos^2(\Psi)\right| \quad (2.6)$$

$$I_{\Psi x}^{2\omega} \propto |P_x^{2\omega}(\Psi)|^2 = ((E_o^{\omega})^4/8)\left(\chi_{x;x,x}^{(2)}\right)^2 \left|\cos^4(\Psi) + {}^1\!/_{\alpha}\sin^4(\Psi) + 2\left({}^2\!/_{\alpha} - {}^1\!/_{\sqrt{\alpha}}\right)\sin^2(\Psi)\cos^2(\Psi)\right| \quad (2.7)$$

Then taking into account the estimation of α, one can estimate the identical responses modulo 90°:

$$I_{\Psi y}^{2\omega} \propto \left|P_y^{2\omega}\right|^2 \cong \left[{}^{(E_o^{\omega})^4}\!/_8\right]\left(\chi^{(2)}\right)^2 |0.425\cos^4\Psi + 0.397\cos^2\Psi\sin^2\Psi + \sin^4\Psi| \quad (2.8)$$

$$I_{\Psi x}^{2\omega} \propto |P_x^{2\omega}|^2 \cong \left[{}^{(E_o^{\omega})^4}\!/_8\right]\left(\chi^{(2)}\right)^2 |\cos^4\Psi + 0.397\cos^2\Psi\sin^2\Psi + 0.425\sin^4\Psi| \quad (2.9)$$

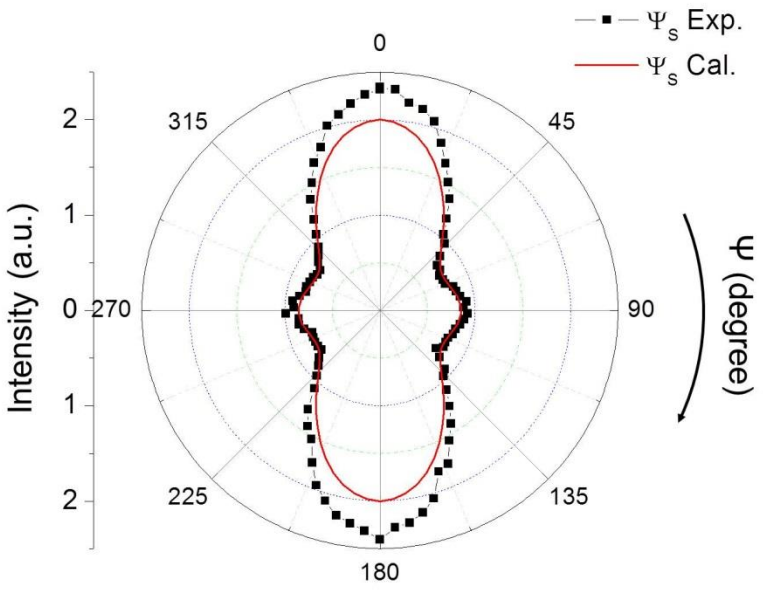

Figure 2.7: Nonlinear optical measurement performed on the bulk of LNS glass-ceramic Ψ-scan (Ψ_s). The experiment response was obtained by rotating the polarization of the laser beam along the z-axis (Figure 2.1). The detector was polarized along x-axis (or s). The calculation is based on equation 2.9

However, as illustrated on Figure 2.7, the calculation does not fit with the experimental patterns. The difference between them could be assigned to the assumption of scattering loss which could not be ruled out. Scattering loss is defined as SHG signal which is independent of the incident and analysed polarization. It are commonly observed for powder analysis [17]. In fact, this mismatch is supported by the dipolar nature of $LiNbO_3$ which contains d_{33} >> d_{31} and d_{22}.

Now, we take into account the scattering loss and recall the equation 2.6 and 2.7 with some modifications

$$I_{\Psi y}^{2\omega} \propto \left|P_y^{2\omega}(\Psi)\right|^2 = ((E_o^{\omega})^4/8)\left(\chi_{y;y,y}^{(2)}\right)^2 \left|{}^1\!/_{\alpha_1}\, cos^4(\Psi) + sin^4(\Psi) + 2\left({}^2\!/_{\alpha_1} - {}^1\!/_{\sqrt{\alpha_1}}\right)\sin^2(\Psi)\cos^2(\Psi)\right| + \langle B_{SL}\rangle \quad (2.10)$$

$$I_{\Psi x}^{2\omega} \propto |P_x^{2\omega}(\Psi)|^2 = ((E_o^{\omega})^4/8)\left(\chi_{x;x,x}^{(2)}\right)^2 \left|cos^4(\Psi) + {}^1/_{\alpha_1}\, sin^4(\Psi) + 2\left({}^2/_{\alpha_1} - {}^1/_{\sqrt{\alpha_1}}\right) sin^2(\Psi)\, cos^2(\Psi)\right| + \langle B_{SL}\rangle \quad (2.11)$$

Where α_1 is the ratio of $\left|\chi_{y;y,y}^{(2)}\right|^2 / \left|\chi_{y;x,x}^{(2)}\right|^2$ and $\langle B_{SL}\rangle$ is the scattering loss. Using the fitting function provided by Origin, we obtain $\alpha_1 \cong 5$ and $\langle B_{SL}\rangle \cong 0.23$ or:

$$I_{\Psi x}^{2\omega} \propto cos^4(\Psi) + 0.2sin^4(\Psi) + 0.094\, sin^2(\Psi)\, cos^2(\Psi) + 0.23 \quad (2.12)$$

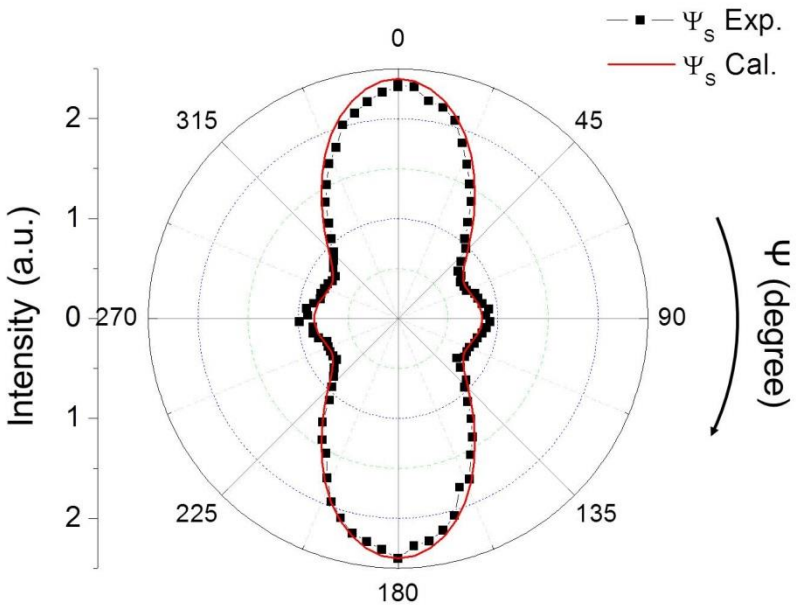

Figure 2.8: The experiment response (Ψs) in comparison with the calculated patterns which is based on equation 2.12

As observed on **Figure 2.8**, the calculated curve extracted from Equation 2.12 fit well with the experimental result of Ψ_y. The scattering loss is around 23%. This result is in good agreement with a resulting macroscopic SHG signal being the sum of SHG-active domains producing dominant dipolar component (d_{33}). However, the ratio α is effected by the orientation distribution of dipoles within the spherulites, so it should be lower than the proportion of d_{33} and other components.

2.3.4 $La_2O_3 – B_2O_3 – GeO_2$ (LBG) glass ceramics

The transparent glass ceramic sample is elaborated from the ($25La_2O_3 – 25B_2O_3 – 50GeO_2$) glass composition obtained by typical quenching method. Then the glass ceramic samples were prepared by 2-step heat treatment in which the first nucleation step was done at 680°C during 2h and followed by a crystal growth step at 775°C (between T_g and T_x) during 30min. Further conditions of elaboration of LBG glass and glass ceramics can be found elsewhere [2, 18]. The spherulites within the LBG glass network in around 30µm size have been obtained and characterized by XRD method. The only $LaBGeO_5$ crystal phase has been proved to precipitate from this thermal process. The glass ceramics shows high transmission close to 80%. Some other properties such as thermal, structural and optical properties of the glass ceramics can be found in [2].

In order to investigate the microscopic nonlinear SHG optical response and make the appropriate correlation with the glass ceramics structuring, the combination of (i) micro-Raman backscattering spectroscopy and (ii) micro-SHG in the backscattering mode were utilized simutaneously. The detail for the technique can be found in the section 2.2.6 of this chapter. Those techniques employ the same setup to get a direct link between optical properties and local structure at the microscopic level. Micro SHG/Raman correlative analysis was performed around 100 µm inside the bulk of a LBG glass ceramic at the equatorial plane of a spherulite. **Figure 2.9** shows three typical Raman spectra measured either inside or outside the spherulite structure (location noted on the optical image). Raman measurements were carried out in y-y configuration with the vertical polarization oriented along the y-axis of the lab-framework (Figure 2.9(a)).

Raman spectra measured within the glass matrix (area 1, Figure 2.9(b)) show three main large bands within the spectral ranges of 250–400, 450–650, and 700–900 cm^{-1}. The low frequency envelope is attributed to lanthanum vibrations and lattice modes from the glass matrix. The two other large massifs peaking at 800 and 550 cm^{-1} correspond, respectively, to symmetric stretching vibration of BO_4 and GeO_4 tetrahedra units and bending modes from the bridges forming

tetrahedral chains [19-22]. Inside the spherulite (Figures 2.9(c) and (d)), Raman sharp peaks appear in addition to the glass matrix background. A good correspondence can be done with the Raman signature of the stillwellite $LaBGeO_5$ crystalline phase [19, 20]. Raman spectra intensities of a peak at 390 cm^{-1} differ when measured at different places in the spherulite. According to Raman studies on single crystals [19, 20], the intensity of this low frequency peak is dependent of the crystal orientation and is maximum when the incident laser direction of polarization is parallel to the c axis of the LBG crystal. The Raman (yy) mapping presented in **Figure 2.10**(b) depicts the integration of the band peaking at 390 cm^{-1}. A stronger Raman signal is observed along the spherulite vertical axis, revealing a radial distribution of $LaBGeO_5$ crystallites with their c-axis oriented along the spherulite radius.

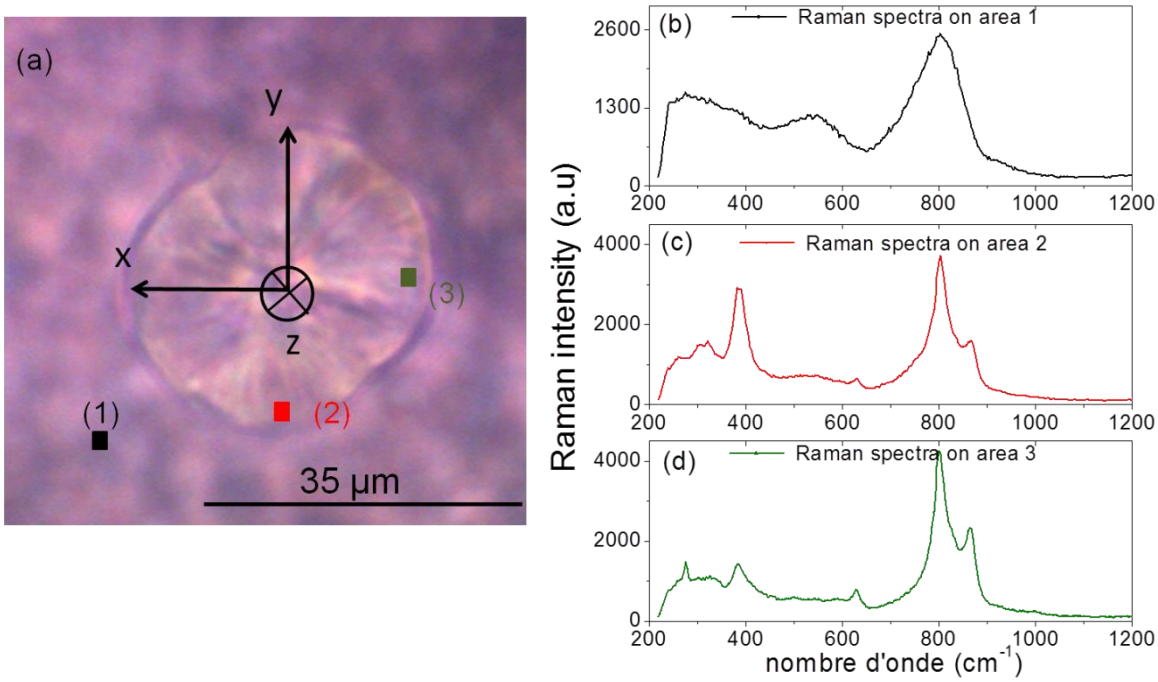

Figure 2.9: (a) Optical microscope image of a spherulite and three distinct spots where Raman spectra were recorded. Parts (b), (c) and (d) of the figure show the corresponding Raman spectra

The micro-SHG mapping carried out at the same position in (y;y,y) polarization configuration is reported in Figure 2.10(a). One can notice large variations of the

SHG intensity within a range of three orders of magnitude. Locations of maximum SHG signal are mainly distributed along the horizontal axis of the figure. In Figure 2.10(c), we have combined the two Raman and SHG images in order to point out the accurate orthogonality existing between the c-axis orientation of the crystallites revealed by Raman and their maximum SHG response.

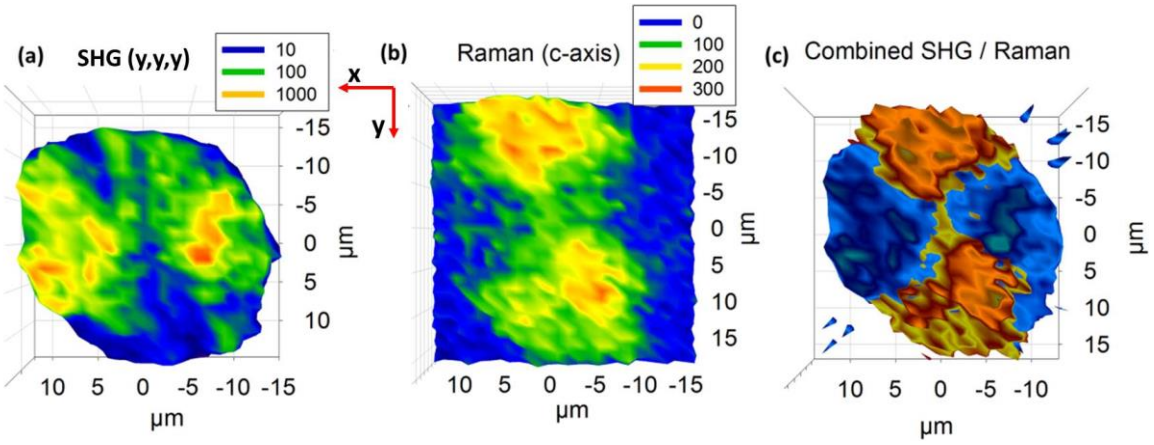

Figure 2.10: (a) micro-SHG mapping of a spherulite probed with the excitation and the collected harmonic polarized vertically (a similar image is obtained in crossed polarization (x;y,y)), (b) Raman mapping indicating the radial orientation of the c-axis of LBG crystallites, (c) combination of the SHG and Raman images each signal is depicted with two different color code (blue for SHG and brown for Raman).

To interpret these observations, we will refer to the NLO properties reported for a $LaBGeO_5$ single crystal. $LaBGeO_5$ class symmetry is C_3 and three nonlinear coefficients with similar magnitude have been reported: d_{11} = 0.76 pm/V, d_{33} = 0.57 pm/V, and d_{31} = 0.68 pm/V [23]. If we consider that the *a* and *b* axes of the crystal could not be differentiated because the crystal structure is uniaxial, we assume d_{11} = d_{22} and the single crystal tensor deriving from the C_3 class symmetry. The nonlinear tensor is expressed as follow:

$$C_3 : \begin{pmatrix} d_{11} & \overline{d_{11}} & 0 & 0 & d_{31} & \overline{d_{11}} \\ \overline{d_{11}} & d_{11} & 0 & d_{31} & 0 & \overline{d_{11}} \\ d_{31} & d_{31} & d_{33} & 0 & 0 & 0 \end{pmatrix} \quad (2.13)$$

Micro-Raman analysis has shown a radial distribution of the $LaBGeO_5$ crystallites along their c-axis within the spherulites. Then, in micro-SHG, we will probe the

terms d_{33} or d_{11} in (y;y,y) configuration if the c-axis is along y and d_{31} for (x;y,y) configuration when the c-axis is along the x. Finally, as a strict orthogonality is observed between c-axis orientation of the crystallites and their SHG response and the same SHG response observed for (y;y,y) and (x;y,y) polarization configurations, we can deduce that $d_{11} >> d_{33}$. Comparable images are obtained for both configurations in accordance with two remaining d_{11} and d_{31} coefficients of comparable value. One hypothesis to explain the low value of d_{33} could be due to an anti-parallel ordering of the crystallites (like anti-ferroelectric domains) within the spherulite inducing a cancellation of the main dipolar component d_{33}.

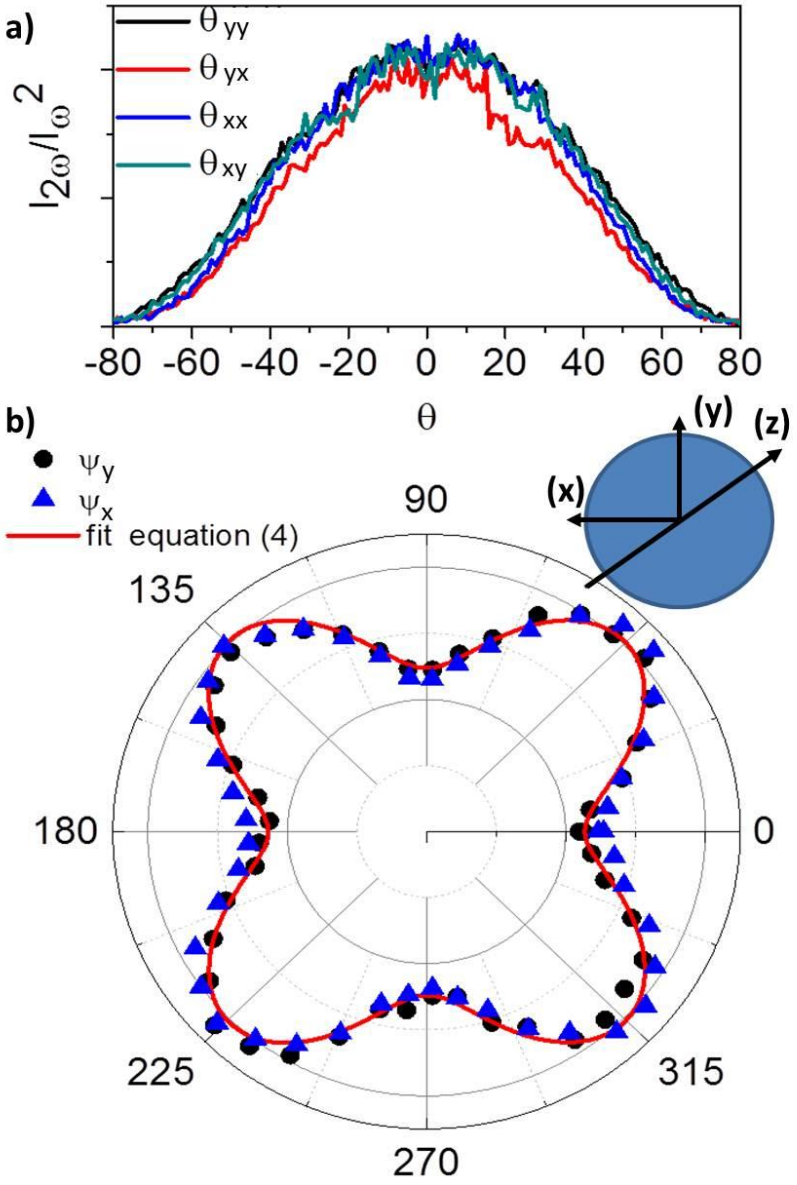

Figure 2.11: nonlinear optical measurement performed on the bulk of LBG1 glass-ceramic θ-scan (top) and Ψ-scan (bottom).

From the formula (2.3) given in section 2.3.2, we can obtain:

$$I_{\Psi i}^{2\omega} \propto \left|P_i^{2\omega}(\Psi)\right|^2 = (E_o^{\omega})^4/8 \left| \left(\chi_{i;x,x}^{(2)}\right)^2 cos^4(\Psi) + \left(\chi_{i;y,y}^{(2)}\right)^2 sin^4(\Psi) + 2\left(2\left(\chi_{i;x,y}^{(2)}\right)^2 - \chi_{i;x,x}^{(2)}.\chi_{i;y,y}^{(2)}\right)\sin^2(\Psi)\cos^2(\Psi)\right| \quad (2.14)$$

Experimentally, we observe from θ scans $I_{yi}^{2\omega} = I_{xi}^{2\omega}$, which implies $\left|\chi_{y;x,x}^{(2)}\right| = \left|\chi_{y;y,y}^{(2)}\right|$ and $\left|\chi_{x;x,x}^{(2)}\right| = \left|\chi_{x;y,y}^{(2)}\right|$ (**Figure 2.11a** or [2]).

Then from Ψ scans $I_{\Psi y}^{2\omega} = I_{\Psi x}^{2\omega}$ which implies by identification $\left|\chi_{y;x,x}^{(2)}\right| = \left|\chi_{x;y,y}^{(2)}\right|$ and $\left|\chi_{x;x,x}^{(2)}\right| = \left|\chi_{y;y,y}^{(2)}\right|$. In other words all the components are equal in module.

Furthermore, if we come back to the crystal nonlinear tensor and then consider the radial orientation of the crystallites inside the spherulite, we have $d_{15} = d_{31}$ for each crystal. This implies that $\left|\chi_{y;y,x}^{(2)}\right| = \left|\chi_{x;y,y}^{(2)}\right| = \left|\chi_{x;y,x}^{(2)}\right| = \left|\chi_{y;x,x}^{(2)}\right|$.

However, since we observe experimental maxima at 45° modulo 90° it is necessary that $\chi_{i;x,x}^{(2)} = -\chi_{i;y,y}^{(2)}$ to verify this condition in the following expression.

$$I_{\Psi i}^{2\omega} \propto \left|P_i^{2\omega}\right|^2 = \left[{(E_o^{\omega})^4}/{8}\right]\left(\chi^{(2)}\right)^2 |cos^4\Psi + 6\,cos^2\Psi\, sin^2\Psi + sin^4\Psi| \quad (2.15)$$

In this particular case, a general expression of SHG intensity in ψ–scan measurement can be noticed as follow [4]:

$$\langle I_{\psi i}^{2\omega}\rangle = G\left[\left[\left|\chi^{(2)}\right|^2 C_{\Psi i}^{Coh}\right]_{Sph} + \langle B_{SL}\rangle\right].[I^{\omega}]^2 \quad (2.16)$$

With $i = x, y$ orientations (Figure 2.1), G is a pre-factor, $\chi^{(2)}$ is a Cartesian component of the average efficient susceptibility and $\langle B_{SL}\rangle$ accounts for scattering losses, $C_{\Psi i}^{Coh}$ is the average coherent response of a spherulite.

In short, the average coherent response of a $LaBGeO_5$ spherulite can be given by

$$C_{\Psi i}^{Coh} = [cos^4\Psi + 6\,cos^2\Psi\,sin^2\Psi + sin^4\Psi] \quad (2.17)$$

As reported in Figure 2.11b, a very good agreement between the data and Eq. (2.15) is observed, yielding scattering losses $\langle B_{SL} \rangle \sim 17\%$. Therefore, SHG studies performed at different spatial scales are fully in agreement with the picture of a radial distribution of crystals inside the spherulite but with an octupolar response indicating thus that a local loss of the dipolar response occurs, which may be explained by an anti-ferroelectric arrangement of the crystallites.

2.3.5 Conclusion

In conclusion, the general mathematical model for the correlation between local structure of a spherulite and the macroscopic SHG patterns has been proposed and developed. Based on the model, the origin of the dipolar SHG response (LNS glass ceramics) and the octupolar SHG response (LBG glass ceramics) observed for $LiNbO_3$ and $LaBGeO_5$ crystallites precipitating in silicate or borogermanate glasses have been correlated to the organization of the crystallites within spherulite domains. The c-axis crystallites are radially distributed along the radius directions of the spherulites.

In terms of LNS glass ceramics, the general equation describing the macro SHG patterns depends on the polarization of the detector. However, they are identical but rotated 90^o.

In the specific case of the LBG glass ceramics, an antiparallel orientation of crystallites domains is expected to explain the loss of the dipolar d_{33} component in the SHG response.

The model shows good agreement with experimental results in both LNS and LBG glass ceramics containing radially oriented crystallites within the spherulite. However, the different behaviors (dipolar and octupolar) of SHG patterns is due to the different crystal symmetries and organization of crystallites. Therefore, this resulted model will be useful to be applied to the next glass ceramic system based

on germanotellurite composition with respect to its local crystal organization and symmetry.

REFERENCES

1. Vigouroux, H., E. Fargin, S. Gomez, B. Le Garrec, G. Mountrichas, E. Kamitsos, F. Adamietz, M. Dussauze, and V. Rodriguez, *Synthesis and Multiscale Evaluation of LiNbO3-Containing Silicate Glass-Ceramics with Efficient Isotropic SHG Response.* Advanced Functional Materials, 2012. **22**(19): p. 3985-3993.
2. Vigouroux, H., *Etude de vitrocéramiques optiques pour le doublement de fréquence*. 2012, Université Sciences et Technologies-Bordeaux I.
3. Vigouroux, H., E. Fargin, A. Fargues, B.L. Garrec, M. Dussauze, V. Rodriguez, F. Adamietz, G. Mountrichas, E. Kamitsos, and S. Lotarev, *Crystallization and second harmonic generation of lithium niobium silicate glass ceramics.* Journal of the American Ceramic Society, 2011. **94**(7): p. 2080-2086.
4. Verbiest, T., K. Clays, and V. Rodriguez, *Second-order nonlinear optical characterization techniques: an introduction*. 2009: CRC Press.
5. Vigouroux, H., E. Fargin, S. Gomez, B. Le Garrec, G. Mountrichas, E. Kamitsos, F. Adamietz, M. Dussauze, and V. Rodriguez, *Synthesis and multiscale evaluation of LiNbO 3 - Containing silicate glass-ceramics with efficient isotropic SHG response.* Advanced Functional Materials, 2012. **22**(19): p. 3985-3993.
6. Crémoux, T., *Physico-chimie aux interfaces de systèmes vitreux à charge d'espace*. 2013, Université Sciences et Technologies-Bordeaux I.
7. Komatsu, T. and T. Honma, *Optical Active Nano-Glass-Ceramics.* International Journal of Applied Glass Science, 2013. **4**(2): p. 125-135.
8. Jain, H., *Transparent ferroelectric glass-ceramics.* Ferroelectrics, 2004. **306**(1): p. 111-127.
9. Tarafder, A. and B. Karmakar, *Nanostructured LiTaO3 and KNbO3 Ferroelectric Transparent Glass-Ceramics for Applications in Optoelectronics*. 2011: InTech.
10. Maciel, G., N. Rakov, C.B. de Araujo, A. Lipovskii, and D. Tagantsev, *Optical limiting behavior of a glass-ceramic containing sodium niobate crystallites.* Applied Physics Letters, 2001. **79**(5): p. 584-586.
11. Bisault, J., G. Ryschenkow, and G. Faivre, *Spherulitic branching in the crystallization of liquid selenium.* Journal of crystal growth, 1991. **110**(4): p. 889-909.
12. Hutter, J.L. and J. Bechhoefer, *Banded spherulitic growth in a liquid crystal.* Journal of crystal growth, 2000. **217**(3): p. 332-343.
13. Hurle, D.T., *Handbook of crystal growth*. Vol. 1. 1993: North Holland.
14. Gránásy, L., T. Pusztai, G. Tegze, J.A. Warren, and J.F. Douglas, *Growth and form of spherulites.* Physical Review E, 2005. **72**(1): p. 011605.
15. Smith, S., H. Riccius, and R. Edwin, *Refractive Index of Lithium Niobate (errata).* Optics Communications (Netherlands), 1977. **20**: p. 188.
16. Takahashi, Y., K. Kitamura, Y. Benino, T. Fujiwara, and T. Komatsu, *LaBGeO 5 single crystals in glass and second-harmonic generation.* Materials Science and Engineering: B, 2005. **120**(1): p. 155-160.
17. Kurtz, S. and T. Perry, *A powder technique for the evaluation of nonlinear optical materials.* Journal of Applied Physics, 1968. **39**(8): p. 3798-3813.
18. Truong, L.N., M. Dussauze, E. Fargin, L. Santos, H. Vigouroux, A. Fargues, F. Adamietz, and V. Rodriguez, *Isotropic octupolar second harmonic generation response in LaBGeO5 glass-ceramic with spherulitic precipitation.* Applied Physics Letters, 2015. **106**(16): p. 161901.

19. Hrubá, I., S. Kamba, J. Petzelt, I. Gregora, Z. Zikmund, D. Ivannikov, G. Komandin, A. Volkov, and B. Strukov, *Optical phonons and ferroelectric phase transition in the LaBGeO 5 crystal.* Physica Status Solidi B Basic Research, 1999. **214**: p. 423-440.
20. Gupta, P., H. Jain, D.B. Williams, T. Honma, Y. Benino, and T. Komatsu, *Creation of Ferroelectric, Single-Crystal Architecture in Sm0. 5La0. 5BGeO5 Glass.* Journal of the American Ceramic Society, 2008. **91**(1): p. 110-114.
21. Stone, A., M. Sakakura, Y. Shimotsuma, G. Stone, P. Gupta, K. Miura, K. Hirao, V. Dierolf, and H. Jain, *Directionally controlled 3D ferroelectric single crystal growth in LaBGeO 5 glass by femtosecond laser irradiation.* Optics express, 2009. **17**(25): p. 23284-23289.
22. Takahashi, Y., A. Iwasaki, Y. Benino, T. Fujiwara, and T. Komatsu, *Ferroelectric properties and second harmonic intensities of stillwellite-type (La, Ln) BGeO5 crystallized glasses.* Japanese journal of applied physics, 2002. **41**(6R): p. 3771.
23. Kaminskii, A., A. Butashin, I. Maslyanizin, B. Mill, V. Mironov, S. Rozov, S. Sarkisov, and V. Shigorin, *Pure and Nd3+-, Pr3+-Ion Doped Trigonal Acentric LaBGeO5 Single Crystals Nonlinear Optical Properties, Raman Scattering, Spectroscopy, Crystal-Field Analysis, and Simulated Emission of Their Activators.* physica status solidi (a), 1991. **125**(2): p. 671-696.

CHAPTER 3 – Ag_2O DOPED GERMANOTELLURITE GLASS AND GLASS CERAMICS

Contents

CHAPTER 3 – Ag_2O DOPED GERMANOTELLURITE GLASS AND GLASS CERAMICS

3.1 Introduction

For the last two decades, optical nonlinearity, especially Second-Order Nonlinearity (SON), has become a key property for many applications in the domain of photonics, notably for electro-optical effects and frequency conversion. Single crystals are well known materials for these applications because of their strong optical nonlinear property. However, they are complicated to manufacture and are strongly dependant on crystal orientation. One way to circumvent this problem is to replace the single crystals with new materials like glass ceramics which can present a favourable combination of ferroelectric crystals and glass matrix where SON does not exist due to centrosymmetric organization [1, 2]. Several glass ceramic materials presenting second harmonic generation (SHG) arising from $LaBGeO_5$, $LiNbO_3$ and $KNbO_3$ crystals have been reported [3-5] but their low transparency still limits commercial applications.

Optical glass ceramics require high transparency and high SON [2, 6]. To ensure the quality of the transmission in glass ceramics, two common solutions are envisaged: size restriction of crystals and/or reduction of the refractive index difference between the glass and the crystallized parts [7]. The latter requirement

can be fulfilled by a careful choice of glass matrix and crystal phase. Regarding the host-glass compositions, tellurite remains one of the most promising glass formers, because of its low melting temperature and the fact that refractive indices of those glasses and many ferroelectric crystals are quite similar [8]. This means that low scattering losses at the interface between glass and crystals can be obtained and therefore high transparency might be achieved. Another possibility is to control the time and temperature of annealing to obtain small crystals, of sub-micron size, and thus reduce the scattering of light [2]. However, in order to control the crystal growth in the bulk, it is necessary to avoid dominant surface crystallization and promote bulk crystallization [9, 10]. Only a few reported works show elaboration and optical properties characterizations of transparent tellurite glass–ceramics containing a high crystal volume fraction [2, 11]. This can be attributed to preferential surface crystallization in TeO_2 -based glasses [2, 10].

Monteiro et al. has studied the TeO_2 – GeO_2 – Nb_2O_5 – K_2O germanotellurite system [12, 13] where the combination of the TeO_2 and GeO_2 glass-forming constituents results in highly stable glasses, especially for the high germanate and high tellurite compositions [12]. The germanotellurite composition $70TeO_2$ – $10GeO_2$ – $10Nb_2O_5$ – $10K_2O$, with a higher refractive index [12], was chosen for further studies. In this work, we added different amounts of silver oxide as nucleating agent, aiming to control the bulk vs surface crystallization processes in order to obtain homogeneous glass ceramics. Optical transparency and second order optical properties are correlated to glass ceramics synthesis.

3.2 Effect of silver oxide addition on the germanotellurite glasses

3.2.1 Glass preparation

Germanotellurite glasses with compositions (100-x) [$70TeO_2$ – $10GeO_2$ – $10Nb_2O_5$ – $10K_2O$] – xAg_2O (mol%) for x=0, 2, 4, 6 mol% (labeled 7T1G, 7T1G2Ag, 7T1G4Ag, and 7T1G6Ag, respectively) were prepared by traditional melt-quenching methods. A mixture of commercial powders of TeO_2 (99.99%, Alfa Aesar), GeO_2 (>99.99%, Aldrich), Nb_2O_5 (99.9985%, Alfa Aesar), K_2CO_3

(99.997%, Alfa Aesar) and corresponding amount of silver nitrate ($AgNO_3$, 99.995%, Alfa Aesar) was melted at 900ºC for 30 minutes after a preheating step at 150ºC to remove moisture. It was then poured on a 300ºC pre-heated platinum plate before an annealing step at the same temperature (300ºC, ~ T_g – 50ºC [13]), for 6 hours.

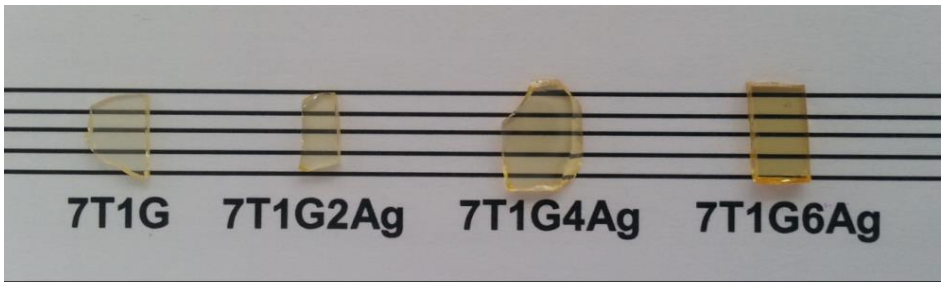

Figure 3.1: Elaborated (100-x) [$70TeO_2$ – $10GeO_2$ – $10Nb_2O_5$ – $10K_2O$] – xAg_2O (mol%) glass samples.

3.2.2 Elemental analysis, density and refractive index

Nominal and experimental compositions determined by WDS analysis of all glass samples are presented in **Table 3.1**. The experimental results are quite close to nominal composition. Some differences occur, namely with light elements such as Ge and O which could not be detected precisely. Ag element, on the other hand, usually shows slightly lower quantity than theoretical one due to volatility of Ag_2O during high temperature melting (900ºC).

The refractive index of each glass is higher than 2.00 as listed in **Table 3.2**. Due to the increase of Ag content (from 0 to 6%), the refractive index increases slightly from 2.021 to 2.043 (at 532nm).

Due to the high density of Ag_2O (molar mass of 231.77g/mol [14]), the density of 7T1GxAg (x=0,2,4,6) shows a monotonic increase with increasingAg_2O content from 4.858g/cm^3 to 5.063g/cm^3 (see Table 3.2).

Table 3.1: WDS analysis (in at%) of 7T1GxAg glass compositions (x=0,2, and 6) in comparison with the starting calculated composition.

	7T1G (at%)		7T1G2Ag (at%)		7T1G6Ag (at%)	
	Cal.	Exp.	Cal.	Exp.	Cal.	Exp.
Te	20.59	20.96	20.22	20.82	19.50	19.26
K	5.88	6.47	5.78	6.16	5.57	6.65
Ge	2.94	2.78	2.89	2.70	2.79	3.74
O	64.71	64.34	64.15	63.94	63.01	60.63
Nb	5.88	5.44	5.78	5.31	5.57	6.44
Ag	0	0	1.18	1.07	3.56	3.26

3.2.3 Thermal analysis

Characteristic temperatures (T_g, T_{x1} and T_{x2}) of all glasses are listed in Table 3.2 and DSC curves of all glasses heated at 20K/min are shown in **Figure 3.2**. Glass transition temperature decreases from 377°C to 339°C with the progressive insertion of silver oxide. Besides that, a second crystallization peak occurs, with increasing silver oxide addition which becomes well separated for the 7T1G6Ag composition. In order to study crystallization of these glasses, bulk and powder DSC measurements were performed. The bulk measurements were made in small pieces of glass with ~1-2 mm, while powder measurements were made in grinded samples with ~80-100 um in size. Figure 3.2 shows different crystallization behavior in bulk and powder silver doped glasses, in comparison with the 7T1G

glass. In the silver-free composition, surface crystallization occurs at lower temperature than bulk crystallization (T_x comparisons, Table 3.2). Then, the gap between T_{x1} and T_{x2} rises when the silver oxide content increases. For the 7T1G6Ag composition, the first onset crystallization temperature T_{x1} is clearly observed around 420ºC in both bulk and powder samples. For this composition, both bulk and powder forms show comparable thermal behavior.

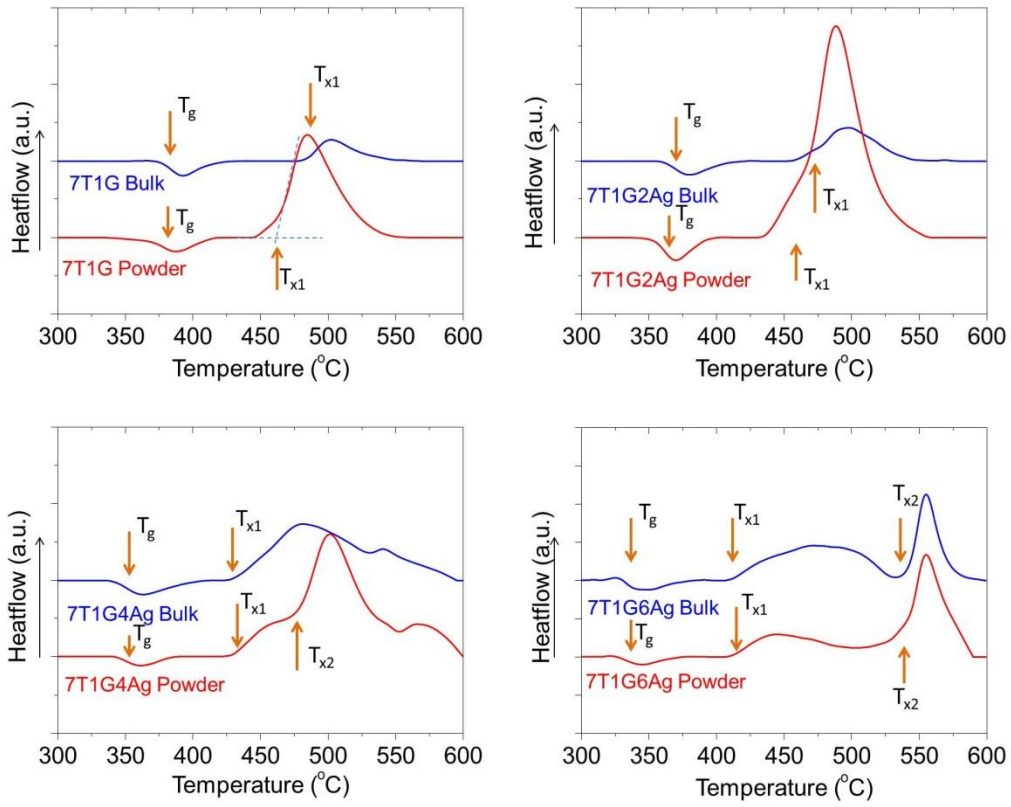

Figure 3.2: DSC curves of 7T1GxAg (x=0, 2, 4 and 6) glasses. Red and blue curves correspond to powder and bulk scans, respectively.

Table 3.2: Thermal characteristics of silver oxide doped germanotellurite glasses

Sample	T_g (°C)	T_{x1} (°C) (±2)		T_{x2} (°C) (±2)		n (at 532nm)	ρ (g/cm^3)	Thickness (mm)
	(±2)	Powder	Bulk	Powder	Bulk	(±0.005)	(±0.005)	(±0.005)
7T1G	377	459	478	-	-	2.021	4.858	0.903
7T1G2Ag	360	436	455	-	-	2.039	4.896	0.991
7T1G4Ag	351	429	434	470	-	2.036	5.026	1.042
7T1G6Ag	339	417	420	540	541	2.043	5.063	0.924

3.2.4 Structural analysis

To illustrate the structural modification of glass samples in respect to silver oxide content, normalized (at 670 cm^{-1}) Raman spectra of all glass samples are presented in **Figure 3.3**. All spectra exhibit two broad intense features which are similar to previous studies of tellurite glasses [12, 15-17]. The region at 400-550 cm^{-1} is attributed to the bending vibrations of the Te-O-Te linkages. The high-frequency region, which consists of a broad peak at 650-670 cm^{-1} and two shoulders at 720-750 cm^{-1} and 850-900 cm^{-1}, is ascribed to the stretching mode of the TeO_4 trigonal bipyramid (tbp) and TeO_{3+1} or TeO_3 trigonal pyramid (tp), respectively, whereas the last one belongs to the stretching mode of Nb-O bonds [12, 18].

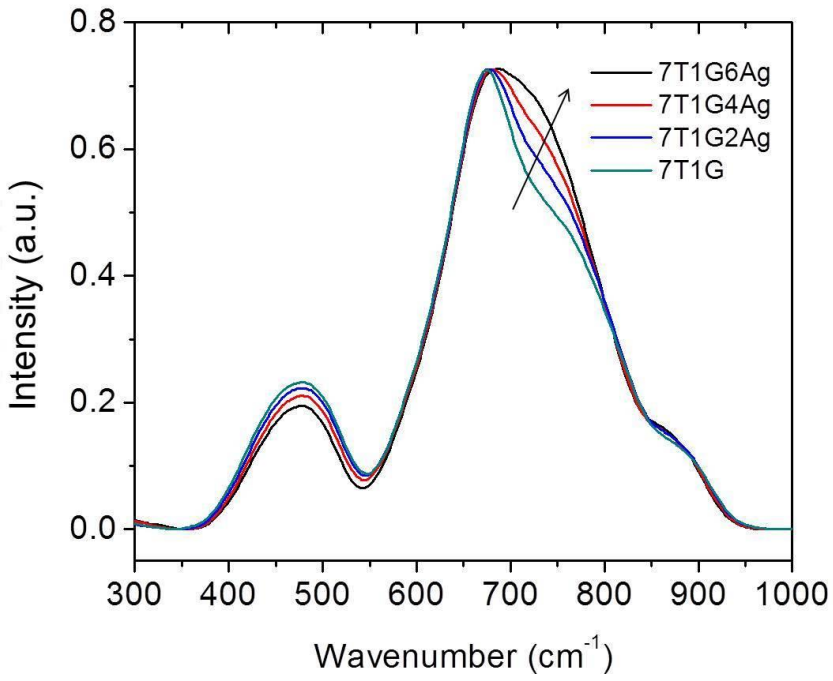

Figure 3.3: Normalized Raman spectra of germanotellurite glasses with different amount of silver oxide

Raman spectra of germanotellurite glasses with 10 mol% of GeO_2 mainly present specific features of the TeO_2-based glasses, in which the glass network is built of TeO_4 tbp and TeO_{3+1}/TeO_3 tp entities [19-21]. In such TeO_2 rich glasses, the

vibration bands attributed to GeO_x entities could be overlapped by strong TeO_x bands, though Ge-O-X (X=Ge, Te) bridging bond vibration cannot be excluded in the region 400-550 cm^{-1} as a maximum is observed at 420 cm^{-1} in the GeO_2 glass spectrum attributed to Ge-O-Ge symmetric stretching vibration [12]. By adding silver oxide, intensity decrease of the band attributed to Te-O-Te linkages (400-550 cm^{-1} region), and intensity increase of the shoulder (at 770 cm^{-1}) attributed to TeO_{3+1} or TeO_3 tp vibrations are observed. This indicates that the interaction of Ag ions with the network leads to the disruption of TeO_4 tbp units and its conversion to TeO_{3+1}/TeO_3 tp units. This effect is also consistent with previous studies [19, 22].

3.2.5 Optical properties

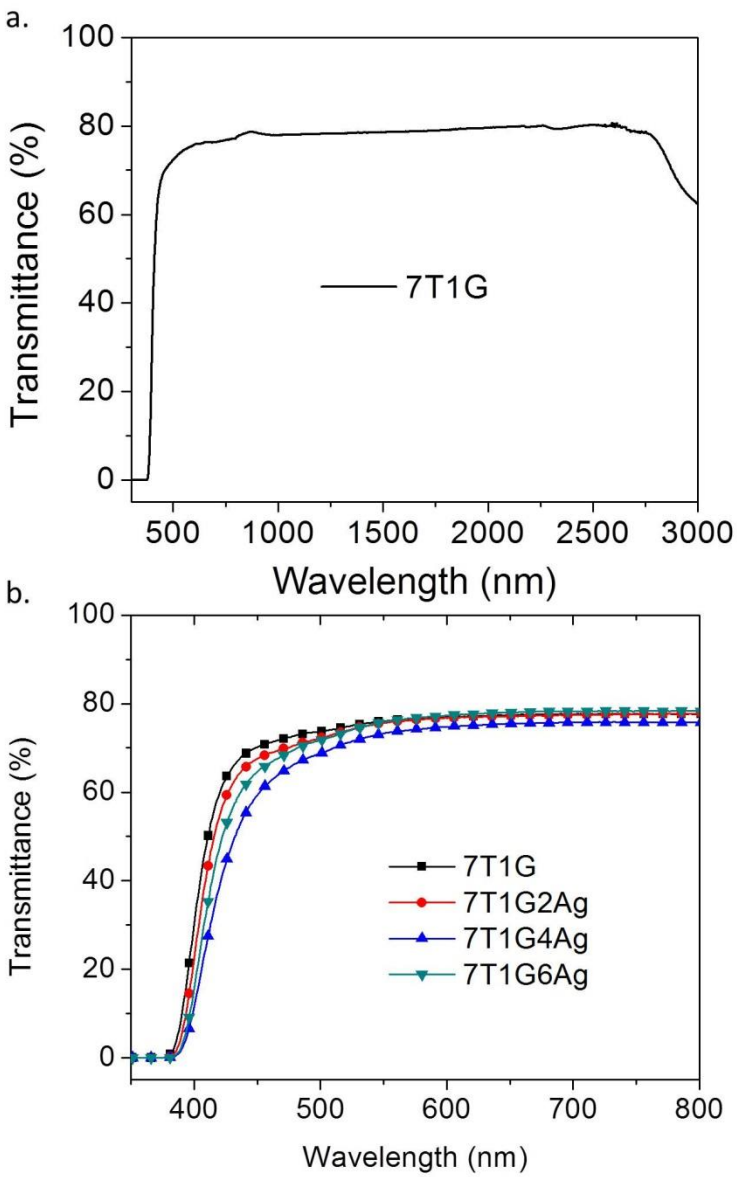

Figure 3.4: (a) Transparency window of the 7T1G glass from 400nm to 3μm and (b) Transmittance spectra of glass samples with compositions (100-x)[70TeO_2 – 10GeO_2 – 10K_2O – 10Nb_2O_5] – xAg_2O, where x = 0 – 6.

The transmittance spectra in the Ultra Violet – Visible – Near Infrared region are presented in **Figure 3.4** for all glass compositions. The UV edge is observed at around 400nm and they present a light yellowish color. Tellurite-based glasses have a long optical window up to 3 μm which is mentioned as an advantage [23,

24]. Kim et al. [8] measured the transmission window of pure TeO_2 glass in the range of wavelength between 200nm and 2.5 µm, the absorption being limited in the near-infrared region by the absorption of H_2O impurity. This could be improved if necessary by preliminar purification of reagents and fusion under controlled atmosphere. The transmission is stable close to 80% and then decreases beyond 2500 nm.

As other tellurite-based glasses, germanotellurite glasses also have high refractive index (n > 2.0, Table 3.2) which leads to high multireflection loss. The loss is estimated by Fresnel formula to more than 20% and is close to experimental results (absorption loss and Rayleigh diffusion loss were not taken into account). It is noticed that the reflectance losses occur at the interfaces between glass and air on both sides [25].The equation below shows that for the 7T1G6Ag composition, with n_{800}=2.04, the reflectance will be estimated as 21% (R=1-T).

$$T \approx \frac{2n}{n^2+1} \approx 0.79 \quad (3.1)$$

The cut-off wavelength [26] on the UV side shows a red-shift with respect to pristine glass as a sequence of silver oxide insertion. The increase of NBO atoms with the addition of Ag_2O as modifiers makes the glass structure become less ordered. As a result, it could induce more extension of the localized states within the gap according to Mott and Davies [27], leading to a decrease of the band gap. Furthermore, the formation of silver clusters observed previously in literature [28, 29] could also be at the origin of a band-gap reduction. This hypothesis will be further studied through luminescence studies.

3.2.6 Phase separation and crystalline phase

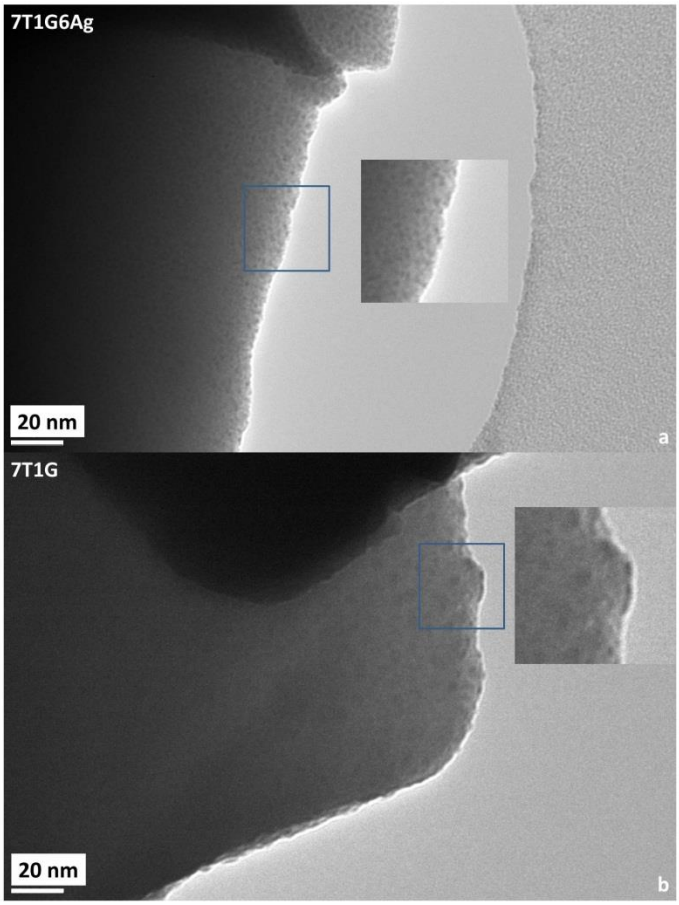

Figure 3.5: Transmission electron microscopy image of (a) 7T1G6Ag and (b) 7T1G glasses.

Transmission electron microscopy observations of the glass samples reveal the presence of circular-shape droplets on the scale of 2-5nm, indicating the existence of nanoscopic liquid-liquid phase separation in the melts of 7T1G6Ag and 7T1G compositions (**Figure 3.5a and 3.5b**). This phase separation was also observed for fast quenching in which the crucible with the melt was put directly in cold water.

To investigate the crystal phases precipitating in each kind of glass, heat treatment was performed. Specific heat treatment temperatures were chosen so that $T \geq T_{x1}$ for each composition. The glass is crushed, heated during 12h, and characterized by XRD diffraction. As observed in **Figure 3.6**, the main crystalline phase appearing among other phases, in 7T1G, is δ-TeO_2. With increasing Ag_2O content, this phase reduces in preponderance and other phases rise, such as the

crystalline phase $K[Nb_{1/3}Te_{2/3}]_2O_{4.8}$. In fact, for 6 mol% Ag_2O addition, the crystallization evidences only the $K[Nb_{1/3}Te_{2/3}]_2O_{4.8}$ phase if the temperature $T \cong T_{x1}$. For $T>T_{x1}$, different phases appear, one of which could be assigned to γ-TeO_2 [30, 31].

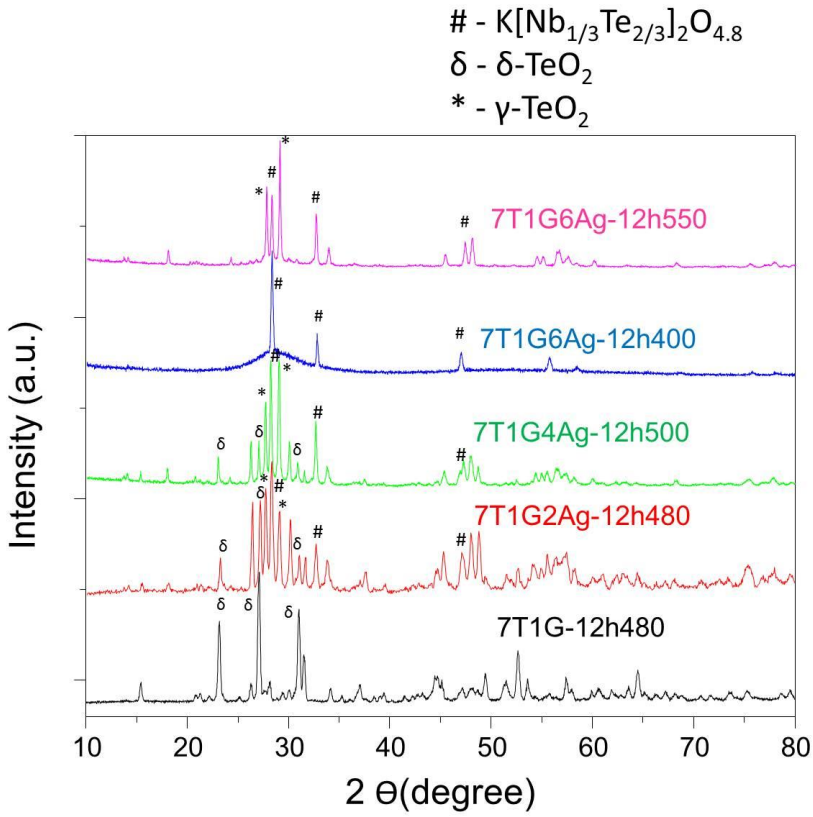

Figure 3.6: XRD patterns of heat treated7T1GxAg compositions. The heat treatment temperature was chosen, for each composition, to meet the condition ($T>T_{x1}$). In the figure, # is $K[Nb_{1/3}Te_{2/3}]_2O_{4.8}$, δ is δ-$TeO_2$ and * is an unknown phase [9, 13].

3.2.7 Behavior of silver within the germanotellurite glass matrix

The role of Ag_2O is important but its role within the glass matrix is unclear. Therefore, a photoluminescence (PL) experiment was carried out for the glasses under investigation. Effectively, the concentration of silver in the glass (3.56 at%) is reasonably large in comparison to several previous studies [32, 33], and clustering could be expected. The PL experiments were performed by using a 485 nm laser excitation which is at the wavelength cut-off of the transmission window of 7T1GxAg glass samples (Figure 3.4). Then the PL signals were detected in the

range 500-800 nm and are shown on **Figure 3.7**. The broad band observed between 500 and 800 nm, with maximum at ~650nm in 7T1G4Ag and 7T1G6Ag, and not present for 7T1G2Ag and 7T1G is due to presence of silver and not to glass matrix defects. Several studies of silver ion-doped soda-lime silicate glasses [32-34] have proved that an annealing step at 300ºC leads to the decrease of isolated Ag^+ and important modification of the photoluminescence behavior attributed to aggregation of 2 to 4 silver atoms during annealing [35]. Belharouak et al. [36] have studied phosphate glasses containing large concentrations of silver ions. In addition to the PL band observed between 300 and 450 nm for excitation at 280nm attributed to isolated Ag^+ ions, a broad PL band observed in the 450-800 nm range with maximum at 550 nm for excitation at 350 nm has been attributed to the formation of Ag^+-Ag^+ dimers. Considering our case, where excitation below 480nm cannot be performed because these radiation would be totally absorbed by the glass matrix, one can only suggest the presence of Ag^+-Ag^+ dimers or small silver ions clusters within the glasses with the higher content of Ag_2O (4-6%). They would be revealed by a maximum PL signal around 650 nm obtained from the tail of the excitation band. For lower Ag_2O ratio germanotellurite glasses (0-2%), the results show that silver is mainly present as isolated Ag^+. One has to notice that partially reduced silver clusters as well as isolated Ag^+, cannot be detected by photoluminescence due to the high cut-off wavelength value. Complementary Paramagnetic Electronic Resonance analysis could bring answer to this question [33].

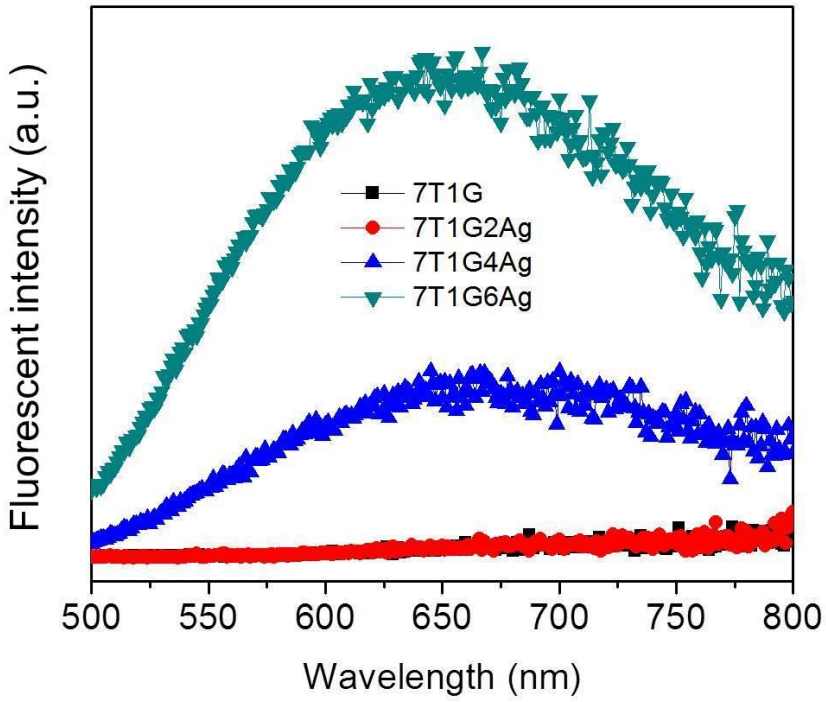

Figure 3.7: UV-Vis spectra of 7T1GxAg glasses (x=0,2,4,6).

3.2.8 Effect of silver oxide addition in the crystallization of 7T1GxAg glasses

The strong modification in thermal property has confirmed the role of Ag_2O as nucleating agent. From Figure 3.2, it is obvious that the 7T1G glass has favorable surface crystallization since the onset crystallization of powder DSC scan starts at lower temperature than the one for bulk sample. Apart from the observed decrease in T_g, the difference between surface and bulk DSC analysis is reduced and becomes null in the case of 7T1G6Ag. This indicates that it is possible to promote both bulk and surface crystallization with the incorporation of nucleating silver agents at the early stage of crystallization.

Furthermore, the main crystalline phase occurring in 7T1G glass was observed to be δ–TeO_2 (Fig. 3.6) which is not favorable to obtain second order optical properties, while, for 7T1GxAg (x≠0) samples, a phase showing SHG activity ($K[Nb_{1/3}Te_{2/3}]_2O_{4.8}$) is obtained. In addition, it was the unique phase appearing for the 6 mol% silver-containing glass ceramics. This phase had already been

reported in previous studies of tellurite glass systems [10, 37]. The cubic, centrosymmetric, fluorite-type (Figure 1.8) structure is consistent with our XRD (Figure 3.6) and theoretically is not SHG active. However, a slight distortion of the cubic structure was proposed to explain the nonlinear optical activity of glass ceramics containing this crystal (see Chapter 1) [37, 38]. Electron diffraction pattern obtained from TEM (see section 3.4) also confirms FCC cubic lattice with a lattice constant estimated a=5.47 Å, which is comparable with previous reported result in the tellurite glass system [39]. Explanation on the cause of distortion is still unclear but Kim et al. [40] has claimed that the atomic size of potassium metal ions may play an important role because a similar cubic crystalline phase of $Na[Nb_{1/3}Te_{2/3}]_2O_{4.8}$, does not show any SHG property. More details about the crystal phase will be discussed in Chapter 4.

3.3 Germanotellurite glass ceramics

3.3.1 Study of nucleation and silver aggregation during nucleation

To determine the temperature of maximum nucleation rate, a heat treatment based on Marotta's method was used. The method includes an intermediate thermal hold to induce exothermic peak temperature shifts [41]. The thermal program consists of a first heating step at a constant heating rate (e.g. 20K/min), followed by a 15 min nucleation heat treatment at a fixed temperature. After that, the samples are heated at the same heating rate (20K/min) to beyond the crystallization peak temperature. **Figure 3.8** illustrates the crystallization peaks obtained at different fixed temperatures from 320°C to 370°C with a 10°C step.

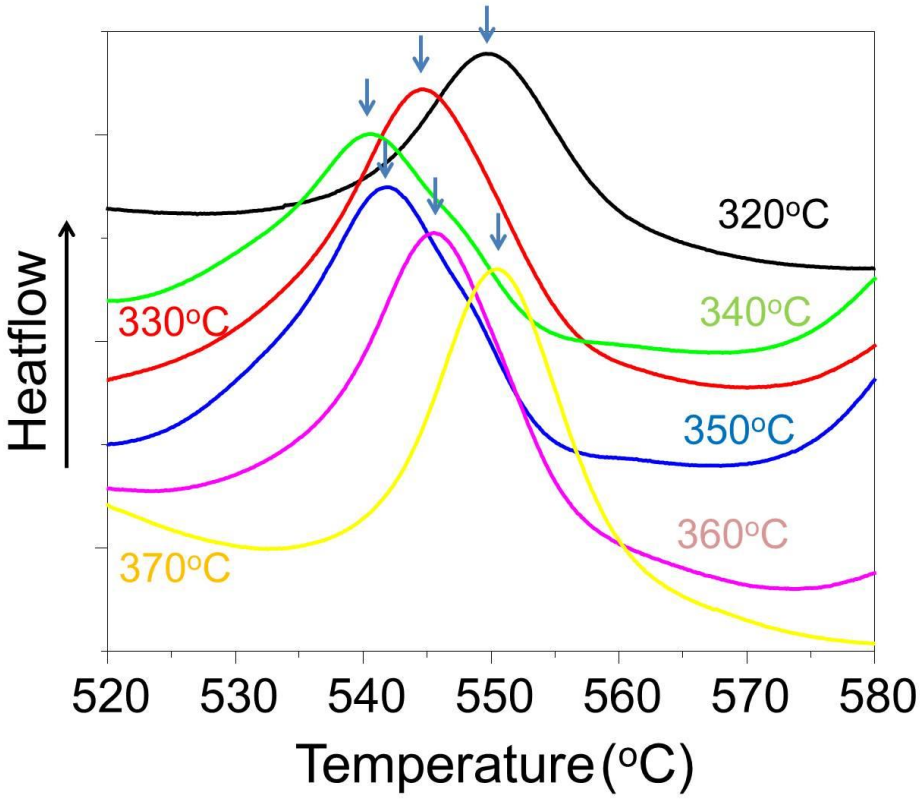

Figure 3.8: Crystallization peak obtained for different nucleation temperature

The analysis concentrates on the shifts of exothermic crystallization peak temperatures as illustrated in the equation below [42]:

$$\ln(I_o) = \frac{E_c}{R}\left(\frac{1}{T_p} - \frac{1}{T_p^o}\right) + const \quad (3.2)$$

Where I_o is the steady-state nucleation rate; T_p and T_p^o are peak temperatures with and without the intermediate thermal hold.

Based on the Equation 3.2, the maximum nucleation rate is expected to occur for the lowest T_p (Figure 3.8, blue arrow) obtained after the thermal hold at a fixed temperature. As observed in Figure 3.8 which 7T1G6Ag was determined as 340°C which is close to T_g (339°C).

In order to study the behavior of silver within the glass matrix during the nucleation step, the 7T1G6Ag glass was heat treated at 340°C to promote nucleation.

Different treatment durations were performed from 30 min to 24 hours. **Figure 3.9** shows the UV/Vis transmission spectra of all heat treated sample with regard to the as-pristine 7T1G6Ag glass. In general, the transmittance decreases proportionally with the treatment duration. For the 24h heat treated sample, the transparency decreases ~25% in comparison to the original 7T1G6Ag glass sample. However, the TEM analysis could not exhibit any crystallization nor any evolution of the separated droplets in size.

Furthermore, a hump occurs at around 500 nm for the 30 min treated sample. This hump is not witnessed for longer treatment times. Therefore, this hump could be assigned to the plasmonic band due to the presence of silver nanoparticles. In literature, the plasmonic effect of silver nanoparticles depends on the size and shape of the particles as well as the refractive index of the medium around [43-45]. Some studies [46, 47] announced that the plasmonic wavelength ranges from 400 nm to 500 nm. However, the red shift of plasmonic wavelength was also observed in high refractive index medium. Rai et al. [43] refer that the wavelength can be illustrated by the following equation:

$$\lambda_m = \lambda_p \left[1 + \left(\frac{2+F}{1-F}\right) n_s^2\right]^{\frac{1}{2}} \quad (3.3)$$

where λ_m and λ_p are the localized surface plasmon resonance (LSPR) absorption maximum and the wavelength of the plasmon resonance peak of bulk metal, respectively; F is the volume fraction; n_s is the refractive index of the effective medium surrounding.

The appearance of plasmonic effects suggests the agglomeration of silver and reduction of silver ions during the nucleation step. The disappearance of the plasmonic hump after that could be assigned to the change of particle size. The size of the silver nanoparticles was observed to decrease in several studies upon heat treating the samples [48, 49]. The mechanism of this degradation is suggested to relate to the total Gibbs free energy. When the particle size exceeds

a critical limit size (r_c), the silver particle will lose Ag^o in order to reduce the Gibbs free energy.

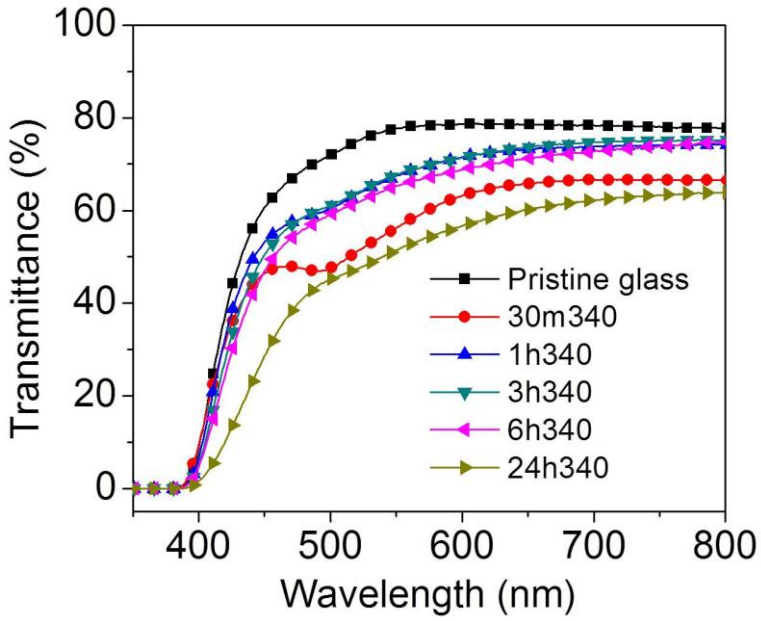

Figure 3.9: Transmission spectra of 7T1G6Ag glass heat treated at 340°C. The hump occurs after 30 min but disappear after that.

3.3.2 Glass ceramics preparation

Glass ceramics were elaborated from the 7T1G6Ag based glass using different heat treatments in order to promote nucleation and/or crystal growth. One should note that various nucleation and growth temperatures and durations were tested. In this study, we have focused our attention on the two most representative series of obtained samples: (i) samples labeled 1S05, 1S15, and 1S30 were prepared by one-step treatment at 440°C (>T_{x1}, see Table 3.2) during 5, 15, and 30 minutes respectively and (ii) samples based on a 2-step treatment consisting of a the first step at 340°C (as determined by the Marotta method – see section 3.3.1) during 3 hours to promote the nucleation and second growth step at 400°C during 15 minutes (2S15) and 30 minutes (2S30). All glass ceramic samples were finally polished again on both sides to remove possible surface crystallization (**Figure 3.10**). Another sample 2S8h (3 hours at 340°C for nucleation and 8 hours at 400°C

for crystal growth) was prepared to exhibit a highly crystallized X-ray diffraction (XRD) pattern.

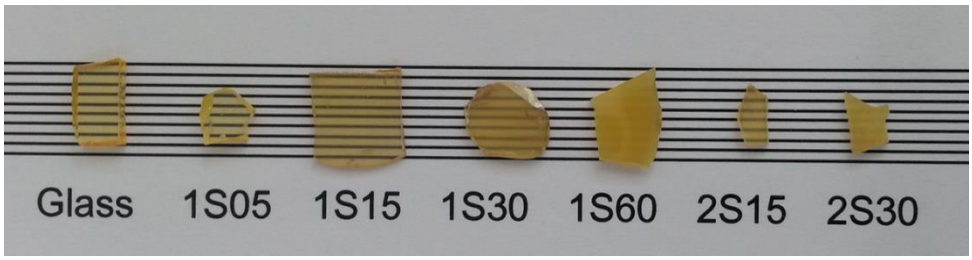

Figure 3.10: Glass ceramic samples elaborated through 1-step and 2-step heat treatments.

Optical microscopic images of 1S15, 1S30, 2S15 and 2S30 samples are shown in **Figure 3.11**. After different heat treatments, domains in microscopic scale can be observed at the early stage of crystallization. The domains within the 1-step heat-treated samples have the shape of 6-pointed or 8-pointed star-like polygons and their size increases from less than 1μm in diameter (1S05) to around 8 μm (1S30). On the other hand, the 2-step heat-treated samples appear textured in its entire volume. The size of the domains forming this texture is too small to be determined by optical microscopy.

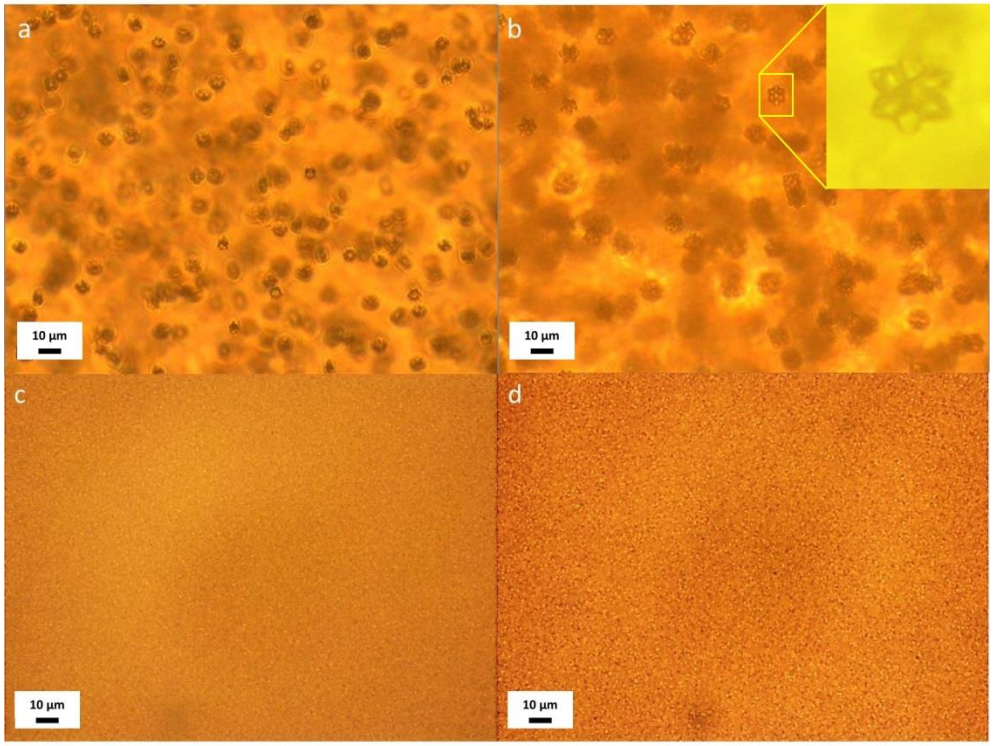

Figure 3.11: Optical microscopy images of phase separation domains which are labeled as follows: (a) 1S15, (b) 1S30, (c) 2S15 and (d) 2S30.

Figure 3.12 presents the X-ray patterns of heat treated glass samples 1S05, 1S15, 1S30, 2S15, 2S30 and 2S8h. The 2S8h pattern shows the presence of a unique crystalline phase that have been assigned to the crystalline phase $K[Nb_{1/3}Te_{2/3}]_2O_{4.8}$ [50]. The most intense peaks characterizing this crystal phase are observed on other XRD patterns except 2S05, leading to the conclusion that crystal growth of $K[Nb_{1/3}Te_{2/3}]_2O_{4.8}$ already occurs for sufficient growing treatment duration. But crystallization rate in 1S and 2S glass ceramic series is still low.

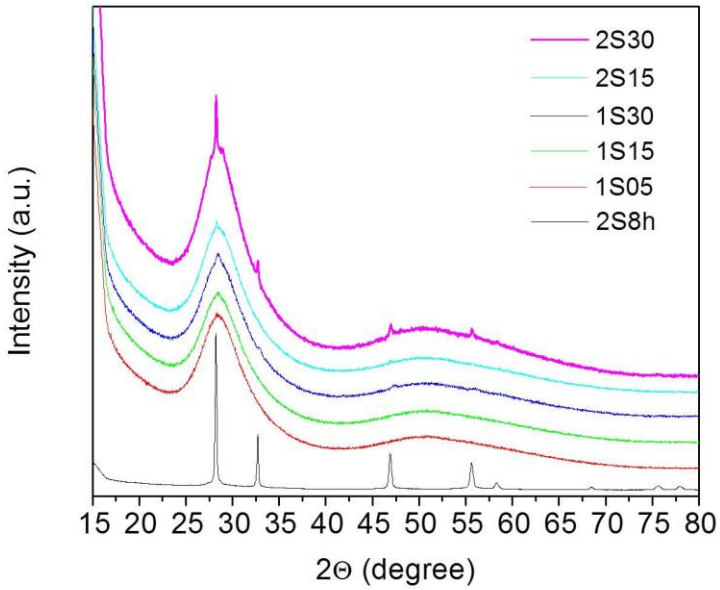

Figure 3.12: **XRD powder patterns of all heat treated samples and the fully crystalline 2S8h which was developed for a clear observation of a unique phase of $K[Nb_{1/3}Te_{2/3}]_2O_{4.8}$.**

3.3.3 Optical transparency

The 7T1G6Ag glass ceramics fabricated by 1-step and 2-step (**Figure 3.13**) methods exhibit lower transparency than the original as-quenched 7T1G6Ag glass. This transmittance reduction is observed in both thermal processes. The loss of transparency observed in the visible range on Figure 3.13a and 3.13b is correlated to the optical microscopy imaging of Figure 3.11. The size and density of domains optically observed appears to be the main origin of transmittance reduction [7]. For the 1-step sample series, scattering losses seem to be related to the size of star polygon objects, as it coincides with the decrease of transmittance from 71.5% (800nm, 1S05) down to 15.2% (800nm, 1S30). For the 2-step annealed samples, the reduction rate is even more drastic. However, due to the combination of two steps (nucleation and crystal growth), the bulk density of these domains appears to increase making the glass ceramics to become translucent (2S15, 17.6%, 800nm) and even opaque (2S30, <1%, 800nm).

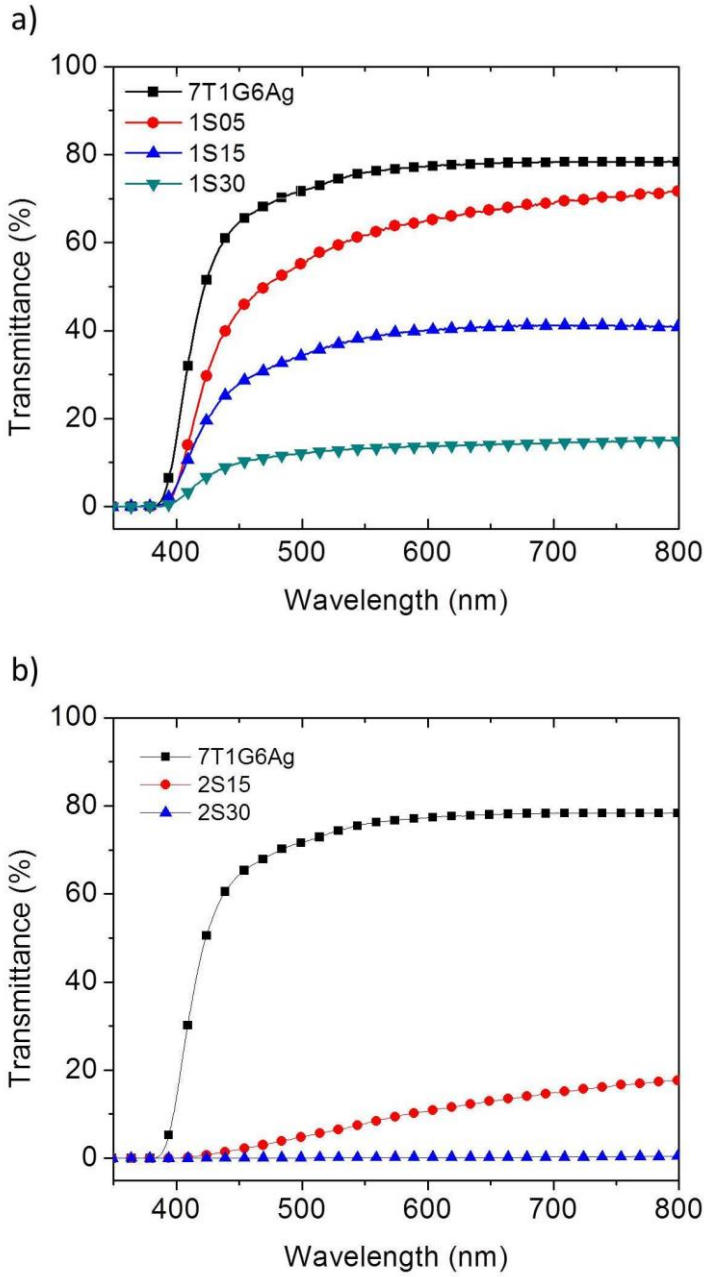

Figure 3.13: **(a) and (b) are transmittance spectra of glass ceramics elaborated via 1-step and 2-step thermal treatments, correspondingly.**

3.3.4 Nonlinear optical properties of germanotellurite glass ceramics

Macroscopic SHG studies of 1S05, 1S15, 1S30, 2S15 and 2S30 were made and some of them are illustrated in **Figure 3.14**. For each sample, polarization scans of the incident beam (Ψ scan) were performed. On the first tread, we focus only on the signal intensity. The dependence of SHG responses (Ψ scan curves) on

polarization and their relation with Chapter 2 will be treated later in Chapter 4. The SHG intensities of both 1-step and 2-step samples change with heat treatment time. However, results are quite different, since for similar crystal growth duration, the 1S- series always show a much stronger intensity than the 2S- ones. The SHG intensity of the 1S30 sample, for instance, is one order of magnitude higher than the one of the 2S30 sample. A signal increase is also observed in the 2-step samples when increasing the growing duration (Figure 3.14). This indicates that the nonlinear optical (NLO) signal increases with crystal growth thermal treatment duration.

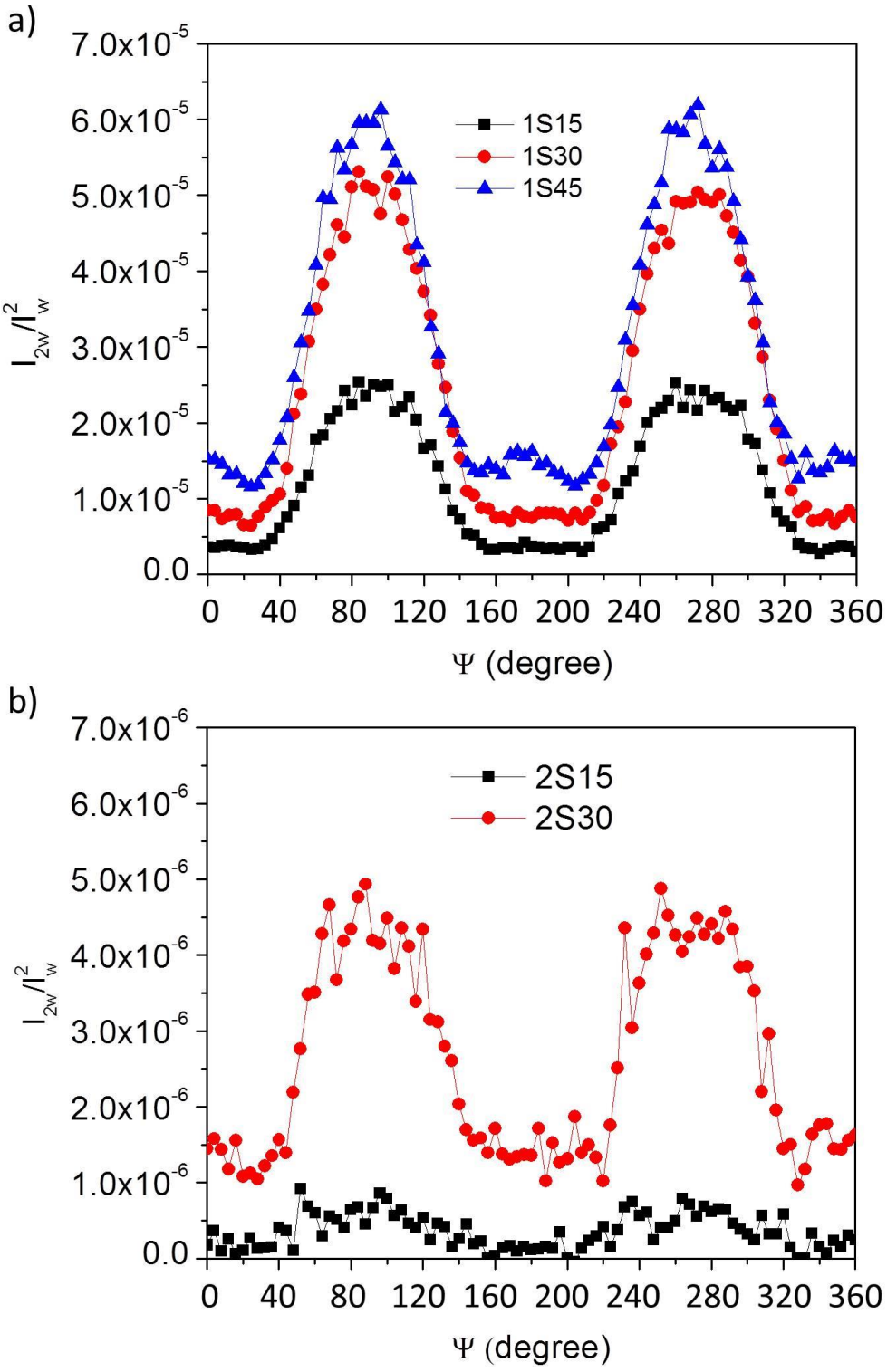

Figure 3.14: **Macroscopic nonlinear optical (NLO) signal (Ψ_p scan) of 1-step and 2-step treated glass ceramics materials in respect to treatment duration.**

3.4 Effects of 1-step and 2-step heat treatment to optical properties

Optical images from Figure 3.11 show several phase separated domains within the volume. The dependence of phase separated domains' number and size on the transparency and the optical nonlinearity of glass ceramics can be deduced from the results depicted in Figures 3.12, 3.13 and 3.14.

Phase separation already occurs in the as-quenched glasses and is observed by TEM technique (Figure 3.5 a-b) as nanometric droplets. Some assumptions in the literature in comparable glass systems assigned them to TeO_2, GeO_2 and/or NbO_6 enriched regions [12, 51, 52]. Although there are some open questions about the nature of separated phase in the as-quenched glass and the correlation with the separation process observed in the Figure 3.11 with the crystal growing, TEM images don't show any evolution of size and density of these small droplets after nucleation or crystallization. Nevertheless, the importance of the phase separation observed by optical microscopy in these glass ceramics should be carefully considered to explain the loss of transparency and evolution of SHG signal.

Furthermore, it is noted that the XRD patterns of all the glass ceramic samples show the dominance of amorphous background with a low ratio of crystallization with nanometer scale crystallites. The size of crystallites is estimated around 20nm for 1S30 and around 60 nm for 2S15. This size has been confirmed by TEM imaging of the highly crystallized 7T1G6Ag glass ceramic sample (2S8h sample) (**Figure 3.15**).

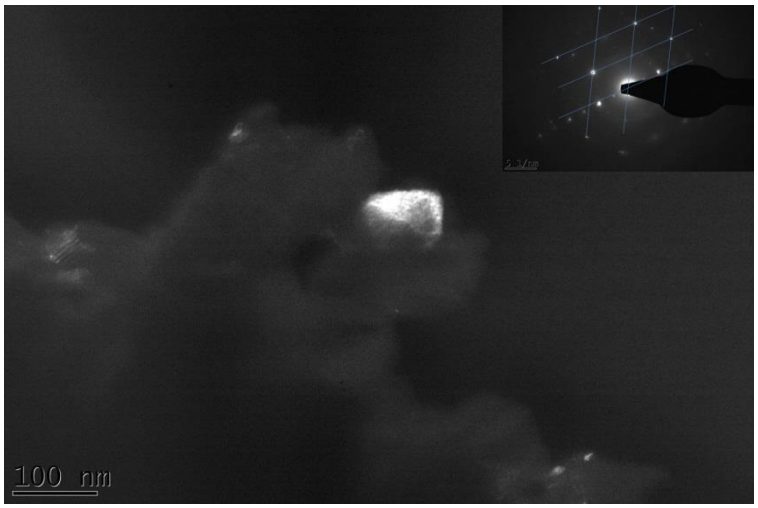

Figure 3.15: TEM image of a crystal in a high crystallized 7T1G6Ag glass ceramics (2S8h). The size is around 70-80 nm.

In order to investigate the position of nanometric crystallites in the glass ceramic, micro-SHG mapping was performed in the vicinity of a microscopic phase separated domain within the 1S30 sample. **Figure 3.16** shows the micro-SHG map of a star-like domain within the 1S30 glass ceramics (~8μm in size). The map clearly indicates that the SHG responses fully localize within the star-like domain.

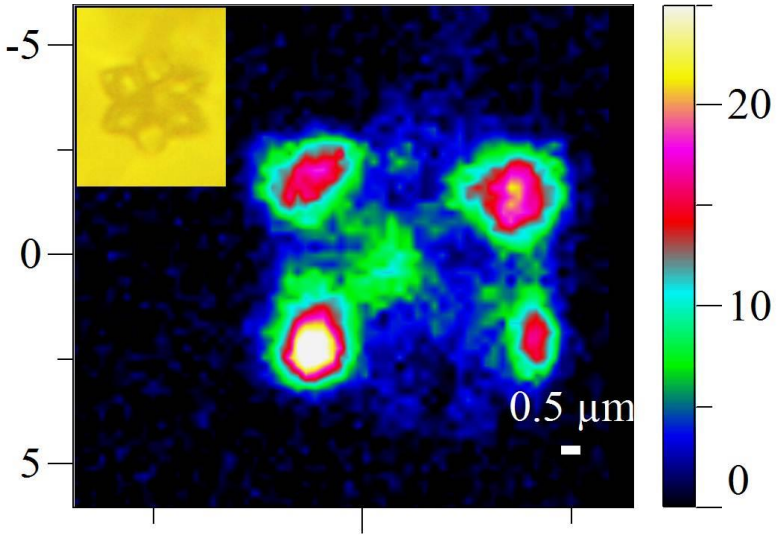

Figure 3.16: Microscopic SHG map of a phase separated domain (inset) within the 1S30 glass ceramic.

To correlate the origin of SHG signal with the size and distribution of the domains, the 2S15 and 1S30 samples are chosen for further studies because they have

quite identical transmission spectrum (Figure 3.13). **Figure 3.17** (onset) also indicates that the ratio of crystallites in both samples is similar as observed by XRD. However, their SHG intensities are dramatically different from each other. The 1S30 sample shows a two-order of magnitude stronger signal than the 2S15 one. Finally, as transmittance and XRD pattern of these two samples are similar, it is obvious that both scattering losses and volume of crystal fraction are not at the origin of the large SHG intensity difference observed.

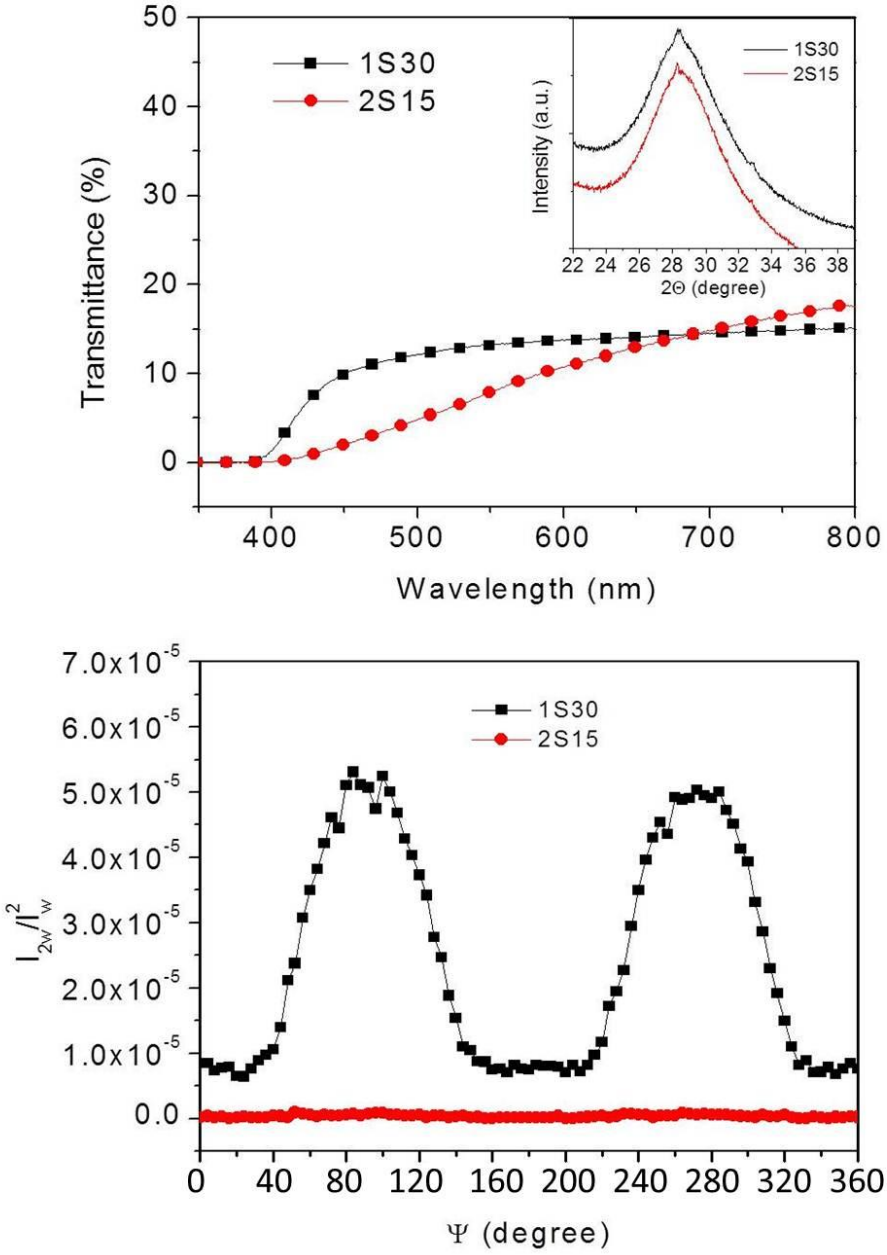

Figure 3.17: Ψp scans of 1S30 and 2S15 glass ceramics. The one-step sample shows two-order stronger signal than two-step one even with higher dispersed concentration of phase separation domains. The onset show the XRD patterns of

The above observation should be explained after successful correlation between the crystallites' organization inside the star-like phase separated domains and the output macroscopic SHG signal. In fact, the origin of SHG signal from the ceramic part is still in debate mainly because of the misunderstanding of the crystal

arrangement and its evolution with the thermal treatment. Some recent studies support this hypothesis. Previous study has proved that $LiNbO_3$ crystallites within a spherulite in silicate-based glass ceramics grow with their c-axis radially oriented whereas Truong et al. has indicated the existence of more complex local $LaBGeO_5$ crystal structuring within a spherulite in niobium borogermanate glass [6, 53]. It is important to emphasize that the 6-polygon star-like shape domains in 1S30 glass ceramics sample implies a complex organization of crystallites.

A factor which can affect the SHG signal is the interference elimination from different parts of the crystallized domains which directly relates to the comparison between the domain size and the wavelength or coherence length [54]. Vigouroux et al. [6] has explained that a spherical phase-separated domain of 30μm in diameter (longer than coherence L_c and wavelength λ) containing $LiNbO_3$ crystallites in silica glass should be considered as two separated zones with opposite crystal orientation. Therefore, the SHG signals from these two zones can be combined in keeping the polarization information on emitted SHG signals. From Figure 3.11 and 3.17 it can be noted that the 1S30 sample with larger size domains (estimated coherence length $L_c \approx 6\mu m$) will have less impact by destructive interference than 2S15 and, therefore, shows more intense SHG signal. However, further studies should be performed to figure out the organization, namely the orientation, of crystallites within these separated domains. This point will be further discussed in Chapter 4.

3.5 Conclusion

In this chapter, we demonstrate the possibility to elaborate glass with different amounts of silver oxide content. The addition of silver oxide as a nucleation agent promotes bulk crystallization. The uniquely crystalline phase induced by heat treatment in those samples is $K[Nb_{1/3}Te_{2/3}]_2O_{4.8}$, which was demonstrated to contain optical nonlinearity. In order to favor a strong nucleation of this crystalline phase, 6 %mol of Ag_2O was added to the nominal glass composition which was then heat-treated to foster the phase separation domain.

The results presented here show that, although a 2-step heat treatment can improve nucleation step, it also enhances phase separation and quickly decreases the transparency of glass ceramics. On the other hand, the 1-step heat treatment promotes the star-like domains, in which $K[Nb_{1/3}Te_{2/3}]_2O_{4.8}$ crystallites appear. Furthermore, this study suggests that the SHG intensity is strongly related to the size and the organization of the crystallized domains.

REFERENCES

1. Bloembergen, N., R. Chang, S. Jha, and C. Lee, *Optical second-harmonic generation in reflection from media with inversion symmetry.* Physical Review, 1968. **174**(3): p. 813.
2. Jain, H., *Transparent ferroelectric glass-ceramics.* Ferroelectrics, 2004. **306**(1): p. 111-127.
3. Kaminskii, A., A. Butashin, I. Maslyanizin, B. Mill, V. Mironov, S. Rozov, S. Sarkisov, and V. Shigorin, *Pure and Nd3+-, Pr3+-Ion Doped Trigonal Acentric LaBGeO5 Single Crystals Nonlinear Optical Properties, Raman Scattering, Spectroscopy, Crystal-Field Analysis, and Simulated Emission of Their Activators.* physica status solidi (a), 1991. **125**(2): p. 671-696.
4. Eckardt, R., H. Masuda, Y.X. Fan, and R.L. Byer, *Absolute and relative nonlinear optical coefficients of KDP, KD* P, BaB 2 O 4, LiIO 3, MgO: LiNbO 3, and KTP measured by phase-matched second-harmonic generation.* Quantum Electronics, IEEE Journal of, 1990. **26**(5): p. 922-933.
5. Günter, P., P. Asbeck, and S. Kurtz, *Second-harmonic generation with Ga1− xAlxAs lasers and KNbO3 crystals.* Applied Physics Letters, 2008. **35**(6): p. 461-463.
6. Vigouroux, H., E. Fargin, S. Gomez, B. Le Garrec, G. Mountrichas, E. Kamitsos, F. Adamietz, M. Dussauze, and V. Rodriguez, *Synthesis and Multiscale Evaluation of LiNbO3-Containing Silicate Glass-Ceramics with Efficient Isotropic SHG Response.* Advanced Functional Materials, 2012. **22**(19): p. 3985-3993.
7. Beall, G. and D. Duke, *Transparent glass-ceramics.* Journal of Materials Science, 1969. **4**(4): p. 340-352.
8. Kim, S.H., T. Yoko, and S. Sakka, *Linear and nonlinear optical properties of TeO2 glass.* Journal of the American Ceramic Society, 1993. **76**(10): p. 2486-2490.
9. Komatsu, T. and T. Honma, *Optical Active Nano-Glass-Ceramics.* International Journal of Applied Glass Science, 2013. **4**(2): p. 125-135.
10. Sakai, R., Y. Benino, and T. Komatsu, *Enhanced second harmonic generation at surface in transparent nanocrystalline TeO2-based glass ceramics.* Applied Physics Letters, 2000. **77**(14): p. 2118-2120.
11. Ferreira, E.A., F.C. Cassanjes, and G. Poirier, *Crystallization behavior of a barium titanate tellurite glass doped with Eu3+ and Er3+.* Optical Materials, 2013. **35**(6): p. 1141-1145.
12. Monteiro, G., L.F. Santos, J. Pereira, and R.M. Almeida, *Optical and spectroscopic properties of germanotellurite glasses.* Journal of Non-Crystalline Solids, 2011. **357**(14): p. 2695-2701.
13. Monteiro, G., L.F. Santos, R.M. Almeida, and F. D'Acapito, *Local structure around Er 3+ in GeO 2–TeO 2–Nb 2 O 5–K 2 O glasses and glass-ceramics.* Journal of Non-Crystalline Solids, 2013. **377**: p. 129-136.
14. Ahmed, A., A. Ali, D.A. Mahmoud, and A. El-Fiqi, *Preparation and characterization of antibacterial P2O5–CaO–Na2O–Ag2O glasses.* Journal of Biomedical Materials Research Part A, 2011. **98**(1): p. 132-142.
15. Udovic, M., P. Thomas, A. Mirgorodsky, O. Durand, M. Soulis, O. Masson, T. Merle-Mejean, and J.-C. Champarnaud-Mesjard, *Thermal characteristics, Raman spectra and structural properties of new tellurite glasses within the Bi 2 O 3–TiO 2–TeO 2 system.* Journal of Solid State Chemistry, 2006. **179**(10): p. 3252-3259.
16. Upender, G., J.C. Babu, and V.C. Mouli, *Structure, glass transition temperature and spectroscopic properties of 10Li 2 O–xP 2 O 5–(89− x) TeO 2–1CuO (5≤ x≤ 25mol%) glass system.* Spectrochimica Acta Part A: Molecular and Biomolecular Spectroscopy, 2012. **89**: p. 39-45.

17. Kosuge, T., Y. Benino, V. Dimitrov, R. Sato, and T. Komatsu, *Thermal stability and heat capacity changes at the glass transition in K 2 O–WO 3–TeO 2 glasses.* Journal of non-crystalline solids, 1998. **242**(2): p. 154-164.
18. Lin, J., W. Huang, Z. Sun, C.S. Ray, and D.E. Day, *Structure and non-linear optical performance of TeO2–Nb2O5–ZnO glasses.* Journal of non-crystalline solids, 2004. **336**(3): p. 189-194.
19. Chowdari, B.V.R. and P. Pramoda Kumari, *Structure and ionic conduction in the Ag2O·WO3·TeO2 glass system.* Journal of Materials Science, 1998. **33**(14): p. 3591-3599.
20. Rivero, C., R. Stegeman, K. Richardson, G. Stegeman, G. Turri, M. Bass, P. Thomas, M. Udovic, T. Cardinal, and E. Fargin, *Influence of modifier oxides on the structural and optical properties of binary TeO2 glasses.* Journal of applied physics, 2007. **101**(2): p. 23526-23526.
21. Guery, G., T. Cardinal, A. Fargues, V. Rodriguez, M. Dussauze, D. Cavagnat, P. Thomas, J. Cornette, P. Wachtel, and J.D. Musgraves, *Influence of Hydroxyl Group on IR Transparency of Tellurite-Based Glasses.* International Journal of Applied Glass Science, 2014. **5**(2): p. 178-184.
22. Wang, C.Y., Z.X. Shen, and B.V.R. Chowdari, *Raman Studies of Ag2O·WO3 ·TeO2 Ternary Glasses.* Journal of Raman Spectroscopy, 1998. **29**(9): p. 819-823.
23. Komatsu, T., K. Shioya, and K. Matusita, *Fabrication of transparent tellurite glasses containing potassium niobate crystals by an incorporation method.* Journal of the American Ceramic Society, 1993. **76**(11): p. 2923-2926.
24. El-Mallawany, R.A., *Tellurite glasses handbook: physical properties and data*. 2011: CRC press.
25. Cardinal, T., *Propriétés optiques non linéaires des verres borophosphatés de titane ou de niobium*. 1997.
26. Wang, Z. and L. Cheng, *Effects of doping CeO2/TiO2 on structure and properties of silicate glass.* Journal of Alloys and Compounds, 2014. **597**: p. 167-174.
27. Mott, N.F. and E.A. Davis, *Electronic processes in non-crystalline materials*. 2012: Oxford University Press.
28. Amjad, R.J., M. Dousti, and M. Sahar, *Spectroscopic investigation and Judd–Ofelt analysis of silver nanoparticles embedded Er 3+-doped tellurite glass.* Current Applied Physics, 2015. **15**(1): p. 1-7.
29. De Araujo, C.B., D. Silvério da Silva, T.A. Alves de Assumpção, L.R.P. Kassab, and D. Mariano da Silva, *Enhanced optical properties of germanate and tellurite glasses containing metal or semiconductor nanoparticles.* The Scientific World Journal, 2013. **2013**.
30. Yankov, G., L. Dimowa, N. Petrova, M. Tarassov, K. Dimitrov, T. Petrov, and B.L. Shivachev, *Synthesis, structural and non-linear optical properties of TeO 2–GeO 2–Li 2 O glasses.* Optical Materials, 2012. **35**(2): p. 248-251.
31. Champarnaud-Mesjard, J., S. Blanchandin, P. Thomas, A. Mirgorodsky, T. Merle-Mejean, and B. Frit, *Crystal structure, Raman spectrum and lattice dynamics of a new metastable form of tellurium dioxide: γ-TeO 2.* Journal of physics and chemistry of solids, 2000. **61**(9): p. 1499-1507.
32. Paje, S., J. Llopis, M. Villegas, and J.F. Navarro, *Photoluminescence of a silver-doped glass.* Applied Physics A, 1996. **63**(5): p. 431-434.
33. Eichelbaum, M., K. Rademann, A. Hoell, D.M. Tatchev, W. Weigel, R. Stößer, and G. Pacchioni, *Photoluminescence of atomic gold and silver particles in soda-lime silicate glasses.* Nanotechnology, 2008. **19**(13): p. 135701.
34. Villegas, M., J. Fernández Navarro, S. Paje, and J. Llopis, *Optical spectroscopy of a soda lime glass exchanged with silver.* Physics and chemistry of glasses, 1996. **37**(6): p. 248-253.
35. Bourhis, K., *Photostructuration par laser infrarouge femtoseconde de verres photosensibles de phosphates de zinc, d'argent et de gallium*. 2011, Université Sciences et Technologies-Bordeaux I.

36. Belharouak, I., H. Aouad, M. Mesnaoui, M. Maazaz, C. Parent, B. Tanguy, P. Gravereau, and G. Le Flem, *Crystal Structure and Luminescence Properties of Silver in AgM (PO 3) 3 (M= Mg, Zn, Ba) Polyphosphates.* Journal of Solid State Chemistry, 1999. **145**(1): p. 97-103.
37. Kim, H.G., T. Komatsu, K. Shioya, K. Matusita, K. Tanaka, and K. Hirao, *Transparent tellurite-based glass-ceramics with second harmonic generation.* Journal of non-crystalline solids, 1996. **208**(3): p. 303-307.
38. Jeong, E., J. Bae, M. Ha, H. Kim, H. Pak, B. Ryu, and T. Komatsu, *Structure of a nanocrystalline phase with second harmonic generation.* Journal-Korean Physical Society, 2007. **51**: p. S32.
39. Jeong, E., J. Bae, T. Hong, K. Lee, B. Ryu, T. Komatsu, and H. Kim, *Thermal properties and crystallization kinetics of tellurium oxide based glasses.* Journal of Ceramic Processing Research, 2007. **8**(6): p. 417.
40. Kim, H. and T. Komatsu, *Fabrication and properties of transparent glass-ceramics in Na2O-Nb2O5-TeO2 system.* Journal of materials science letters, 1998. **17**(13): p. 1149.
41. Marotta, A., A. Buri, F. Branda, S. Saiello, J. Simmons, D. Uhlmann, and G. Beall, *Nucleation and crystallization in glasses, advances in ceramics.* The American Ceramic Society, 1982.
42. Davis, M.J. and I. Mitra, *Crystallization measurements using DTA methods: applications to Zerodur®.* Journal of the American Ceramic Society, 2003. **86**(9): p. 1540-1546.
43. Rai, V., A. Srivastava, C. Mukherjee, and S. Deb, *Localized surface plasmon resonance (LSPR) and refractive index sensitivity of vacuum evaporated nanostructured gold thin films.* arXiv preprint arXiv:1406.4605, 2014.
44. Mock, J., M. Barbic, D. Smith, D. Schultz, and S. Schultz, *Shape effects in plasmon resonance of individual colloidal silver nanoparticles.* The Journal of Chemical Physics, 2002. **116**(15): p. 6755-6759.
45. Lee, K.-S. and M.A. El-Sayed, *Gold and silver nanoparticles in sensing and imaging: sensitivity of plasmon response to size, shape, and metal composition.* The Journal of Physical Chemistry B, 2006. **110**(39): p. 19220-19225.
46. Mock, J.J., D.R. Smith, and S. Schultz, *Local refractive index dependence of plasmon resonance spectra from individual nanoparticles.* Nano Letters, 2003. **3**(4): p. 485-491.
47. González, A., C. Noguez, J. Beránek, and A. Barnard, *Size, Shape, Stability, and Color of Plasmonic Silver Nanoparticles.* The Journal of Physical Chemistry C, 2014. **118**(17): p. 9128-9136.
48. Rivera, V., S. Osorio, D. Manzani, Y. Messaddeq, L. Nunes, and E. Marega, *Growth of silver nano-particle embedded in tellurite glass: Interaction between localized surface plasmon resonance and Er 3+ ions.* Optical Materials, 2011. **33**(6): p. 888-892.
49. Amjad, R.J., M. Dousti, M. Sahar, S. Shaukat, S. Ghoshal, E. Sazali, and F. Nawaz, *Silver nanoparticles enhanced luminescence of Eu 3+-doped tellurite glass.* Journal of Luminescence, 2014. **154**: p. 316-321.
50. Shioya, K., T. Komatsu, H.G. Kim, R. Sato, and K. Matusita, *Optical properties of transparent glass-ceramics in K2O・Nb2O5・TeO2 glasses.* Journal of non-crystalline solids, 1995. **189**(1): p. 16-24.
51. Dimitriev, Y., E. Kashchieva, and M. Koleva, *Phase separation in tellurite glass-forming systems containing B2O3, GeO2, Fe2O3, MnO, CoO, NiO and CdO.* Journal of Materials Science, 1981. **16**(11): p. 3045-3051.
52. Hart, R.T., J.W. Zwanziger, and P.L. Lee, *The crystalline phase of (K 2 O) 15 (Nb 2 O 5) 15 (TeO 2) 70 glass ceramic is a polymorph of K 2 Te 4 O 9.* Journal of non-crystalline solids, 2004. **337**(1): p. 48-53.
53. Truong, L.N., M. Dussauze, E. Fargin, L. Santos, H. Vigouroux, A. Fargues, F. Adamietz, and V. Rodriguez, *Isotropic octupolar second harmonic generation response in LaBGeO5 glass-ceramic with spherulitic precipitation.* Applied Physics Letters, 2015. **106**(16): p. 161901.

54. Kurtz, S. and T. Perry, *A powder technique for the evaluation of nonlinear optical materials.* Journal of Applied Physics, 2003. **39**(8): p. 3798-3813.

CHAPTER 4 – CORRELATION BETWEEN STRUCTURAL ORGANIZATION OF CRYSTALLITES WITHIN A STAR-LIKE DOMAIN AND SHG PROPERTIES OF GLASS CERAMICS

Contents

CHAPTER 4 – CORRELATION BETWEEN STRUCTURAL ORGANIZATION OF CRYSTALLITES WITHIN A STAR-LIKE DOMAIN AND SHG PROPERTIES OF GLASS CERAMICS

Introduction

In chapter 3, we studied the thermal characteristics of germanotellurite glass in the composition of (100-x)(70TeO_2 – 10GeO_2 – 10Nb_2O_5 – 10K_2O) – xAg_2O (x=6 mol%). The consequence of introduction of silver oxide in this glass system is the enhancement of bulk crystallization. This indicates that silver ions play the role of nucleating agents to promote bulk crystallization. This leads to the appearance of a unique crystal phase in the bulk under controlled 1-step or 2-step thermal annealing processes (1S and 2S series, respectively). The crystalline phase is then defined as $K[Nb_{1/3}Te_{2/3}]_2O_{4.8}$ by XRD patterns (Figure 3.12 in Chapter 3).

Moreover, 1S and 2S series of SHG-active transparent glass ceramic samples with 6%Ag_2O have been elaborated and analyzed. Optical microscopy revealed phase-separated star-like domains homogeneously distributed in the bulk. Their size was increasing with thermal treatment duration from submicroscopic size to 15-20µm. Micro-SHG mapping of a star-like domain observed in 1S30 sample (Figure 3.16, Chapter 3) indicated that the SHG active crystallites are in the micron-size domains. However, XRD patterns of the same sample allowed estimating crystalline sizes around 20nm. So we conclude that they are embedded

in an amorphous state inside the star-like phase separated domains. Though the volume fraction of crystallization appears to be quite low in these domains, macroscopic SHG has been measured from the samples in transmission mode.

However, we discovered a significant difference in comparing the macroscopic SHG responses delivered by two samples with similar transmission and crystallization rate but submitted to two different heat treatments (i.e. one-step crystallization (1S30) versus two-step nucleation plus crystallization (2S15)). The size and volume density of star-like separated domains was also shown to be clearly different. The conclusion leads to the necessity to further investigate the complex organization of $K[Nb_{1/3}Te_{2/3}]_2O_{4.8}$ nanocrystallites within the star-like domains.

The role of such substructure has been evidenced in other glass ceramic systems as previously discussed in Chapter 2 (Part B). Vigouroux et al. have shown that, inside phase separated centro-symmetric spherulite in niobate silicate glass ceramics, the $LiNbO_3$ nano-crystallites were radially aligned along their c axis. Spherulites have two separated opposite parts which produce SHG signal without interference elimination when the size of the spherulite overcomes the coherence length [1]. Another study carried out on $LaBGeO_5$ glass ceramics showing precipitation of nano-crystallites inside microscopic size phase separated spherulite (Chapter 2, part B) has gone even further with an effort to simulate the macroscopic SHG patterns [2].

We will focus this chapter on characterization of the organization of nano-crystallites inside the domains. For this purpose, we will have to take into account the lack of researches devoted to the $K[Nb_{1/3}Te_{2/3}]_2O_{4.8}$ crystal phase such as second- and third-order nonlinear optical coefficients [3-8]. The 1S60 sample (60 min at 440^{o}C) was used for this purpose throughout this chapter. The sample containing large star-like domains ranging around 15µm was selected in order to facilitate the structural analysis.

A. EXPERIMANTAL RESULTS

4.1 Characterization of the phase separation

4.1.1 X-ray diffraction

Figure 4.1 shows the XRD patterns of the 1S60 and 2S8h samples for comparison. Both of them evidence a unique crystal phase which fits well with $K[Nb_{1/3}Te_{2/3}]_2O_{4.8}$ composition as reported in literature [5, 6, 9]. The XRD pattern consists of 4 main peaks at 28.2°, 32.7°, 46.9° and 55.6° which allows to estimate the lattice parameter a=5.47 Å considering the hypothesis of a FCC cubic phase [3]. The star-like domains embedded within the germanotellurite glass matrix can be observed in the inset of the figure. The phase separated domains in star-like shape have a size ranging from 15-17 µm and are homogeneously distributed. The crystallization occurs within these phase separated domains (Figure 3.16 and 3.17, Chapter 3) with mean size crystallites estimated from Scherrer equation based on the FWHM. The crystallites are in nanoscopic scale which range around 20nm (the 1S60 glass ceramic sample) and 45nm (the highly crystallized 2S8h sample). In contrast, the size of phase separated domains is around 10^3 larger than the size of the crystallites in 1S60. Despite of small evolution of the crystallite size, we can observe on Figure 4.1 a very low crystallization rate for 1S60 in the bulk when compared to 2S8h. Figure 4.1 inset allows considering phase separation occurring in few percent of the total volume of the bulk. From this consideration, we can deduce that the rate of crystallization occurring inside the phase separated domains is still very low; the domains are then mostly amorphous.

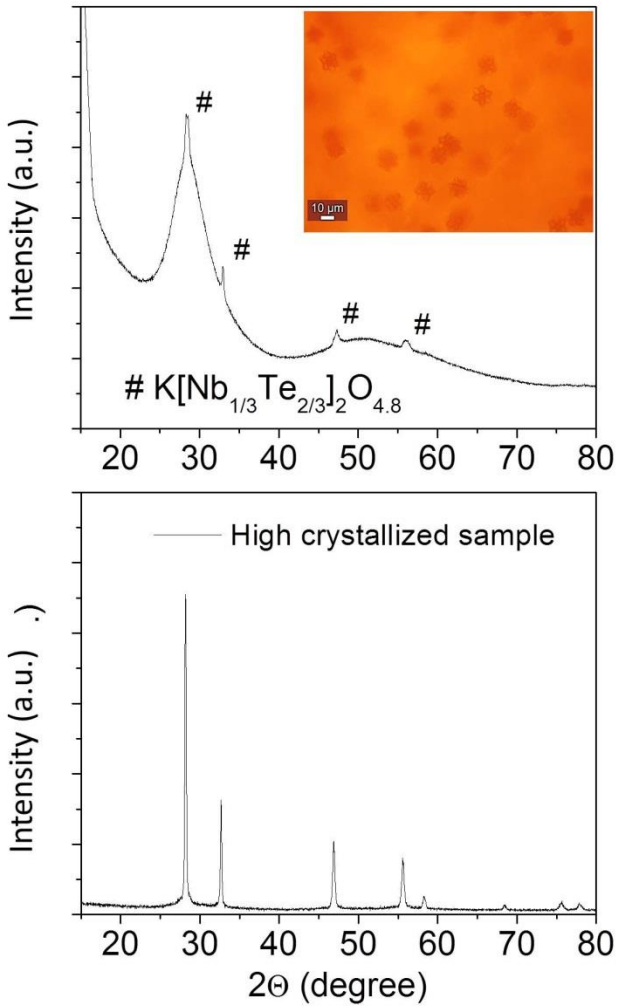

Figure 4.1: Optical microscopy images (inset) of phase separation domains which occurred during the heat treatment (60 min at 440°C, i.e. 1S60); XRD powder patterns of (a) 1S60 sample in comparison to (b) high crystallized samples (3h at 340°C plus 8h at 400°C, i.e. 2S8h). A clear observation of a unique phase of $K[Nb_{1/3}Te_{2/3}]_2O_{4.8}$ is obtained.

4.1.2 WDS analysis of the phase separation

In order to characterize the atomic rearrangement occurring in the two amorphous phases, e.g. the remaining glass matrix and the star-like domains, WDS quantitative element analysis was performed.

The atomic% (at%) of each element is quantified within and outside a selected domain through WDS technique described in Chapter 2 (Part A). The results are

illustrated in **Figure 4.2**. Clear contrast can be observed and **Table 4.1** illustrates the measured atomic percentages of all elements inside and outside the domain. The calculation of expected at% of elements in the as-quenched glass and in the crystal $K[Nb_{1/3}Te_{2/3}]_2O_{4.8}$ is also indicated for comparison. The glass matrix outside the domain shows a mean at% of elements which are very close to the expected values for the initial as-quenched glass, considering the % of error for this analysis technique. On the contrary, these values differ notably inside the domain. In comparison to the outside glass matrix, the ratio of germanium is very low. Besides that, while tellurium and oxygen at% seem to be unchanged, the decrease of potassium and increase of niobium and silver at% are significant. Furthermore, the proportions of elements within the domain do not fit well with what we expect in the crystal $K[Nb_{1/3}Te_{2/3}]_2O_{4.8}$. The potassium at% was effectively expected to increase inside the domain where precipitation of crystallites with larger concentrations of K is supposed to grow. The silver at%, on the contrary, seems to be gathered from the glass environment. According to a proposed hypothesis of silver and potassium exchange between the glass matrix and the studied separated domain, the crystal composition could take into account the presence of silver. Another hypothesis could be the decrease of potassium at% in the amorphous part of the domain due to the insertion of this element in the grown crystallites $K[Nb_{1/3}Te_{2/3}]_2O_{4.8}$ which is compensated by Ag diffusion from outside to the domain. In the absence of precise characterization of silver insertion in the crystal (crystallites are too small to be quantitatively analyzed by TEM), we will further use the following notation: $(Ag,K)[Nb_{1/3}Te_{2/3}]_2O_{4.8}$.

This hypothesis can be comforted by the lattice parameter $a = 5.47 \pm 0.01$ Å measured in Chapter 4.1.2 from XRD, in comparison with the parameter obtained for $K[Nb_{1/3}Te_{2/3}]_2O_{4.8}$ crystal $a = 5.54 \pm 0.01$ Å [10]. Considering smaller ionic radius of silver cations in comparison with potassium cations, the decrease of the lattice parameter could be the consequence of exchanging potassium to silver cations in the crystal composition. The same decrease of this constant had effectively been previously observed by Jeong et al. in the $72TeO_2 – 14Nb_2O_5 –$

xK_2O – $(14\text{-}x)Na_2O$ glass ceramics when potassium cations are progressively replaced by smaller sodium cation in the crystal structure [10].

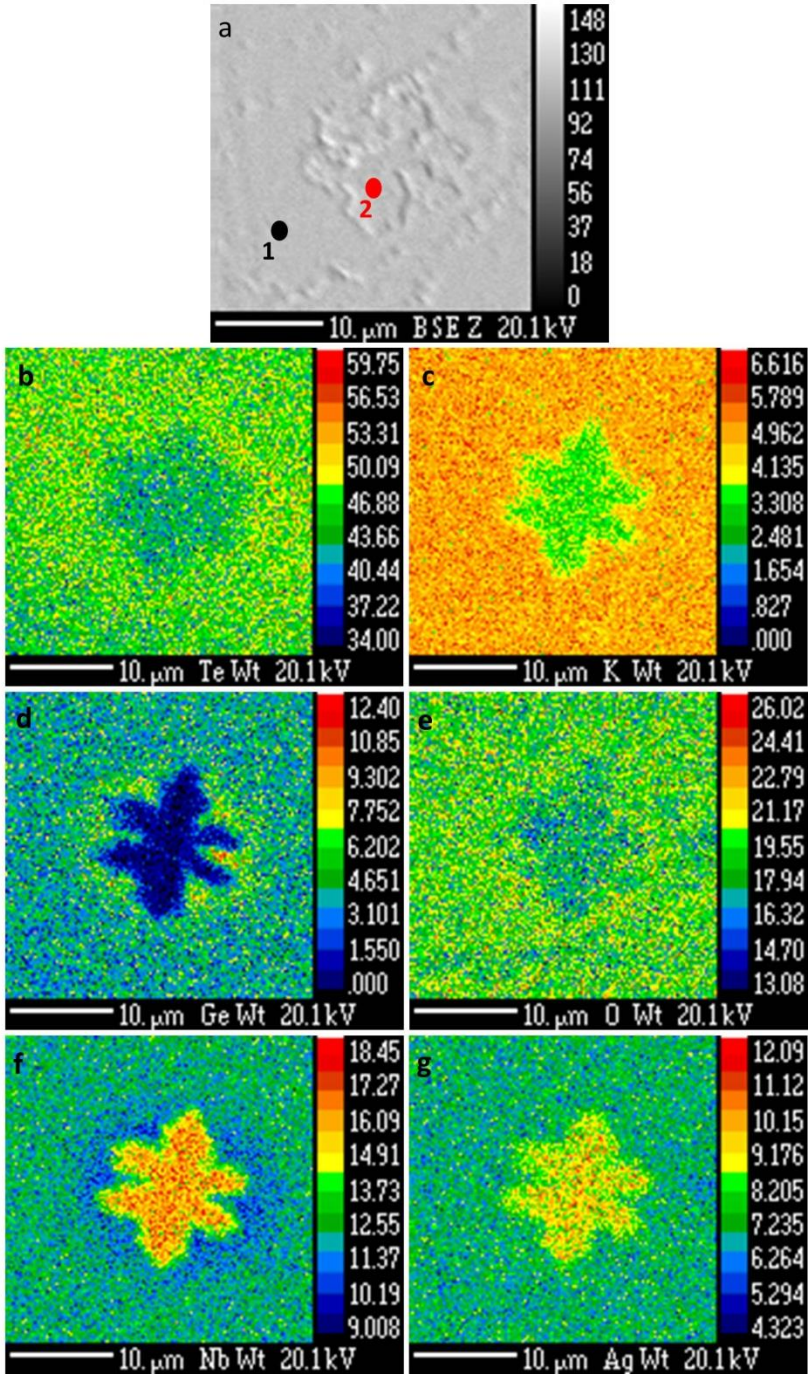

Figure 4.2: WDS quantitative element analysis mapping of a star-like phase separated domain (a). The directly obtained maps of Te, K, Ge, O, Nb and Ag WDS signal correspond to figure from (b) to (g), respectively.

It is interesting to observe that normalized at% of Te in Table 4.1 is the same outside and inside the domain, although WDS signal mapping in Figure 4.2b clearly shows a lower raw signal in the domain. One can make the same remark for oxygen atoms. This decrease of Te and O signals in the domain means there is less Te-O bonds and could be the signature of lower density. Interesting discussion can be given also on the halo we observe for Ge and Nb outside the interface. Ge atoms seem to pile up from the interface to the glass matrix, while Nb concentration is decreased from the glass matrix to the surface of the domain. These halos could be diffusion layers at the interface indicating more rapid kinetics for going across the interface compared to the diffusion kinetics of Ge and Nb in the glass matrix. Thinner halos are observed for K and Ag and could be explained by better diffusion kinetics of these elements in the glass matrix.

Table 4.1: Experimental quantitative analysis of elements outside (position 1 of Figure 4.2a or glass matrix) and inside (position 2 of Figure 4.2a or star-like object) the phase separated domain normalized for a total of 100%. The calculated at% of glass matrix is based on the 94($70TeO_2 – 10GeO_2 – 10Nb_2O_5 – 10K_2O$) – $6Ag_2O$ composition while the calculated at% of the domain indicates the crystal $K[Nb_{1/3}Te_{2/3}]_2O_{4.8}$ composition.

	Glass matrix (1)			Domain (2)		
	at% (cal.)	at% (Exp.)	Dev.	at% (cal.)	at% (Exp.)	Dev.
Te	19.49	18.80	0.44	17.09	18.78	0.21
K	5.57	6.30	0.07	12.82	4.81	0.07
Ge	2.78	3.08	0.19	-	0.73	0.24
O	63.03	61.57	0.65	61.54	61.72	0.31
Nb	5.57	6.83	0.20	8.55	9.3	0.24
Ag	3.55	3.42	0.10	-	4.65	0.10

From Table 4.1 where compositions are normalized to 100%, we observe little change in the composition of the remaining glass around the phase-separated domain despite the previous atomic migration to/from the separated domain previously described (e.g. the composition is a little bit rich in Ge and cations when

compared to the as-quenched glass). In the domain, the approximate mean composition $67TeO_2 – 16.5Nb_2O_5 – 16.5K_2O$ is measured. When compared to the composition of the crystal, the domain shows the same Te/Nb ratio but the proportion Te/(Ag+K) is lower.

4.2 Matching macro-SHG responses with mathematical model

The macro-SHG signal patterns of 1S60 were obtained in different measurement mode sets. The first one observed in **Figure 4.3a** shows the θ scans (θ_{ss}: θ_{xx}, θ_{sp}: θ_{xy}). Despite of the same pattern shape with maxima at normal incidence for the two Θ scans, we observe different maximum intensities (Figure 4.3a). Regarding to the Ψ scans (Ψ_p: $\Psi_{y;i,i}$ and Ψ_s: $\Psi_{x,i,i}$, where i is rotating excitation polarization from angle Ψ=0 to Ψ=360°, see Chapter 2), they are identical modulo Ψ=90° (Figure 4.3b) obtained from other glass ceramics in the same composition [1, 11]. It is worth to notice that the maxima of Ψ scans can be obtained when the incident polarization corresponds to analyzed harmonic signal. Moreover, the Ψ scans have the signature of a dipolar SHG behavior of the material (see Chapter 2). It was shown to be the consequence of the dipolar nature of the crystal nonlinear optical activity with a d_{33} predominant component.

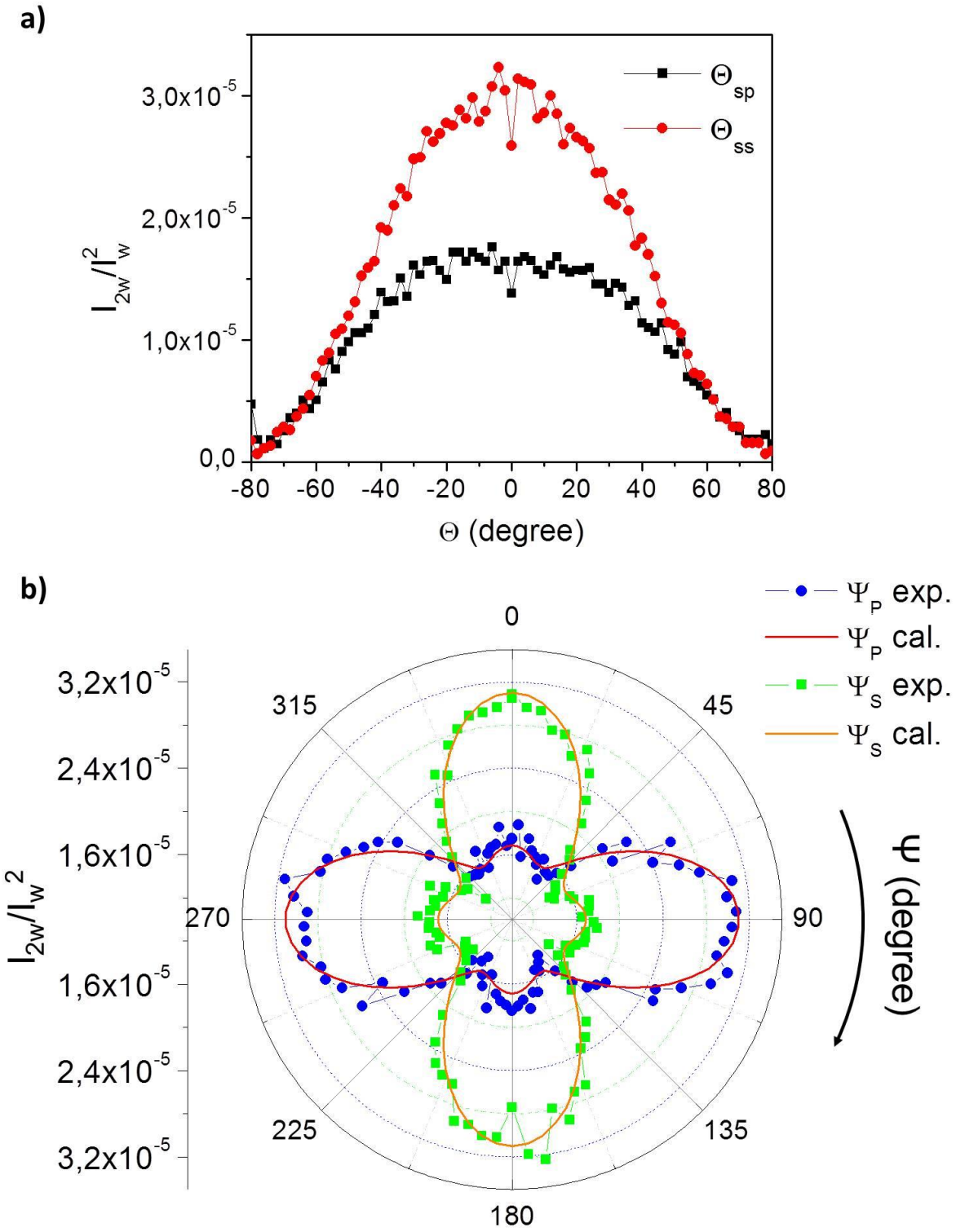
a)
3,0x10-5
2,0x10-5
1,0x10-5
0,0
I2w/Iw2
Θsp
Θss
-80 -60 -40 -20 0 20 40 60 80
Θ (degree)
b)
Ψp exp.
Ψp cal.
Ψs exp.
Ψs cal.
0
45
90
135
180
225
270
315
3,2x10-5
2,4x10-5
1,6x10-5
1,6x10-5
2,4x10-5
3,2x10-5
I2w/Iw2
Ψ (degree)

Figure 4.3: Experimental SHG of (a) θ_{ss}: θ_{xx} and θ_{sp} : θ_{xy} scans and (b) Ψ_p : $\Psi_{y;i,i}$ and Ψ_s : $\Psi_{x;i,i}$ scans in transmission mode through the 1S60 glass ceramic sample in comparison with simulated patterns (red an orange lines in (b)) extracted from Equations 4.6 and 4.7

We remind the Equation 2.3 developed in Chapter 2 to describe generally the SHG patterns of glass ceramics performed by Ψ scans:

$$I_{\Psi i}^{2\omega} \propto \left|P_i^{2\omega}(\Psi)\right|^2 = (E_o^{\omega})^4/8 \left|\left(\chi_{i;x,x}^{(2)}\right)^2 cos^4(\Psi) + \left(\chi_{i;y,y}^{(2)}\right)^2 sin^4(\Psi) + 2\left(2\left(\chi_{i;y,x}^{(2)}\right)^2 - \chi_{i;x,x}^{(2)}.\chi_{i;y,y}^{(2)}\right)\sin^2(\Psi)\cos^2(\Psi)\right| \quad (4.1)$$

where i=x,y.

It is notice that the macro-SHG results of the glass ceramics give some inputs for the mathematic expression. Experimentally, we observe from θ-scans (xx and xy in Figure 4.3a) and Ψ-scans (Ψ_p ans Ψ_s in Figure 4.3b) that firstly $I_{yy}^{2\omega} > I_{yx}^{2\omega}$ and $I_{xx}^{2\omega} > I_{xy}^{2\omega}$ (4.2), which implies $\left|\chi_{y;y,y}^{(2)}\right| > \left|\chi_{y;x,x}^{(2)}\right|$ and $\left|\chi_{x;x,x}^{(2)}\right| > \left|\chi_{x;y,y}^{(2)}\right|$ (4.3), and secondly $I_{\Psi y}^{2\omega} = I_{\Psi x}^{2\omega}$ but rotate 90° (Figure 4.3b), which implies by identification $\left|\chi_{y;x,x}^{(2)}\right| = \left|\chi_{x;y,y}^{(2)}\right|$ and $\left|\chi_{x;x,x}^{(2)}\right| = \left|\chi_{y;y,y}^{(2)}\right|$ (4.4).

From the experimental θ scans and Ψ scans where $I_{pp} = I_{ss} = \beta I_{sp} = \beta I_{ps}$ (or $\Theta_{pp} = \Theta_{ss} = \beta\Theta_{sp} = \beta\Theta_{ps}$, as observed in Figure 4.3), the existence of d_{31} and d_{33} coefficients in the crystal ONL tensor is confirmed. The decrease of SHG signal observed on Figure 4.3a when changing the detection polarization indicates that $d_{31}<d_{33}$.

Regarding to the hypothesis proposed by Vigouroux et al. [1], the summation of the signals delivered by all SHG-active domains containing crystals in the bulk of the glass ceramics (in respect to the coherence length) builds the macroscopic response of the sample. One can try to correlate the macro-SHG patterns with the mathematical model as performed for LNS and LBG glass ceramics in Chapter 2.

Now if we suppose that the Kleinman symmetry holds, we have $d_{31} = d_{15}$ and for all these point groups $d_{11} = d_{13} = 0$. d_{31} is then the only remaining term involved in crossed polarization studies.

After some developments, on the same model as we did for $LiNbO_3$-SiO_2 glass ceramics in Chapter 2 (equations 2.10 and 2.11 in Chapter 2), we obtain a correct simulation of Ψ scans for a value of β=2.1 representing the ratio between I_{pp} and I_{ps} signal intensity and scattering loss 0.15 which lead to:

$$I_{\Psi_y}^{2\omega} \propto 0.48cos^4\Psi + 0.52\,cos^2\,\Psi\,sin^2\Psi + sin^4\Psi + 0.15 \quad (4.6)$$

$$I_{\Psi_x}^{2\omega} \propto cos^4\Psi + 0.52\,cos^2\,\Psi\,sin^2\Psi + 0.48sin^4\Psi + 0.15 \quad (4.7)$$

According to literature, the crystalline $(Ag,K)[Nb_{1/3}Te_{2/3}]_2O_{4.8}$ phase would be monoaxial due to slight distortion of a fluorite-type structure [4, 8, 10]. Therefore, this phase would belong to the point groups of tetragonal crystal system which are C_4, S_4, C_{4v}, D_{2h}, and D_4. However, D_{2h} contains all zero scalars which should be ruled out. C_4 and C_{4v} point groups containing d_{33} and d_{31} components in the ONL tensor are then appropriate group symmetries for the crystal.

Considering the highest level of symmetry C_{4v} for simplification, then the d_{ij} components tensor would be:

$$C_{4v}\begin{pmatrix} 0 & 0 & 0 & 0 & d_{31} & 0 \\ 0 & 0 & 0 & d_{31} & 0 & 0 \\ d_{31} & d_{31} & d_{33} & 0 & 0 & 0 \end{pmatrix} \quad (4.5)$$

In comparison to the result obtained for LNS glass ceramic system, $\beta < \alpha$ which implies that the $(Ag,K)[Nb_{1/3}Te_{2/3}]_2O_{4.8}$ crystal phase and/or the crystallite arrangement within the star-like domain make it less dipolar than $LiNbO_3$ spherulite. This result means that we can propose the structural organization of crystallites within the star-like domain based on one dominant $\chi^{(2)}$ coefficient.

4.3 Correlation between local structural modification and SHG inside a star-like domain

4.3.1 Micro-Raman analysis

Regarding to the structural modification induced during the heat treatment and local organization of crystallization in the glass ceramics, micro-Raman characterizations were performed (see Chapter 2.2.6 for technical principles of the experimental set-up). A star-like shape separated domain ~15 µm was selected in 1S60. Then Raman spectra were registered in two different points outside (1) and inside (2) the domain (see the inset of **Figure 4.4a**). A general decrease of the Raman intensity all over the spectrum is observed within the phase separated domain. Though crystallization is occurring in this region, the corresponding Raman spectrum does not reveal any corresponding sharp peak. The decrease of the global signal could be explained from lower density of the material inside the domain and/or modifications of the atomic bonds. Furthermore, comparing with the surrounding glass matrix, the WDS signal of Te and O elements in the studied domain was shown to be lower (see Figure 4.2). As bonds between those two elements are at the origin of the stronger Raman active bonds in the 400-800cm^{-1} region in the glass spectrum (see Chapter 3.2.4), one could justify the global decrease of the Raman signal by a lower volume number of Te-O bonds. One can also observe fluctuation of the integrated signal in full range 300-1000 cm^{-1} proving the existence of microscopic size non homogeneous zones inside the domain (Figure 4.4). One can also suggest a loss of the global intensity due to scattering in the heterogeneous domains.

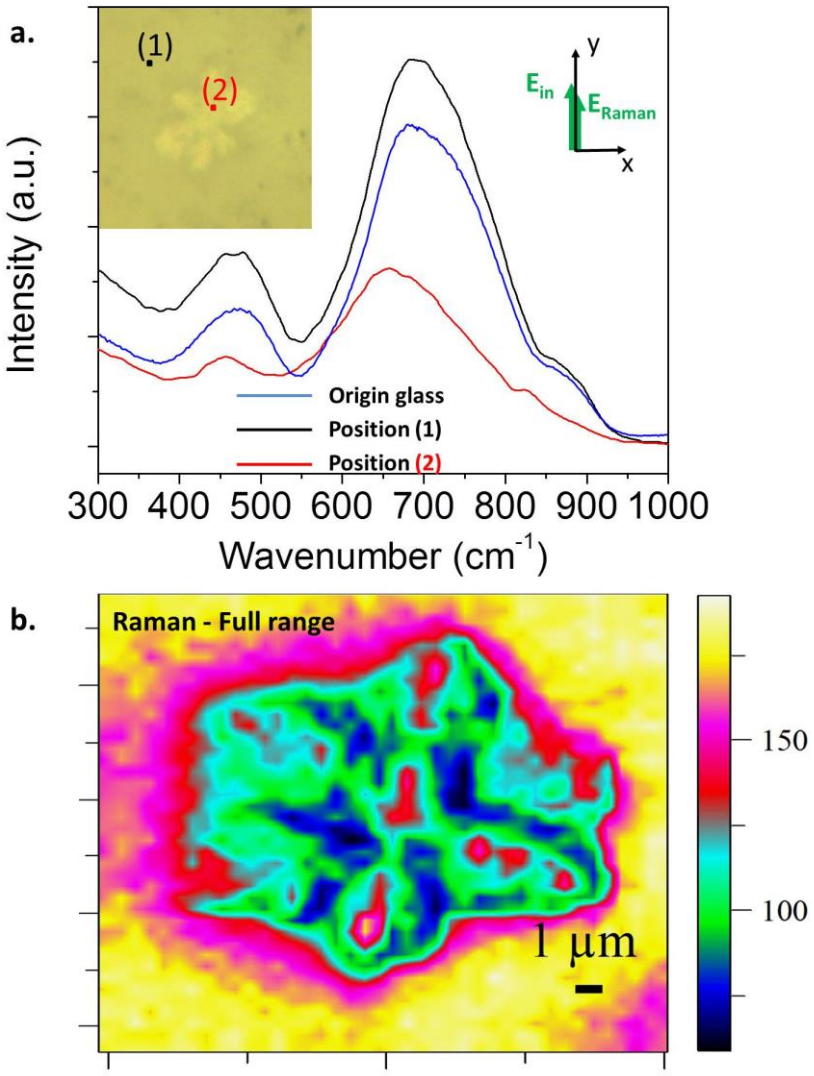

Figure 4.4: (a) Raman spectra of the two positions inside and outside the domain and (b) micro-Raman map of a domain in 1S60 which illustrates the difference in full spectral range from 350 cm^{-1} to 1000 cm^{-1}. The polarizations of the measurement is yy (see Chapter 2, part A)

A supplementary micro-Raman spectrum has been registered for the most crystallized 2S8h sample for comparison with spectra collected in Figure 4.4. The three spectra are normalized at their maximum and shown on **Figure 4.5a**. One can see from this figure the Raman spectra of the glass in region (1) is the same as observed for the as-quenched glass (Figure 3.3). This is in accordance with a very slight modification of the composition observed by WDS in Chapter 4.2.2. A shift to a lower wavenumber of the main 550-800 cm^{-1} band is observed inside the

studied domain (2). The small band around 850 cm^{-1} attributed to Nb-O bond vibrations remains small though an increase in Nb at% is observed in WDS analysis (see Table 4.1). But the peak appears interestingly sharper compared to the glass matrix. This could be an indication of the presence of $K[Nb_{1/3}Te_{2/3}]_2O_{4.8}$ or $(Ag,K)[Nb_{1/3}Te_{2/3}]_2O_{4.8}$ crystalline phase though the ratio of crystallization was estimated to be very small (see Chapter 3.4). The increase of the crystallization rate for 2S8h induces a more important shift of the main band and more sharpness of the small band attributed to Nb-O bonds. The subtraction of the Raman spectrum inside the studied domain (spot (2) in Figure 4.4) in 1S60 with the reference to the glass matrix spectrum (spot (1) in Figure 4.4) was carried out (Figure 4.5b). As a sequence, the observed differences of signal will be discussed for 3 main bands (band 1 to 3). The first two bands (520-680 cm^{-1} and 680-825 cm^{-1}) related to the Te-O bonds (TeO_4 trigonal bypyramid (tbp) asymmetric vibrations and TeO_3/TeO_{3+1} trigonal pyramid (tp) vibrations, correspondingly) while the last small one belongs to Nb-O (850 – 900 cm^{-1}). We observe the increase of TeO_4 tbp band (1) whereas TeO_3/TeO_{3+1} tp and Nb-O Raman active bands (2) and (3) decrease in global intensity, though sharpness of the Nb-O vibration peak inside the domain appears with positive difference at 825 cm^{-1} on the lower energy side of the Nb-O vibration band. In conclusion, a reorganization of distorted TeO_3/TeO_{3+1} tp to form TeO_4 tbp linked together with Te-O-Te bridges is observed [12]. This agrees fairly well with the observation and conclusion proposed by Hart et al. [13] in the potassium niobate tellurite glass ceramics with compositions similar to the phase separated domain. Sharpness of the 350-520 cm^{-1} vibration band observed in the domain is probably explained by the disappearance of Ge-O-X bands vibrations consecutive the vanishing of Ge from the composition. This band is then purely attributed to Te-O-Te bridges. One can notice the positions of maxima for the bands attributed to TeO_4 and Te-O-Te correspond to the maxima positions observed for the crystal phase δ–TeO_2 [12].

The shape of the band attributed to Nb-O bands shows two maxima around 825-840 cm^{-1} and 900 cm^{-1} which correspond to the 1S60 sample and the highly

crystallized sample. This is characteristic spectrum for Nb highly distorted octahedral oxygenated sites in oxide glass with at least one non-bridging oxygen forming shorter Nb-O bond [14].

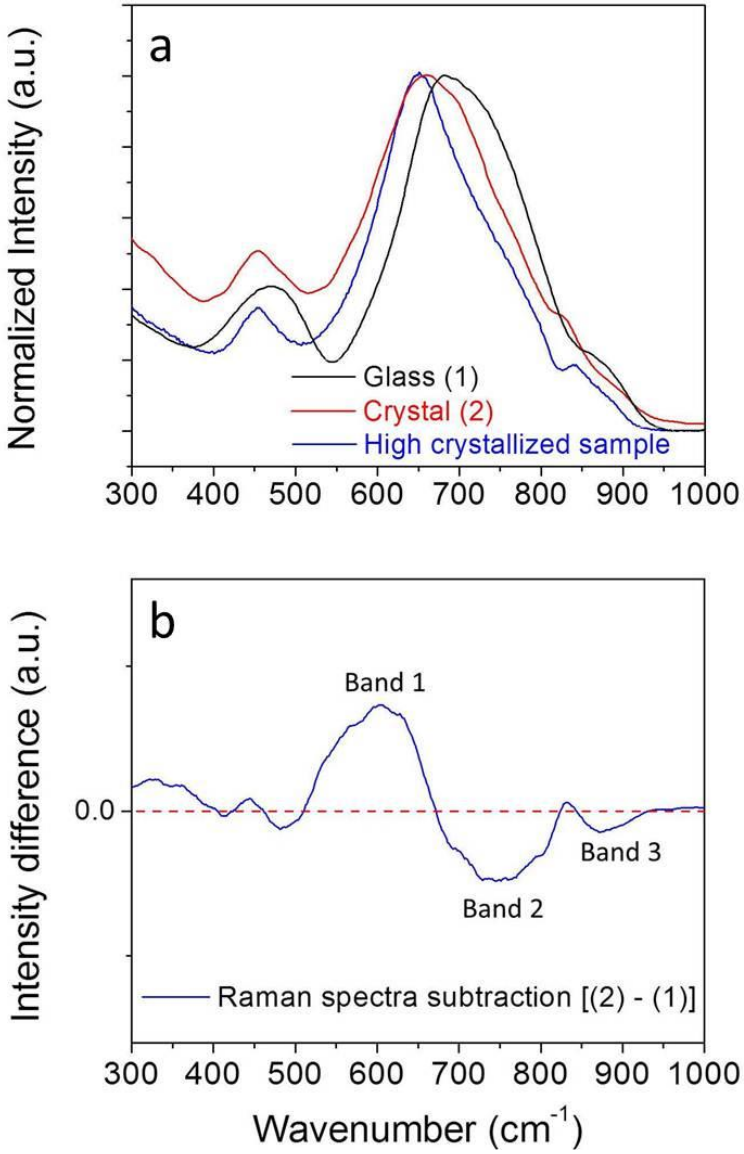

Figure 4.5: (a) Normalized Raman spectra of 2 spots inside and outside the separated region (1) and (2) in 1S60 and a spot in the high crystallized 2S8h sample. Regarding the spot (1) as reference, the subtraction of two spectra gives the rise of three main bands (Band 1-3).

4.3.2 Micro-Raman/micro-SHG responses of crystallized domains

Micro-SHG mapping of the same star-like domain in 1S60 clearly confirms the origin of the optical nonlinear signal inside the phase separated domain (**Figure 4.6a**). The signal is clearly emitted by collection of $K[Nb_{1/3}Te_{2/3}]_2O_{4.8}$ or $(Ag,K)[Nb_{1/3}Te_{2/3}]_2O_{4.8}$ crystallites localized in this area. The SHG mappings for identical (y;y,y) and crossed (y;x,x) polarizations (Figure 4.6a and b, respectively) show overall intensity dramatically different from each other (one order of magnitude). However, both images of the studied 6-pointed star domain shows 4 more-active corners, the other two branches being less-active (Figure 4.6). This SHG activity within the domain fits well with the more modified Raman broad bands (1, 2, 3) integrated intensities as shown on Figure 4.6c-e where the two less-SHG-active corners show less structural modification. Within the corners more-active in SHG, the tellurite and niobate network is more affected. This would be the signature of local structure reorganization highly correlated to the crystallization process. Moreover, if we compare to global Raman linked to density variations (Figure 4.4b), a good comparison can be done. It tends to prove that higher density within the domains corresponds to crystallized zones which are SHG active.

However, some difference remains between micro-SHG and micro-Raman mapping (Figure 4.6). On micro-SHG mapping, one can see well-aligned crystal signal in the 4 active corners emitting comparable intensity. On micro-Raman mapping, the difference is more pronounced in the center of the domain and progressively reduced when going far from the center in the SHG active corners. This would be an indication of a progressive local structure rearrangement of the glass network from the center of the domain (beginning of the phase separation) with departure of Ge, income of Nb and exchange of K to Ag. But one can further take into account the volume of the probed zone by the usage of micro-Raman. At the center, the probed volume would be purely from the star-like domain whereas, at the corners where their size is limited at a few micrometers, either the domain or the glass matrix was probed.

More pronounced Raman and SHG activities in the 4 corners of the domain are confirmed throughout the sample as one can see in 3D mapping (probing the domain along z-axis, **Figure 4.7**).

Coming back to Figure 4.6a and b, the intensities observed in y;y,y polarization are much higher than the one polarized along y;x,x. Therefore, the dipolar nature of the SHG crystallites response is supposed to be at the origin of this large decrease of the signal. In addition, a similar conclusion was deduced from macro-SHG patterns in Chapter 4.2.

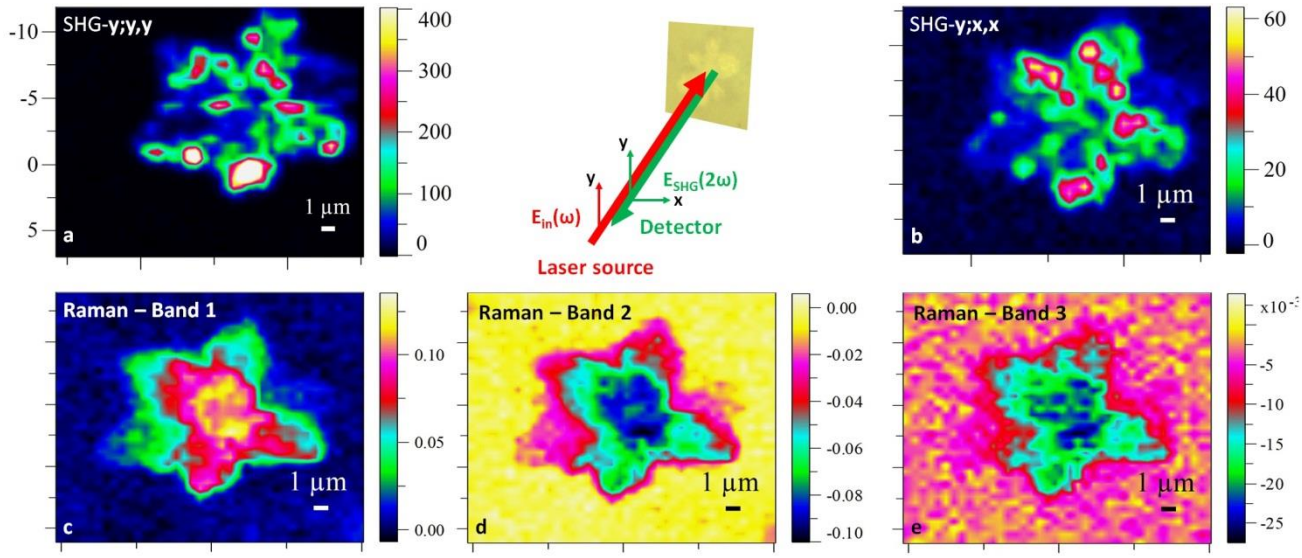

Figure 4.6: The map of SHG in (a) y;y,y and (b) y;x,x modes and their correlative Raman maps of (c) band 1 and (d) band 2 and (e) band 3 as described in Figure 4.4b.

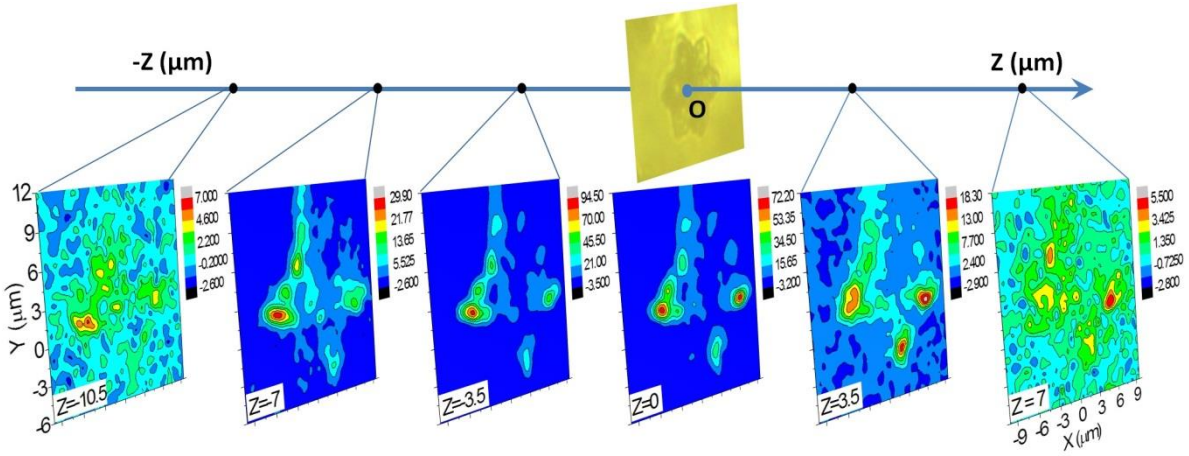

Figure 4.7: SHG maps of 1S60 glass ceramic sample in Z-axis were performed to obtain full picture in 3-dimensions.

However, dipoles non-aligned with the excitation polarization surprisingly show SHG signal in contradiction with the hypothesis of dipoles radially oriented from the center described in other glass ceramics [1]. As observed on **Figure 4.8**. SHG signal remains constant when the angle between the excitation polarization and the crystallized domain varies. It means the dipolar behavior according to polarization studies is invariant to the rotation at the micrometer scale. Therefore, we have to consider a substructure of the crystals leading to the production of this original SHG response.

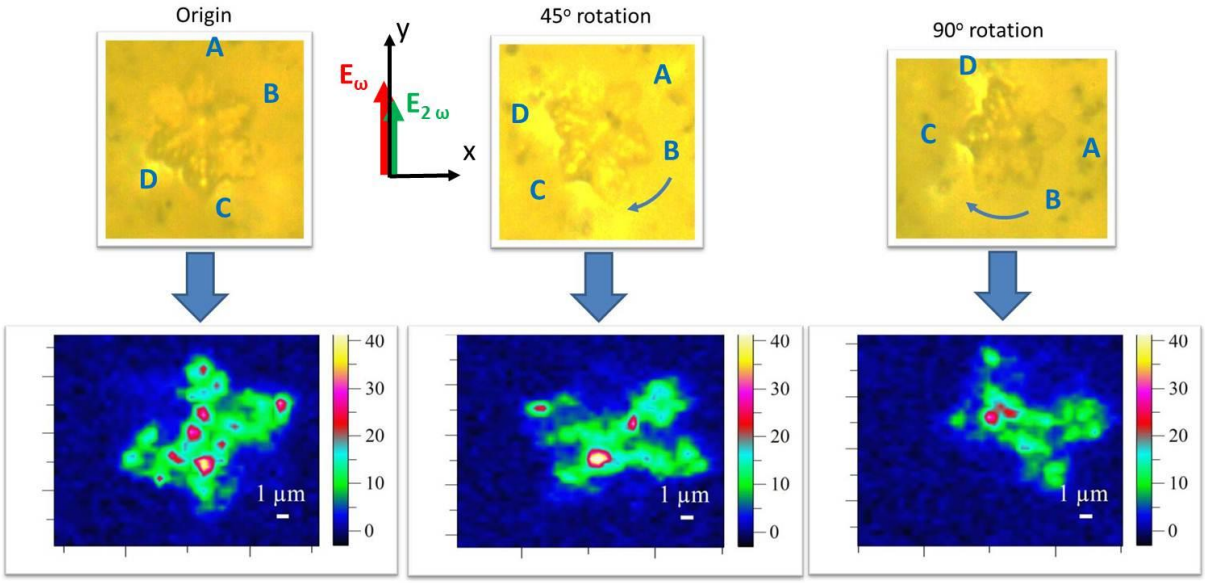

Figure 4.8: SHG intensity mapping of a star-like separated domain of 1S60. The patterns are identical. Different angle of rotation of the sample towards fixed excitation of polarization (0°, 45°, 90°) are presented. A, B, C and D are the four corners which deliver the maximum SHG signal.

B. DISCUSSION

4.4 Model for crystal growing and local structure in the domain

4.4.1 Preferable surface crystallization within phase separated domains

From WDS analysis, one can suppose the creation of phase separated centers in the glass matrix. During the thermal treatment, they would grow progressively in

equivalent directions of the space thereby forming 3D star-like shape domains. From experimental at% measured in Table 4.1, one can estimate the composition of the domain to be ~ 67% TeO_2 – 16.5% Nb_2O_5 – 16.5% $(Ag,K)_2O$ very close to the composition studied by Jeong et al. [7, 8] and Sakai et al. [6]. In $15K_2O$ – $15Nb_2O_5$ – $70TeO_2$ glass composition, Sakai et al. obtained the precipitation of monocrystallites of the unique phase $K[Nb_{1/3}Te_{2/3}]_2O_{4.8}$ after thermal treatment. The Maker Fringes SHG macroscopic measurement of the glass ceramics showed typical pattern of the two ~50 µm crystallized surface layers of the sample [6, 9]. Optically active nanocrystals are precipitated in the surface layers with c axis perpendicular to the surface [9]. This allowed the authors to suppose preferential oriented surface crystallization in this glass composition (the SHG signal was equal to zero for θ=0 angle of incidence proving the bulk response was the noise level) [6, 9].

From these previous studies and consideration of the remaining amorphous glass composition in the studied star-like domain, one can postulate preferential crystallization of $(Ag,K)[Nb_{1/3}Te_{2/3}]_2O_{4.8}$ at the interface between the corners of the separated domain and the glass matrix. c axis of the crystallites would be oriented perpendicularly to the interface. As the corners of the domain progressively extend with the thermal duration, the crystallization would follow the evolution of the interface and take place all along the branches of the star-like domain. Nevertheless, one cannot explain why the same favorable situation does not happen in all the corners of the domain but in only 4 of them (Figure 4.6 and 4.7).

4.4.2 Local structure modifications

Reorganization of the tellurite and niobate networks has been shown in Figure 4.5b which seems to be in contradiction with cations enrichment of the separated domain observed from WDS (Table 4.1). However, one can find a possible explanation in the local modifications induced by the precipitation of crystallites. The crystal phase has an atomic ratio Te/Nb which is exactly the same as the one measured by WDS in the domain, but the ratio Te/(K+Ag) is lower in the crystal. So the precipitation of crystallites locally depletes the environment in K^+/Ag^+

cations, which could induce local relinking of the tellurite network. On other side, Hart et al. [15] claimed a polymorph of $K_2Te_4O_9$ structure known to have tetragonal lattice for the crystalline phase appearing in $15K_2O – 15Nb_2O_5 – 70TeO_2$ glass composition. As discussed in Chapter 1, this hypothesis was rejected by Jeong et al. [7] after they proved the composition of the crystal included Nb cations, but the structure proposition of Hart et al. fitted quite perfectly with X-ray and neutron diffraction results. According to Hart et al., the crystal is described to be essentially long $Te_4O_9^{2-}$ chains separated by K^+ cations. If this structure is close to the structure of $(K,Ag)[Nb_{1/3}Te_{2/3}]_2O_{4.8}$, the tellurite network could be constituted with TeO_4 sites connected by sharing alternatively a corner and an edge like in $K_2Te_4O_9$. Both remarks lead to justify the TeO_4 sites emergence in the crystalline branches of the domain showing SHG in contradiction with the ratio of cations in the domain. Finally, though homogeneous compositions were measured by WDS at the microscopic level all over the domain, sub-microscopic fluctuations of density are observed on Figure 4.4b occurring in the more crystallized branches. If we suppose the crystal denser compared to amorphous environment, then we can suppose the crystallization takes place when favorable density conditions are met. Growing crystalline particles attract K^+/Ag^+ cations from the amorphous environment and then induce relinking of the tellurite glass network. Local increase of the density in the crystalline particles should be compensated by local decrease of the amorphous material density around the particles explaining the sub-microscopic density inhomogeneities observed on Figure 4.4b.

4.4.3 Modelization for crystalline particle substructure

Only few structural hypothesis have been proposed to explain the SHG activity of the $(K,Na)[Nb_{1/3}Te_{2/3}]_2O_{4.8}$ crystal. One hypothesis involves distortion of the lattice due to oxygen vacancy in the fluorite-type structure [7], meaning to keep the stoichiometry (1.6 vacancy/lattice unit). Another hypothesis involves the difference in size between K, Na and Nb, Te which would produce a slight distortion of the cubic structure along an axis [5]. At this point, another consideration concerning the distance Nb-O and Te-O in the crystal can be taken into account to explain this

distortion. In a perfect fluorite-type structure and $a \approx 5.47\text{Å}$, this distance would be around 2.34 Å which is far from the usual shortest distances range usually found in tellurite and niobate oxide crystals: 1.8 – 2.2 Å [12, 14]. Considering the lattice parameter of K_2O fluorite-type structure equal to 6.44 Å, one can suppose a global shift of oxygen positions to Nb and Te positions in the lattice. This is also expected to lead to a distortion of the lattice [15].

In fact, Kim et al. [4] measured a very slight axial distortion c/a = 1.0018, that should be confirmed in our $(Ag,K)[Nb_{1/3}Te_{2/3}]_2O_{4.8}$ crystalline phase through further investigation.

Then according to literature, $(Ag,K)[Nb_{1/3}Te_{2/3}]_2O_{4.8}$ crystalline phase is supposed to be monoaxial and is expected to show dipolar nonlinear optical behavior [3]. Following this assumption, the maximum SHG activity is expected when crystallites have **c**-axis oriented along the polarization of excitation. Obviously the model of the crystallization process proposed in Chapter 4.4.2 has to fit to the original SHG response presented on Figure 4.6a and b: design of crystal precipitation must show dipolar behavior unchanged with rotation around the laser polarization. A proposal of Ban et al. [16-18] provides a suggestion for the substructure of 6-pointed star-like TiO_2 anatase in which the crystalline faces [100] grow in two directions making an angle of 45^o between them. However, this hypothesis cannot be confirmed because germanotellurite based glass is destroyed under high energy electron beam. Therefore, it is impossible to investigate the crystal structure in atomic scale (by high resolution transmission electron microscope for instance). However, the SEM images indicate obviously that, in each corner, there are extra branches which make a 45^o angle from the c-axis (**Figure 4.9a**).

According to the proposition of Ban et al., c axis of the nanocrystallites would be oriented as indicated on Figure 4.9a. This hypothesis agrees fairly well with the previous interface crystallization process proposed in 4.4.1.

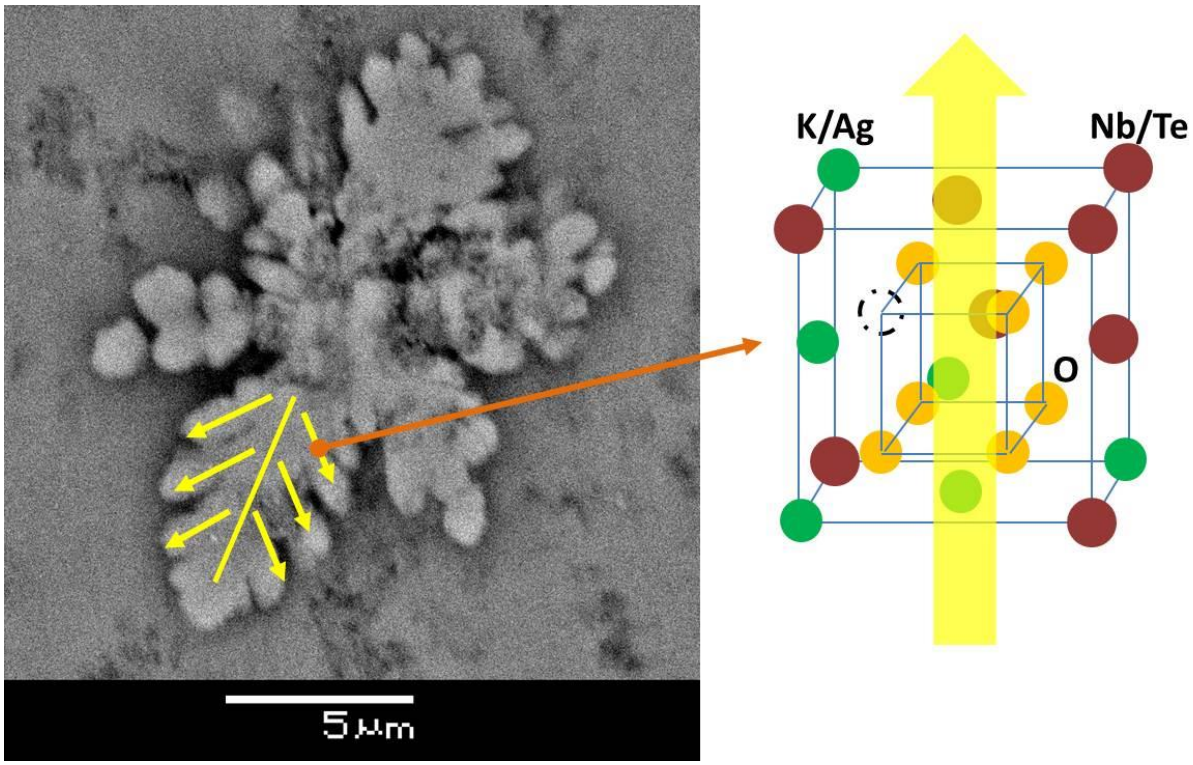

Figure 4.9: (a) 6-corner domain inside the 1S60 sample imaged by scattering electron microscopy and predicted dipoles of (Ag,K)[$Nb_{1/3}Te_{2/3}$]$_2O_{4.8}$ crystallites within the phase separated domain (yellow arrows); (b) Crystalline structure proposed by Jeong et al. [7].

The proposed sub-structure can be utilized to interpret the SHG behavior of the star-like domain (Figure 4.9a). The general output SHG signal is the summation of SHG from each oriented crystallite. The size of the corner in comparison to the coherence length (estimated around 6 µm, Chapter 3) and second harmonic wavelength (0.532 µm) should be taken into account. In this case, the size of corner range from 5-6 µm is quite close to the estimated coherence length of the materials and far from the second harmonic wavelength. So two separated opposite parts of the corner can be supposed to produce nondestructive summation [1, 2].

Furthermore, although there is no information about the nonlinear optical activity of the crystal (Ag,K)[$Nb_{1/3}Te_{2/3}$]$_2O_{4.8}$, the clear dipolar macroscopic SHG behavior of the sample has been recognized in both the macro- and micro-SHG responses as described in Chapter 4.2 and 4.3.2. This allows to suspect a strong one-dimension

scalar d_{33} susceptibility when compared to other nonlinear components of the tensor as mentioned by Vigouroux et al. [1]. **Figure 4.10** presents the SHG responses due to the dipolar term d_{33} of the corner containing crystallites according to the model of substructure presented on Figure 4.9a. On this Figure, one can observe that whatever orientation of the corner versus excitation, SHG signal due to d_{33} remains unchanged with polarization along the direction of the excitation. This model agrees with the observations made on Figure 4.8.

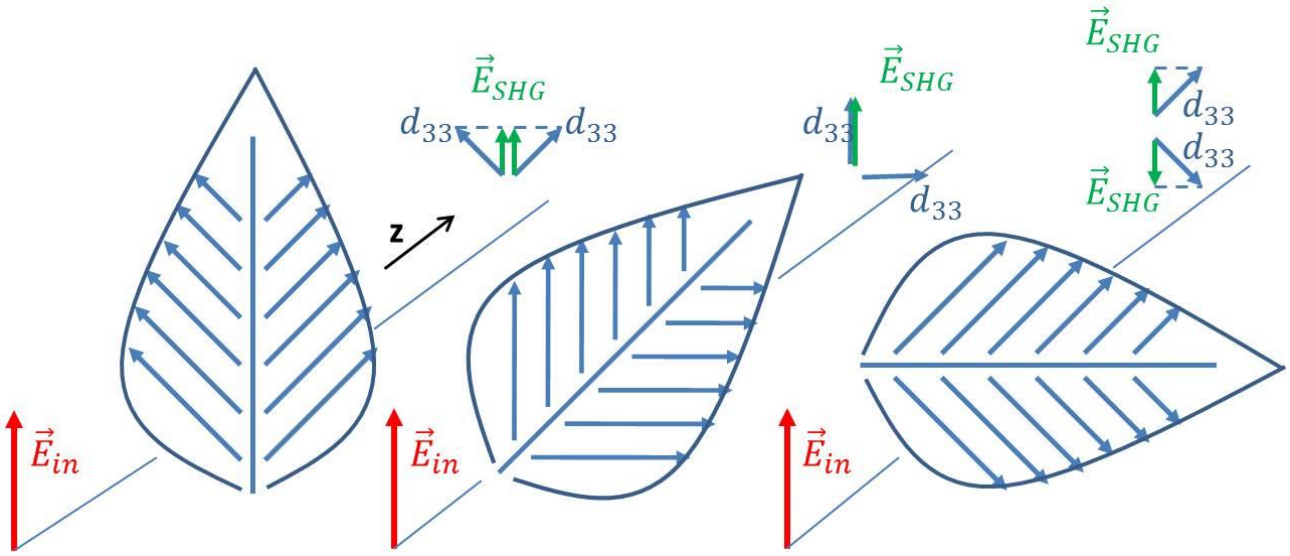

Figure 4.10: Illustration of a corner when it is rotated around E_{in} direction. The response with tensor d_{33} is presented for simplification. This hypothesis allows explaining SHG behavior shown in Figure 4.7.

For polarization of SHG signal perpendicular to excitation, other tensor components of the crystal are involved.

4.5 Conclusion

In this chapter, we confirm that the star-like phase separated domains in germanotellurite glass ceramics are mainly amorphous potassium-niobate tellurite glass with low ratio of nanocrystallites $(Ag,K)[Nb_{1/3}Te_{2/3}]_2O_{4.8}$ where silver partly replaces potassium to form the crystals. The phenomenon was observed in other glass ceramic system where sodium and potassium exist together in the crystal

phase ($(Na,K)[Nb_{1/3}Te_{2/3}]_2O_{4.8}$). Further investigation has to be performed to confirm this hypothesis.

The star-like domains contain all precursors for the crystallization though SHG mapping images show uneven inactivity of the different corners. The active corners with active-SHG response show reorganization of the amorphous glass network coinciding to local precipitation of nanocrystallites.

Besides the demonstration of rotation independence microscopic SHG responses of the glass ceramics perpendicularly to the direction of propagation of the excitation, the dipolar behavior of the signal has been proved at macroscopic and microscopic scale (Ψ_p and Ψ_s modes for macro-SHG and y:x,x and y:y,y modes for micro-SHG). However, the organization of nanocrystallites inside the star-like domain differs from $LiNbO_3$ nanocrystallites radially oriented inside the spherulites observed in LNS glass ceramics and developed in Chapter 2. The substructure is assumed to simile the microstructure of TiO_2 anatase growth where the face [100] growth in two ways which makes an angle of 45º with the main direction. The SEM image of a domain has supported this assumption.

The correlation between micro-SHG and macro-SHG has been simulated by applying the as-developed mathematic model in Chapter 3 and assuming the previously described substructure for $(Ag,K)[Nb_{1/3}Te_{2/3}]_2O_{4.8}$ nanocrystallites, the crystal phase belonging to the symmetry point group C_4 or C_{4v}.

REFERENCES

1. Vigouroux, H., E. Fargin, S. Gomez, B. Le Garrec, G. Mountrichas, E. Kamitsos, F. Adamietz, M. Dussauze, and V. Rodriguez, *Synthesis and Multiscale Evaluation of LiNbO3-Containing Silicate Glass-Ceramics with Efficient Isotropic SHG Response.* Advanced Functional Materials, 2012. **22**(19): p. 3985-3993.
2. Truong, L.N., M. Dussauze, E. Fargin, L. Santos, H. Vigouroux, A. Fargues, F. Adamietz, and V. Rodriguez, *Isotropic octupolar second harmonic generation response in LaBGeO5 glass-ceramic with spherulitic precipitation.* Applied Physics Letters, 2015. **106**(16): p. 161901.
3. Shioya, K., T. Komatsu, H.G. Kim, R. Sato, and K. Matusita, *Optical properties of transparent glass-ceramics in K2O・Nb2O5・TeO2 glasses.* Journal of non-crystalline solids, 1995. **189**(1): p. 16-24.
4. Kim, H.G., T. Komatsu, K. Shioya, K. Matusita, K. Tanaka, and K. Hirao, *Transparent tellurite-based glass-ceramics with second harmonic generation.* Journal of non-crystalline solids, 1996. **208**(3): p. 303-307.
5. Kim, H. and T. Komatsu, *Fabrication and properties of transparent glass-ceramics in Na2O-Nb2O5-TeO2 system.* Journal of materials science letters, 1998. **17**(13): p. 1149.
6. Sakai, R., Y. Benino, and T. Komatsu, *Enhanced second harmonic generation at surface in transparent nanocrystalline TeO2-based glass ceramics.* Applied Physics Letters, 2000. **77**(14): p. 2118-2120.
7. Jeong, E., J. Bae, M. Ha, H. Kim, H. Pak, B. Ryu, and T. Komatsu, *Structure of a nanocrystalline phase with second harmonic generation.* Journal-Korean Physical Society, 2007. **51**: p. S32.
8. Jeong, E., J. Bae, T. Hong, K. Lee, B. Ryu, T. Komatsu, and H. Kim, *Thermal properties and crystallization kinetics of tellurium oxide based glasses.* Journal of Ceramic Processing Research, 2007. **8**(6): p. 417.
9. Komatsu, T. and T. Honma, *Optical Active Nano-Glass-Ceramics.* International Journal of Applied Glass Science, 2013. **4**(2): p. 125-135.
10. Jeong, E.D., P.H. Borse, J.S. Lee, M.G. Ha, H.K. Pak, T. Komatsu, and H.G. Kim, *Second harmonic generation and fabrication of transparent K2O-Na2O-Nb2O5-TeO2 glass-ceramics.* Journal of Industrial and Engineering Chemistry, 2006. **12**(5): p. 790-4.
11. Vigouroux, H., E. Fargin, A. Fargues, B.L. Garrec, M. Dussauze, V. Rodriguez, F. Adamietz, G. Mountrichas, E. Kamitsos, and S. Lotarev, *Crystallization and second harmonic generation of lithium niobium silicate glass ceramics.* Journal of the American Ceramic Society, 2011. **94**(7): p. 2080-2086.
12. Dutreilh-Colas, M., *Nouveaux matériaux pour l'optique non linéaire: Synthèse et étude structurale de quelques phases cristallisées et vitreuses appartenant aux systèmes TeO (2)-Tl (2) O-Ga (2) O (3) et TeO (2)-Tl (2) O-PbO*. 2001, Limoges.
13. Hart, R.T., M.A. Anspach, B.J. Kraft, J.M. Zaleski, J.W. Zwanziger, P.J. DeSanto, B. Stein, J. Jacob, and P. Thiyagarajan, *Optical implications of crystallite symmetry and structure in potassium niobate tellurite glass ceramics.* Chemistry of materials, 2002. **14**(10): p. 4422-4429.
14. Cardinal, T., *Propriétés optiques non linéaires des verres borophosphatés de titane ou de niobium*. 1997.
15. Hart, R.T., J.W. Zwanziger, and P.L. Lee, *The crystalline phase of (K 2 O) 15 (Nb 2 O 5) 15 (TeO 2) 70 glass ceramic is a polymorph of K 2 Te 4 O 9.* Journal of non-crystalline solids, 2004. **337**(1): p. 48-53.

16. Ban, T., T. Nakatani, Y. Uehara, and Y. Ohya, *Microstructure of six-pointed starlike anatase aggregates.* Crystal Growth and Design, 2008. **8**(3): p. 935-940.
17. Ban, T., T. Nakatani, and Y. Ohya, *Morphology of anatase crystals and their aggregates synthesized hydrothermally from aqueous mixtures of titanium alkoxide and different alkylammonium hydroxides.* Journal of the Ceramic Society of Japan, 2009. **117**(1363): p. 268-272.
18. Ban, T., N. Nakashima, T. Nakatani, and Y. Ohya, *Hydrothermal synthesis of oriented anatase films consisting of columnar aggregates and their wetting properties.* Journal of the American Ceramic Society, 2009. **92**(6): p. 1230-1235.

GENERAL CONCLUSIONS

Different approaches have been combined to elaborate glass and glass ceramics based on germanotellurite composition doped with silver oxides and to characterize local structure and SHG. The addition of silver cations was shown to promote the bulk crystallization of a unique crystalline phase which was already known to produce SHG. The best composition was chosen for further glass ceramics elaboration and characterization. Therefore, with the help of correlative micro-SHG/micro-Raman combined to WDS quantitative element analysis allowed to characterize the crystal growing process and organization inside star-like phase-separated domains.

At the beginning of this thesis, a literature review to recall the background of our research from basic glass and glass ceramic knowledge to physical principle of nonlinear optics in respect to the symmetry of crystals has been done. We also provided a collection of SHG-active crystals as well as recent studies of several kinds of tellurite-based glass ceramics. In order to understand the nature of the SHG-active crystallites precipitated within the tellurite glass matrix, the studies of $K[Nb_{1/3}Te_{2/3}]_2O_{4.8}$ were reviewed. Its crystal structure and the origin of SHG are still in debate. A more popular hypothesis of distorted fluorite-type structure was proposed since 1990s, mainly because of the typical XRD patterns of cubic structure. However, Hart et al. then rejected the hypothesis because it cannot be used to explain the unusual Te-O distance and neutron diffraction patterns. The authors themselves suggested a new model based on $K_2Te_4O_9$ in which the oxygen anions would be distributed randomly around order cations. However, the new model did not interpret clearly the presence of Nb elements which was justified later by Jeong et al. At the end of the chapter, several studies consist on atomic exchange of K and Na in $(K,Na)[Nb_{1/3}Te_{2/3}]_2O_{4.8}$ composition have been shown. Furthermore, the distortion of the crystal cubic structure was proposed to partly depend on the ionic size difference between K and Na because $Na[Nb_{1/3}Te_{2/3}]_2O_{4.8}$ does not induce any SHG signal.

Before investigating the germanotellurite glasses and glass ceramics, we developed a mathematical model for the correlation between local structure of a spherulite and the

macroscopic SHG patterns. The model has been proposed to have the general formula as follow:

$$I_{\Psi i}^{2\omega} \propto \left|P_i^{2\omega}(\Psi)\right|^2 = (E_o^{\omega})^4/8\,|Acos^4(\Psi) + Bsin^4(\Psi) + C\sin^2(\Psi)\cos^2(\Psi)| + D$$

According to the comparison among A, B, and C terms which relate to the $\chi^{(2)}$ coefficients and the value of scattering loss D, the typical dipolar or octupolar shape of macroscopic SHG patterns can be simulated. The correlative macroscopic SHG measurement setup and operation to obtain different $\chi^{(2)}$ tensors would be helpful to derive all the terms. The model was then attempted to apply for two different glass ceramic systems that were previously studied by Vigouroux et al., $LiNbO_3/SiO_2$ (LNS) and $LaBGeO_5$ (LBG) glass ceramics.

Based on the correlative micro-Raman/micro-SHG characterization described in the first part of Chapter 2, both the LNS and LBG glass ceramic systems were proven to contain radially oriented crystallized spherulites. In both cases, the c-axis of spherulites corresponds with the SHG-active dominant orientation (d_{33}) of $LiNbO_3$ crystal and $LaBGeO_5$ crystal. In LNS glass ceramics, the mathematical model describing the macro SHG patterns depends on the polarization of the detector (x or y in lab preferential frame). However, they are identical but rotated 90°. The dipolar dominant d_{33} is at the origin of dipolar macroscopic SHG signal. In the specific case of the LBG glass ceramics, an antiparallel orientation of crystallites domains along c-axis is expected to explain the loss of the dipolar d_{33} component in the SHG response. The macroscopic SHG equation is independent with the polarization of incoming laser beam and detector.

The model shows good agreement with experimental results in both LNS and LBG glass ceramics, so this resulted model would be useful for the next glass ceramic system based on germanotellurite composition in respect to its local crystal organization and symmetry.

Back to the tellurite-based glasses, we demonstrated the possibility to elaborate germanotellurite glass with different amounts of silver oxide content from 0 to 6 %mol. Then, the effect of the doping into glass properties was introduced. The promotion of

bulk crystallization by adding silver oxide as a nucleation agent has been demonstrated. We obtained a uniquely phase crystallization, i.e. $K[Nb_{1/3}Te_{2/3}]_2O_{4.8}$, induced by heat treatment in those samples. The crystals were then demonstrated to be SHG active. Besides that, the microstructure of germanotellurite glasses is influenced by the conversion from TeO_4 tbp to TeO_3/TeO_{3+1} tp as the content of Ag_2O increases. Silver ions can break the TeO_4 network and release the NBOs. This effect also leads to the slight red shift of their transmission spectra at the UV edge through the formation of localized states within the band gap. The behavior of silver within the germanotellurite glass was also discussed. For high silver oxide content (4 or 6 % mol), the presence of silver clusters due to annealing was observed through photoluminescence detection. However, the existence of clusters within the lower silver oxide contained glasses cannot be ruled out due to the high cut-off wavelength value of the materials.

In order to favor the crystalline phase for glass ceramic study, 6 %mol of Ag_2O was added to the nominal glass composition which was then heat-treated to foster the nucleation and crystallization. The optical properties were affected by the duration of heat treatment as well as the method of elaboration (1-step or 2-step). The results show that, although a 2-step heat treatment can improve the nucleation, it also enhances phase separation and quickly decreases the transparency of glass ceramics. On the other hand, the 1-step heat treatment promotes the star-like domains, in which $K[Nb_{1/3}Te_{2/3}]_2O_{4.8}$ crystallites appear. However, the SHG signals generated from 1-step heat treated samples are far higher than 2-step samples', even with similar transparency and crystallite quantity. It leads to the suggestion that the SHG intensity is strongly related to the organization of crystallites within the star-like domains.

To study further about the germanotellurite glass ceramics in respect of crystalline phase and substructure within the phase separated star-like domain, we used multi-scale approaches based on correlative micro-Raman/micro-SHG characterizations. At first, we found that the crystal phase should be modified to $(Ag,K)[Nb_{1/3}Te_{2/3}]_2O_{4.8}$ where silver atoms will replace partly potassium to form the crystals. The star-like domain contains all precursors for the crystallization as observed in WDS elemental quantification map. However, the low quantity of potassium in comparison with the

nominal crystal phase and the existence of silver element support the idea of modified crystal phase with Ag constituent. In literature, the phenomenon was observed in other glass ceramic system where sodium and potassium exist together in the crystal phase ($(Na,K)[Nb_{1/3}Te_{2/3}]_2O_{4.8}$). The crystal structure should be cubic but oxygen atoms will be oriented randomly around cations.

The correlation between micro-SHG and the global responses has been also simulated by applying the as-developed mathematic model in Chapter 2. Furthermore, based on the assumption of slight distortion cubic structure of $(Ag,K)[Nb_{1/3}Te_{2/3}]_2O_{4.8}$, we can find out that the nonvanishing components in the symmetry point group of the crystal phase can match with C_4 or C_{4v}. It is noted that the slight distortion can be affected by the atomic size of silver and potassium, so the values of d_{33} and d_{31} could be different towards the ratio of Ag/K in the crystal phase.

The micro-SHG mapping images confirm that the star-like objects in germanotellurite glass ceramics are mainly phase separated domains with partly distributed crystallites as assumption in Chapter 3. This is because of some relatively SHG-inactive corners. When we compare the obtained SHG maps of a star-like domain with its correlative micro-Raman map, the correlation between them can be found. The corners with active-SHG response show the increase of TeO_4 bonds and decrease of TeO_3 and NbO_6 than others. It means that some specific spots within the domain reorganize during the heat treatment and transform to crystallites.

In addition to the demonstration of in-plane isotropic property of the glass ceramics, the dipolar property of the sample in macroscopic and microscopic scale is evidenced by using different measurement modes (pp/sp in macro-SHG and yy/yx in micro-SHG). Nevertheless, the substructure of the star-like domain differs from $LiNbO_3$ spherulites in LNS glass ceramics which was proven to have radial distribution. The SHG-active spots in star-like domain stay quite stable when rotating the sample. The substructure is assumed to simile the microstructure of TiO_2 anatase growth where the face [100] growth in two ways which makes an angle of 45^o with the main direction.

These results show a potential of tellurite-based glass ceramics as a candidate for optical nonlinear applications in spite of the needs of further studies to obtain higher transparent glass ceramics with strong SHG activity. Thereby, the study provides several perspectives for further researches and applications.

- More investigations are needed for several hypotheses and issues in this study such as the nature of phase separated droplets, the structure of crystal phase and the inactivity of some SHG-active branches within star-like domains. Furthermore, one can also optimize the heat treatment to obtain higher transparency as well as optical nonlinear behavior of the glass ceramics.

- Because the works of this study focused only on glass ceramics with 6%mol Ag2O content, it could be interesting to investigate other doping amounts with appropriate heat treatment. It is worth to notice that the addition of silver oxides significantly modifies the properties of germanotellurite glass as observed in XRD patterns of heat treated 7T1GxAg samples.

- Applications of thermal poling to generate SHG signal in germanotellurite glass and the effect of silver cations on the optical nonlinearity would be another research direction.

- Other perspectives which can be listed out are the possibility of doping other nucleating agents like Au, Pt or ZrO_2 and TiO_2.

FIGURES

Titre : Deuxième génération d'harmoniques dans la céramique de verre Germanotellurite dopés avec l'oxyde d'argent.

Résumé :

L'importance du traitement du signal et la transmission favorise de nouvelles applications pour les matériaux optiques non linéaires, tels que des convertisseurs de fréquence. Les cristaux sont des matériaux pour ces applications bien connues en raison de leur comportement non linéaire optique forte. Cependant, ils sont coûteux à fabriquer et dépendent fortement de l'orientation cristalline. Les verres sont des candidats possibles à cause de leurs propriétés optiques et la facilité de fabrication, mais ils ne possèdent pas de second ordre non-linéarité en raison de leur structure centrosymétrique. Cependant, un matériau composite vitrocéramique avec des cristaux ferro-électriques noyées dans une matrice de verre peut combiner les propriétés de cristaux non linéaires avec la facilité de fabrication de lunettes.

Germanotellurite verre et la céramique, verre dopés avec différentes quantités d'oxyde d'argent, dans la (100-x) (70TeO2 - 10GeO2 - 10Nb2O5 - 10 - K2O) xAg2O système (x = 0 à 6% en mole), a été étudiée. L'étude se compose de l'élaboration et la caractérisation d'une céramique de verre qui peuvent répondre aux exigences de matériaux optiques non linéaires, avec une grande transparence et une activité non linéaire intense. Les caractéristiques des verres et de la céramique de verre ont été déterminées par analyse thermique, diffraction des rayons X, la microscopie électronique, UV-Vis et spectroscopie Raman. Cristallisation en vrac a été observé pour les verres d'argent dopé avec une phase cristalline unique (Ag, K) [Nb1 / 3Te2 / 3] 2O4.8, qui présente une activité seconde génération harmonique (SHG). Un seul traitement thermique a abouti transparence supérieure à un traitement thermique en 2 étapes avec un premier chauffage à la température de nucléation et un second traitement pour la croissance cristalline. Pour les modes de transmission et XRD UV-Vis similaires, les échantillons de chaleur 1-étape traités ont montré une réponse SHG deux ordres supérieur à la 2-étape.

Cette différence d'intensité provient de la taille des domaines à l'intérieur des deux céramiques de verre. Le traitement thermique une étape a été trouvé, de promouvoir micron de taille domaines cristallisés, alors que le traitement thermique en deux étapes a abouti à des tailles de sous-domaine de longueurs d'onde. La réponse macroscopique SHG global a été trouvé pour présenter le comportement dipolaire typique. Ce dipôle nature vient de chaque domaine agissant comme SHG émetteur. Une caractérisation basée sur une technique de micro-Raman / micro-SHG corrélative, qui peut fournir à la fois des informations structurelles et les réponses de SHG locales dans les mêmes régions sub-micron, a été réalisée, ce qui indique que l'organisation de cristallites dans les domaines rend leur réponse SHG indépendante de polarisation de la lumière. Un modèle structural a été proposé pour expliquer la propriété dipolaire général et l'indépendance de la polarisation de la lumière.

Mots clés : céramique vitreuse ; génération harmonique 2 ; germanotellurite.

Title : Second Harmonic Generation in Germanotellurite glass ceramics doped with silver oxide.

Abstract :

The importance of signal processing and transmission promotes new applications for nonlinear optical materials, such as frequency converters. Crystals are well known materials for these applications because of their strong optical nonlinear behaviour. However, they are costly to manufacture and are strongly dependant on crystal orientation. Glasses are possible candidates because of their optical properties and ease of fabrication but they possess no second-order nonlinearity due to their centrosymmetric structure. However, a glass-ceramic composite with ferroelectric crystals embedded in a glass matrix can combine the nonlinear properties of crystals with the easiness of fabrication of glasses.

Germanotellurite glass and glass ceramics, doped with different amounts of silver oxide, in the (100-x)(70TeO2 – 10GeO2 – 10Nb2O5 – 10 K2O) – xAg2O (x=0-6 mol%) system, has been studied. The study consists of elaboration and characterization of a glass ceramic that can fulfil the requirements of nonlinear optical materials, with high transparency and intense nonlinear activity. The characteristics of the glasses and glass ceramics were determined by thermal analysis, X-ray diffraction, electron microscopy, UV-Vis and Raman spectroscopies. Bulk crystallization has been observed for the silver-doped glasses with a unique crystal phase, $(Ag,K)[Nb_{1/3}Te_{2/3}]_2O_{4.8}$, which presents second harmonic generation (SHG) activity. A single heat treatment yielded higher transparency than a 2-step heat treatment with a first heating at the nucleation temperature and a second treatment for crystal growth. For similar UV-Vis transmission and XRD patterns, the 1-step heat treated samples showed a two order higher SHG response than the 2-step one.

This intensity difference comes from the size of domains within the two glass ceramics. The 1-step heat treatment was found to promote micron sized crystallized domains, while the two step heat treatment yielded sub-wavelength domain sizes. The global SHG macroscopic response was found to present typical dipolar behaviour. This dipole nature comes from each domain acting as SHG emitter. A characterization based on a correlative micro-Raman/micro-SHG technique, which can provide both structural information and local SHG responses within the same sub-micron areas, was performed, indicating that the organization of crystallites inside the domains makes their SHG response independent of light polarization. A structural model has been proposed to explain the general dipolar property and the light polarization independence.

Keywords : glass ceramics; second harmonic generation; germanotellurite

---

Unité de recherche

1. Institut de Chimie de la Matière Condensée de Bordeaux (ICMCB), France
2. Institut des Sciences Moléculaires (ISM), Universite de Bordeaux, France
3. Department of Chemical Engineering, Instituto Superior Técnico, Lisbon, Portugal